



## Durham E-Theses

---

### *Measurement of ground-lining pressure distribution around two tunnels in stiff stony clay*

El-Naga, N. M. A.

#### How to cite:

---

El-Naga, N. M. A. (1976) *Measurement of ground-lining pressure distribution around two tunnels in stiff stony clay*, Durham theses, Durham University. Available at Durham E-Theses Online:  
<http://etheses.dur.ac.uk/9092/>

#### Use policy

---

The full-text may be used and/or reproduced, and given to third parties in any format or medium, without prior permission or charge, for personal research or study, educational, or not-for-profit purposes provided that:

- a full bibliographic reference is made to the original source
- a [link](#) is made to the metadata record in Durham E-Theses
- the full-text is not changed in any way

The full-text must not be sold in any format or medium without the formal permission of the copyright holders.

Please consult the [full Durham E-Theses policy](#) for further details.

---

Academic Support Office, Durham University, University Office, Old Elvet, Durham DH1 3HP  
e-mail: [e-theses.admin@dur.ac.uk](mailto:e-theses.admin@dur.ac.uk) Tel: +44 0191 334 6107  
<http://etheses.dur.ac.uk>

MEASUREMENT OF GROUND-LINING PRESSURE  
DISTRIBUTION AROUND TWO TUNNELS IN  
STIFF STONY CLAY

by

N.M.A. El-Naga, B.Sc., Civ.Eng.

Being a dissertation presented to the University of Durham for the  
fulfilment of the requirements of the degree of M.Sc. in Engineering  
Geology by research.

The copyright of this thesis rests with the author.  
No quotation from it should be published without  
his prior written consent and information derived  
from it should be acknowledged.



April, 1976.

## ABSTRACT

This thesis describes the design, construction and calibration of a hybrid hydraulic/electrical type of earth pressure cell and the subsequent use of these cells for the measurement of radial ground pressures bearing on concrete segmental tunnel linings at two locations in mixed clayey ground in north-east England. Also described is an accompanying programme of lining distortion measurement and a preliminary discussion is directed towards theoretical aspects of ground/lining interaction mechanics. The tunnels studied were 3.20 m diameter and at depths of 11.77 m and 12.39 m to the crown. Lining/soil radial interaction pressures were found to be almost uniformly distributed about the tunnel, these recorded pressures being almost one-half the maximum possible overburden pressure calculated on a  $\gamma z$  basis. Furthermore, these ultimate pressures were achieved after a period of only 7 to 8 days following lining erection and grouting. Ultimate measured lining ring distortions were also realized after this 7 day period. This relatively rapid stabilisation of ground pressure contrasts with a much more protracted, on-going distortion reported by other workers in other materials, but is consistent with contractual experience which suggests that tunnel secondary linings could be safely erected, with little risk of brittle fracture, much earlier following primary lining construction than has hitherto been considered prudent.

## CONTENTS

	Page
List of Figures	i
List of Tables	vi
List of Symbols	vii
Acknowledgements	viii
CHAPTER 1: <u>INTRODUCTION</u>	1
1.1 General Introduction	1
1.2 General types of earth pressure cells	8
CHAPTER 2: <u>DESIGN, CONSTRUCTION AND CALIBRATION OF THE PRESSURE CELL USED IN THE PRESENT STUDY.</u>	15
2.1 Design of the pressure cell used in the present study	15
2.2 Construction of the pressure cells	24
2.3 Laboratory calibration	25
CHAPTER 3: <u>FIELD INSTALLATION, FIELD MEASUREMENT AND DATA RECORDING.</u>	52
3.1 Installation of the pressure cells	52
3.2 The soil formation	59
3.3 Measurement of the changes in the tunnel diameter	59
3.4 Data recording	59
CHAPTER 4: <u>ANALYSIS OF THE DERIVED DATA.</u>	67
4.1 Analysis of the first experiment results	67
4.2 Analysis of the second experiment results	72
4.3 Analysis of the tunnel diameter measurements	81
4.4 Application of tunnel-soil contact pressure theories to the tunnel situation currently considered	88
4.5 Notable case histories of tunnel-soil contact pressure measurements	91

	Page
CHAPTER 5:	
<u>THEORETICAL STUDY OF THE EFFECT OF LINING-SOIL STIFFNESS ON THE DISTRIBUTION OF THRUST AND BENDING MOMENT IN THE LINING.</u>	100
5.1 Introduction	100
5.2 Rigid lining	100
5.3 Flexible lining	101
5.4 Semi-flexible or semi-rigid lining	101
CHAPTER 6:	
<u>SUMMARY AND CONCLUSIONS.</u>	114
6.1 Summary	114
6.2 Conclusions	114
<u>APPENDIX A: Theories taking the effect of tunnel depth into consideration</u>	116
<u>APPENDIX B: Theories disregarding the effect of tunnel depth.</u>	121
<u>REFERENCES</u>	127

List of Figures.

		Page
1	Site plan	3
2	Map of north-east England	4
3	Section through the tunnel lining	6
4	Sections through a lining segment	7
5	Electric strain gauge earth pressure cell ( <u>after</u> Peattie and Sparrow, 1954)	9
6	Electric strain gauge earth pressure cell ( <u>after</u> Brown and Pell, 1967)	9
7	Vibrating wire pressure cell ( <u>after</u> Thomas and Ward, 1969)	11
8	Vibrating wire earth pressure cell ( <u>after</u> Bjerrum, Kenny and Kjaernsli, 1965)	11
9	Vibrating wire earth pressure cell ( <u>after</u> Shepherd, 1967)	13
10	Glötzl earth pressure cell	13
11	Section through the type of cell used in the first sequence of experiments	16
12	The pressure cells used in the first experiment	17
13	One of the pressure cells used in the first experiment	17
14	Section through the type of cell used in the second sequence of experiments	18
15	The pressure cells used in the second experiment	19
16	One of the pressure cells used in the second experiment	19
17	Effect of cell geometry and cell-soil stiffness on the cell error ( <u>after</u> Peattie and Sparrow, 1954)	21
18	Effect of flexibility factor on the cell error ( <u>after</u> Tory and Sparrow, 1967)	21

19	The cell used in hydraulic calibration	26
20	The pressure system used in calibration	26
21-26	Calibration charts for the pressure cells used in the first experiment	27-32
27	Particle size distribution of the sand used in calibration	35
28	Section through the calibration tank	36
29	The machine used in calibration	37
30	The calibration tank	37
31	Effect of thickness of the sand cover on the cell output	38
32	Pressure-output using different sand cover	38
33-38	Calibration charts for the pressure cells used in the second experiment	41-46
39	Section through the calibration tank showing position of clay cylinder	47
40	Position of cells (first experiment)	53
41	Position of cells (second experiment)	54
42	Pressure cells Nos. 2 and 3 in the first experiment	55
43	View of the tunnel showing the box used for the protection of the electronic equipment	55
44	Electronic equipment used for the data recording in the first experiment	56
45	Pressure cells Nos. 3 and 4 in the second experiment	56
46	Pressure cell no. 2 in the second experiment	57
47	Electronic equipment used for the data recording in the second experiment	57
48	Power supply, voltmeter and connecting box	58
49	The six-channel recorder used for the data recording	58
50	Record of borehole No. C1	60



	Page	
51	Record of borehole No. H53	61
52	Position of steel plates, the steel plate and the measurement bar used in the tunnel diameter measurements	62
53	Measuring of the tunnel diameter changes	63
54	" " " " "	63
55	Pressure-time curves for the pressure cells Nos. 1 and 4	68
56	Pressure -time curve for the pressure cells Nos. 2 and 3	68
57	Pressure-time curve for the pressure cells Nos. 5 and 6	69
58	Pressure distribution around the tunnel lining one day after its construction	70
59	Pressure distribution around the tunnel lining two days after its construction	70
60	Pressure distribution around the tunnel lining five days after its construction	71
61	Final pressure distribution around the tunnel lining (first experiment)	71
62	$P/P_{max}$ % and $P/\gamma H$ % = time curve of pressure cell 1	73
63	" " " " " " " 2	73
64	" " " " " " " 3	74
65	" " " " " " " 4	74
66	" " " " " " " 5	75
67	" " " " " " " 6	75
68	Pressure-time curve for the pressure cells Nos. 1 and 6 (second experiment)	76
69	Pressure-time curve for the pressure cells Nos. 2 and 5 (second experiment)	77
70	Pressure-time curve for the pressure cells Nos. 3 and 4(second experiment)	78

	Page	
71	Pressure distribution around the tunnel lining one day after its construction(second experiment)	79
72	Pressure distribution around the tunnel lining two days after its construction (second experiment)	79
73	Pressure distribution around the tunnel lining five days after its construction (second experiment)	80
74	Final pressure distribution around the tunnel lining (second experiment)	80
75	$P/P_{max}$ % and $P/\gamma H$ % - time curve of pressure cell 1	82
76	" " " " " " 2	82
77	" " " " " " 3	83
78	" " " " " " 4	83
79	" " " " " " 5	84
80	" " " " " " 6	84
81	Final deformation of tunnel lining	85
82	The changes of the tunnel diameter-time curves	86
83	Pressure-time curve of a tunnel in Chicago plastic clay	93
84	Deformation-time curve of the tunnel lining (Chicago subway)	93
85	Deformation of the tunnel lining (Chicago subway)	93
86	The changes in the horizontal and vertical tunnel diameter at site 'B'	94
87	Section through the tunnel lining at site 'B'	94
88	Stress-time curve at site 'B'	94
89	The changes in the horizontal and vertical tunnel diameter at site 'A'	95
90	Section through the tunnel linings at site 'A'	95

		Page
91	Stress-time curve at site 'A'	95
92	Thrust-time curve for the two observation points	98
93	Section through the tunnel lining	98
94	Pressure distribution on a rigid lining	102
95	Straining actions diagram	104
96	Stresses distribution and displacements in the medium and the shell	107
97	Medium and lining under a state of uniform compression	109
98	Medium and lining under a state of pure shear	109
99	Variation of thrust coefficient with compressibility ratio and flexibility ratio	112
100	Variation of moment coefficient with flexibility ratio	113
101	Variation of diameter change with flexibility ratio	113

List of Tables

		Page
1	Results of calibration tests for the pressure cells using hydraulic pressure (first experiment)	33
2	Results of calibration tests for the pressure cells using dry sand as a testing medium	39
3	Results of temperature calibration tests.(first experiment)	39
4	Results of calibration tests for the pressure cells using dry sand as a testing medium	48
5	Results of temperature calibration tests (second experiment)	48
6	$C_p$ , $C_t$ , R, T and calibration equations of the pressure cells used in the first experiment	50
7	$C_p$ , $C_t$ , R, T and calibration equations of the pressure cells used in the second experiment	51
8	Results of laboratory tests	64
9	Overburden pressure, maximum measured pressure, and $\frac{P_{max}}{\gamma H}$ % of the pressure cells (first experiment)	65
10	Overburden pressure, maximum measured pressure and $\frac{P_{max}}{\gamma H}$ % of the pressure cells (second experiment)	66
11	The changes in the tunnel diameter	87
12	Particulars of tunnel linings	96
13	Comparison between the experimental results	99
14	Strength coefficient 'f' ( <u>after</u> Protodyakonov)	126

## Units and Symbols.

In this thesis quantities are expressed in both Imperial and metric units as follows:

### Imperial units

in.	inch or inches
ft	foot or feet
lbf/in <sup>2</sup>	pounds force per square inch
lbf/ft <sup>2</sup>	pounds force per square foot

### Metric units

mm.	millimetre or millimetres
cm.	centimetre or centimetres
m	metre or metres
kgf/cm <sup>2</sup>	kilograms force per square centimetre
kN/m <sup>2</sup>	kilonewtons per square metre

### Acknowledgements

The author is indebted to Dr. P.B. Attewell, his supervisor, for much helpful advice and guidance during the course of this study. The author would also like to express his gratitude to Dr. I.W. Farmer (now Reader in Mining Engineering, University of Newcastle upon Tyne) for his valuable assistance, particularly in the organisation of the field work.

Thanks are also due to various members of the technical staff in the Engineering Geology Laboratories for their assistance during the period of this project, in particular to Mr. A. Swann, who constructed all the bodies of the pressure cells, and to Mr. C.B. McEleavey and Mr. P. Key for their valuable help both in the field and in the laboratory.

The Northumbrian Water Authority kindly gave permission and made provision for the pressure cell installations in the two tunnel locations. Particular thanks are due to Mr. P.G. Gough (Resident Engineer, N.W.A.) and to Contractors (Messrs. Charles Brand Ltd.).

## CHAPTER 1

### INTRODUCTION

#### 1.1 General introduction.

One of the most important problems which arises during the design and construction of tunnel linings is the estimation of the ground pressures acting on the lining after its construction and the time after which the lining deformation is terminated.

Many theories have been developed for the evaluation of such pressures, but field measurements of ground-lining interaction pressure and lining deformation are still one of the most reliable methods of obtaining specific design data. One of the common methods of measuring the contact pressures involves the use of pressure cells. It is well known that the accuracy and reliability of the measured data are directly influenced by many factors, among which are the design concept and quality, laboratory calibration, field installation, and the data recording technique. The importance of each of these factors will be discussed in the context of a specific case history of pressure measurement.

The theories developed for the evaluation of soil-structure interaction pressure can be classified into two main groups: theories taking into consideration the effect of tunnel depth, and theories disregarding the effect of tunnel depth. The first group is represented in Appendix A by Bierbaumer theory and Terzaghi theory. The second group is represented in Appendix B by Kommerol theory and Protodyakonov theory.

In the last few years, theoretical study of the underground structure-soil interaction problems has become possible through the development of the

finite element method which represents the most sophisticated analytical technique presently available. The accuracy and the value of the results obtained by applying such a method depend on how well the adopted mathematical model represents the complexity of the problem in question.

It is well known that the lining-soil relative stiffness does affect the distribution of bending moment and thrust through the lining section. Accordingly, it must also influence the amount of lining deformation and the time necessary for such deformation to cease. The tunnel lining can be classified, according to its stiffness, into two types: a flexible lining and a rigid lining. The effect of lining stiffness on the bending moment and thrust distribution will be discussed in more detail in Chapter 5.

Two field experiments in the locations shown in Figure 1 were carried out in order to investigate this general problem. Six pressure cells were designed and constructed for each of two in situ experiments, aimed specifically at measuring radial contact pressures at different points behind the lining of a tunnel in mixed ground (stony clay, laminated clay) on the north bank of the River Tyne in north-east England. The location is shown in Figure 2.

The tunnel in question is 3.20 m (10'6") diameter, hand-driven without a shield. This method of working greatly facilitated installation of the gauges. The function of the tunnel, which forms part of the Northumbrian Water Authority's new multi-million pound scheme for updating the sewerage facilities in Greater Tyneside, is to convey sewage along the final length of the North-bank interceptor sewer to the treatment plant sediment settlement tanks at Howdon.



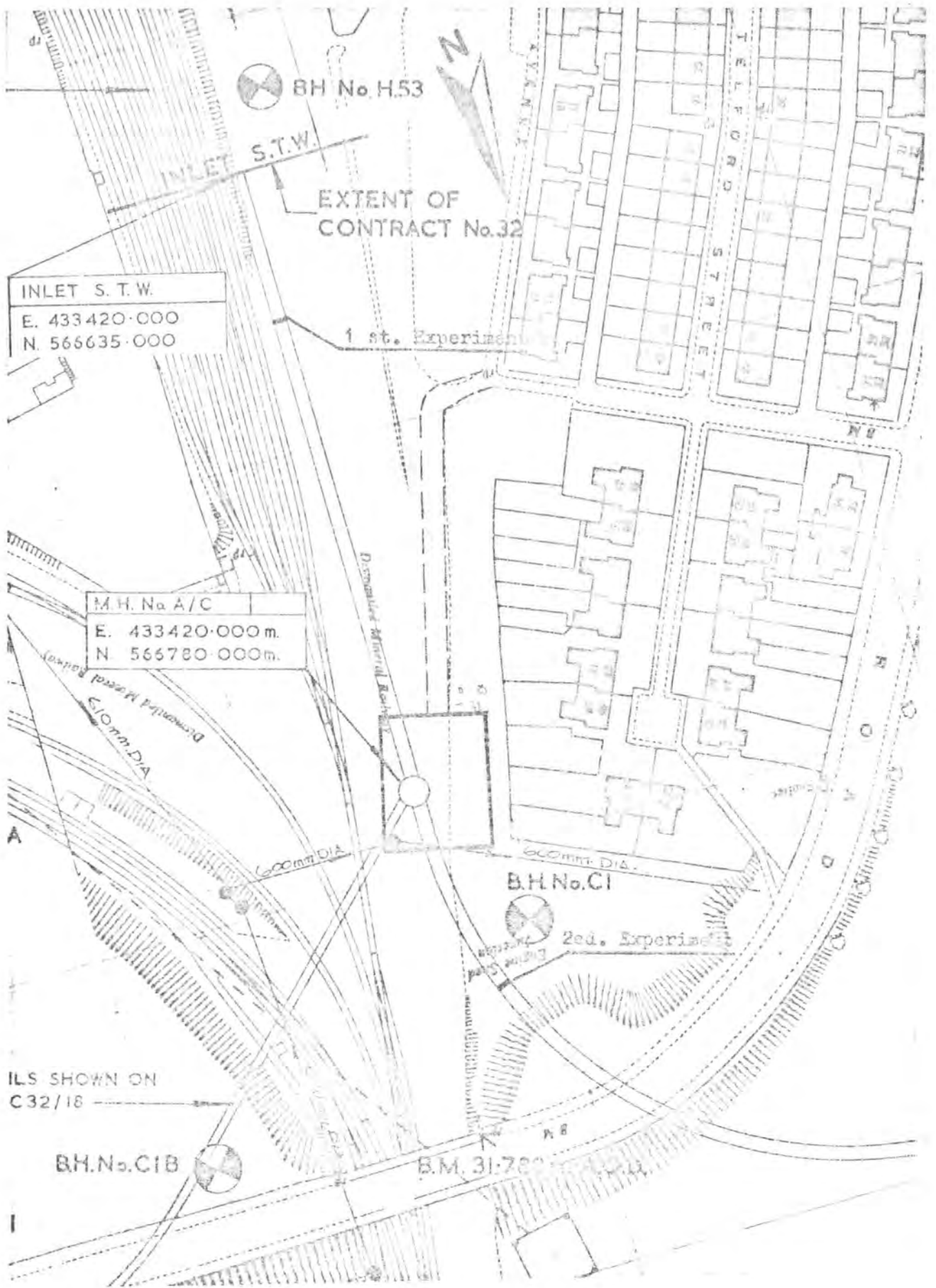


Figure 1 Site plan



Figure 2 Map of North East England

The pre-cast segmental tunnel lining consists of 61 cm (2ft) wide rings, each comprising six segments and a key as shown in Figures 3 and 4. The aim was to install the pressure cells at the time of the lining erection and to recover the sensor elements of each of the cells for re-use when the secondary brick lining for the tunnel was built several months later. This recovery operation is a fundamental feature of the low-cost cell design to be described subsequently.

During the design of a pre-cast R.C. lining, many factors should be taken into consideration. Among these factors is the requirement that the lining should be designed to withstand the expected outer pressure taking into consideration a reasonable factor of safety. There must also be an economy of production of the pre-cast segments, and the segments should be strong enough to withstand the rough handling received during the erection of the lining ring. Before the start of this research, it was previously known that the R.C. lining used in this tunnel was quite strong enough to resist the expected outer pressure, but the points that this present research covers relate to the distribution of the lining-soil interaction pressure, the order of lining deformation, and the time needed for this deformation to terminate.

Using these results, the period that should be left between the erection of the primary R.C. lining and the building of the secondary brick lining may be specified from a rather more scientific base. Current practice is to defer secondary brick lining construction for several months following primary lining erection, but if it can be shown that radial pressure transfer from soil to lining ceases much earlier - and hence, by implication, that the consequential deformations terminate earlier - then secondary lining construction could well proceed much sooner at a more

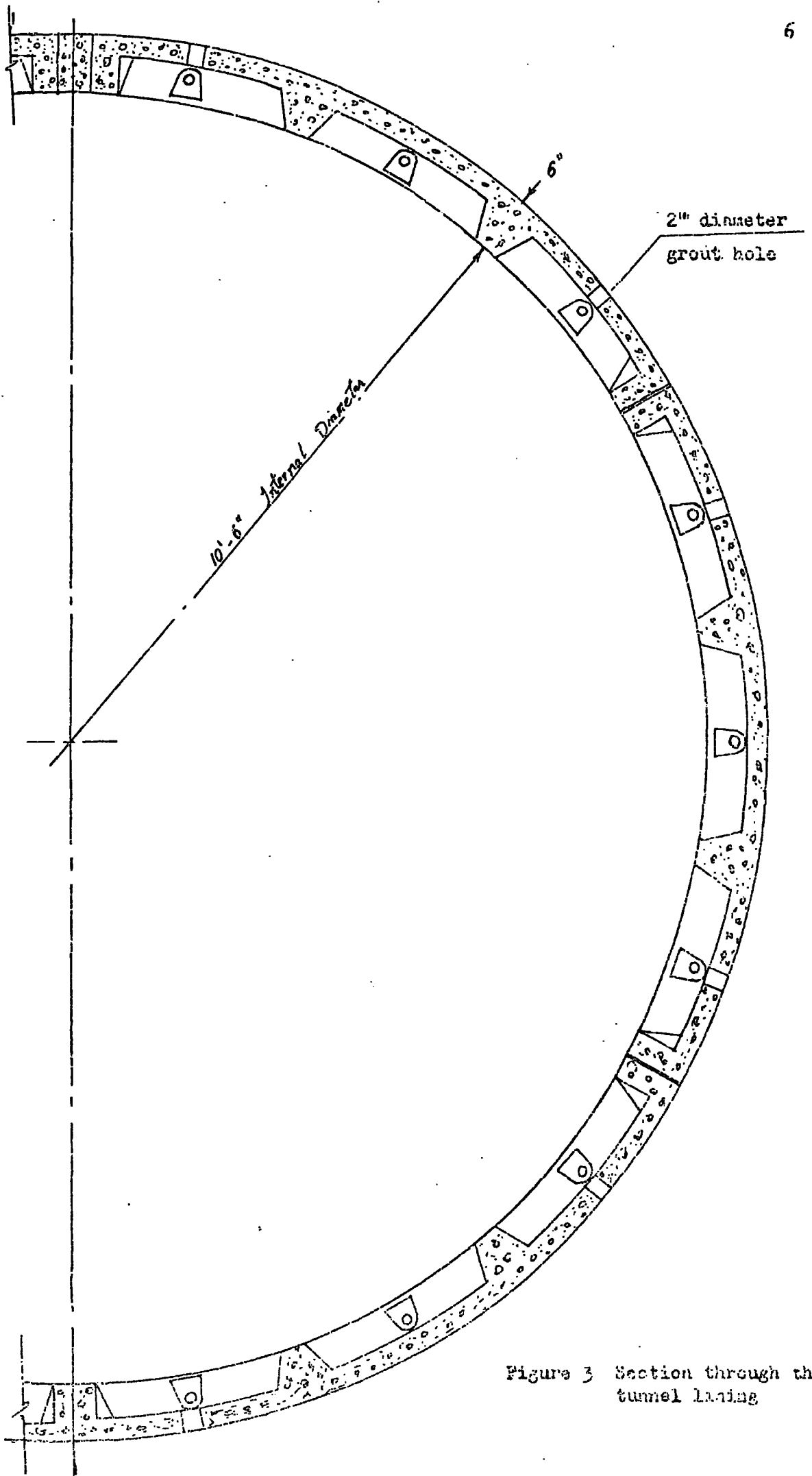


Figure 3 Section through the tunnel lining

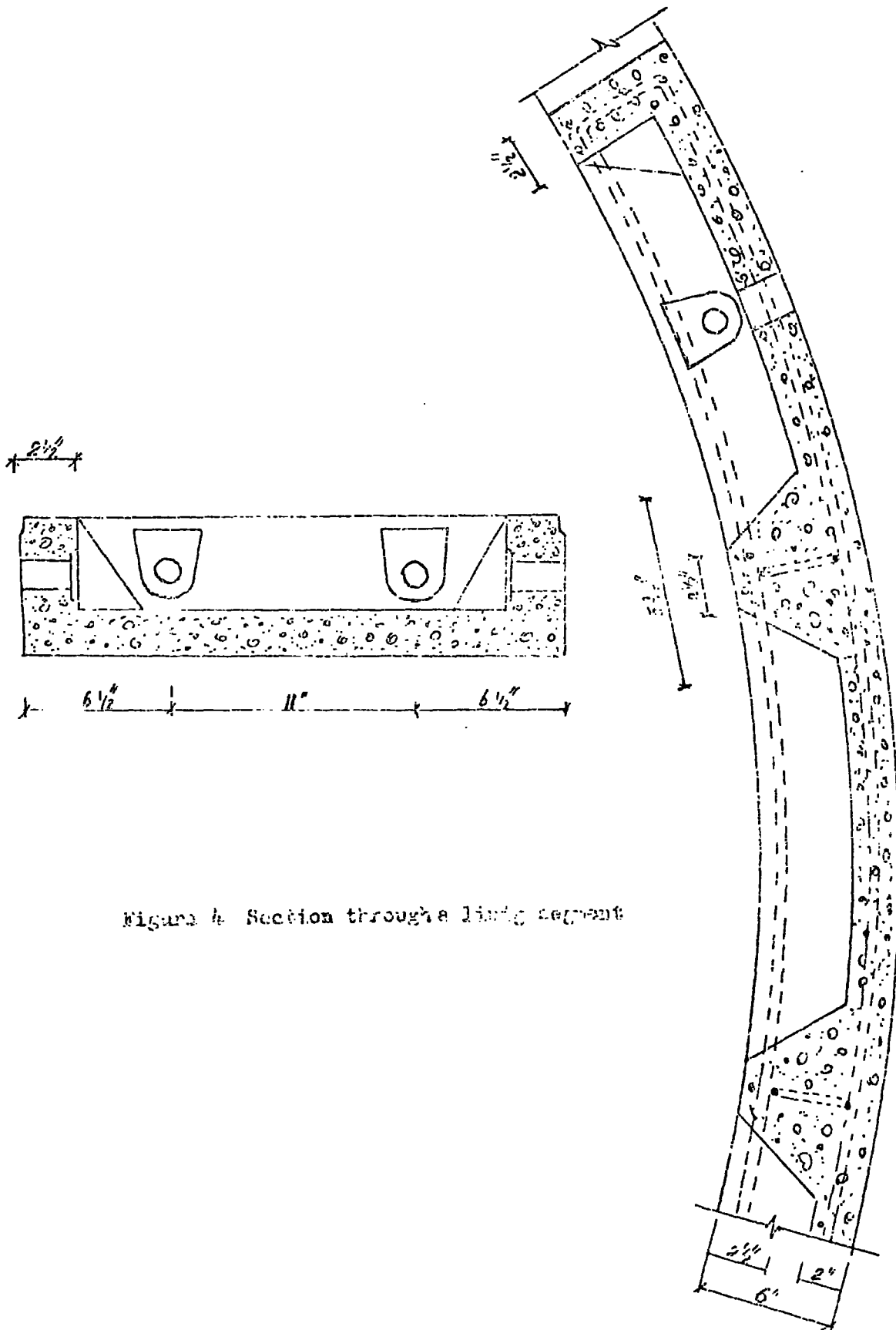


Figure 4 Section through a lining segment

convenient time when the full complement of supporting equipment of the contractor is still on site.

1.2 General types of pressure cells.

Pressure cells may be classified into two general types: a) diaphragm-type pressure cells and b) hydraulic-type pressure cells.

a) Diaphragm-type pressure cells:

The theory of this type of pressure cell is based on measurement of the deflection of a sensing diaphragm, activated by the external pressure to be measured. Measurement sensing may be by one of the following two systems:

1. Strain gauge system:

In this type of pressure cell, the deflection of the sensing diaphragm is measured by using a number of strain gauges (generally not less than four) mounted on the diaphragm and connected in bridge format. Figure 5 shows the electrical strain gauge earth pressure cell designed by Peattie and Sparrow (1954) with the strain gauges arranged in a configuration of two central tension gauges and two edge compression gauges. The accuracy of this cell was influenced by cross-stresses; these are stresses acting in the plane of the sensing diaphragm. In order to avoid the errors occurring as a result of cross-sensitivity, Brown and Pell (1967) suggested a new arrangement of the strain gauges, as shown in Figure 6. The strain gauges were arranged in three directions at 45°. With this arrangement, the errors due to cross-sensitivity were minimized.

Wong (1974) proves theoretically and experimentally that to avoid the effect of non-uniform pressure distribution, only gauges near to the edge of the sensing diaphragm should be used, with a minimum of four at intervals of 90°. The use of a minimum of four edge gauges, equally

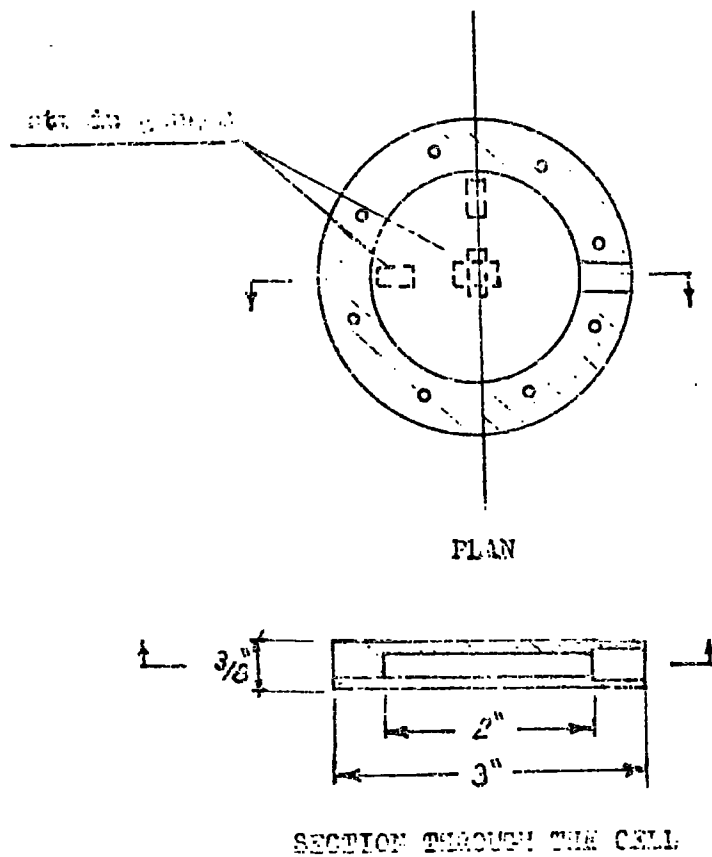


Figure 5 Electrical strain Gauge earth pressure cell  
(after Pettit and Sparrow, 1954)

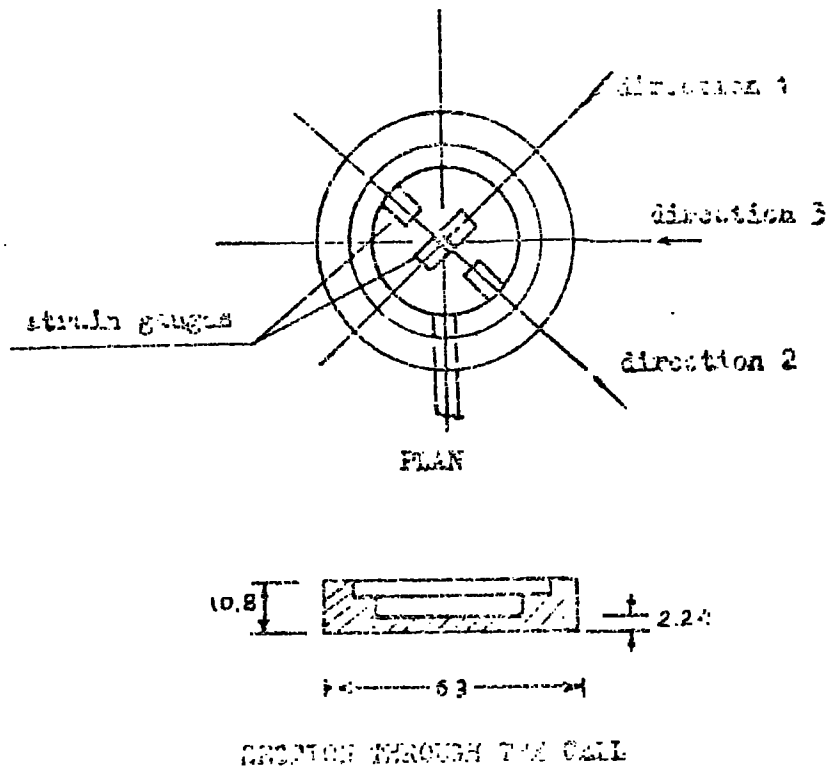


Figure 6 Electrical strain gauge earth pressure cell  
(after Pettit and Sparrow, 1954)

spaced, tends to minimize any effect of localized excess load directly over any one of them.

Generally, with this type of pressure cell, it is recommended that the area of the sensing diaphragm should be as large as practicable, since this facilitates the accurate positioning of the strain gauges and reduces the percentage error.

## 2. Vibrating wire system:

The cell generally consists of a rigid supporting plate, rigid supporting ring and a sensing diaphragm which is designed to respond to the ground pressure. The diaphragm has two projecting arms between which the vibrating wire is stretched (as shown in Figure 8). The deflection of the diaphragm - resulting from the applied pressure - causes a slight rotation to the arms, and this changes the stress in the vibrating wire and thus its frequency. Finally, by using calibration charts, the average value of earth pressure acting on the cell diaphragm can be evaluated.

Figure 7 represents a vibrating wire pressure cell designed by Thomas and Ward (1969). This cell consists of two metal diaphragms bolted together to form the body of the cell. The vibrating wire is stretched between two arms located at the points of maximum rotation (at a distance of  $\sqrt{3}/2$  times the diaphragm diameter from the centre). Using this cell, changes in pressure as small as  $5 \text{ kN/m}^2$  were measured.

Figure 8 shows a vibrating wire pressure cell designed by Bjerrum, Kenny and Kjaernsli (1965), mainly for the measurement of sheet pile-soil interaction pressure.

Figure 9 illustrates a vibrating wire pressure cell designed by Shepherd (1967). This cell consists of two welded steel plates of 15 cm



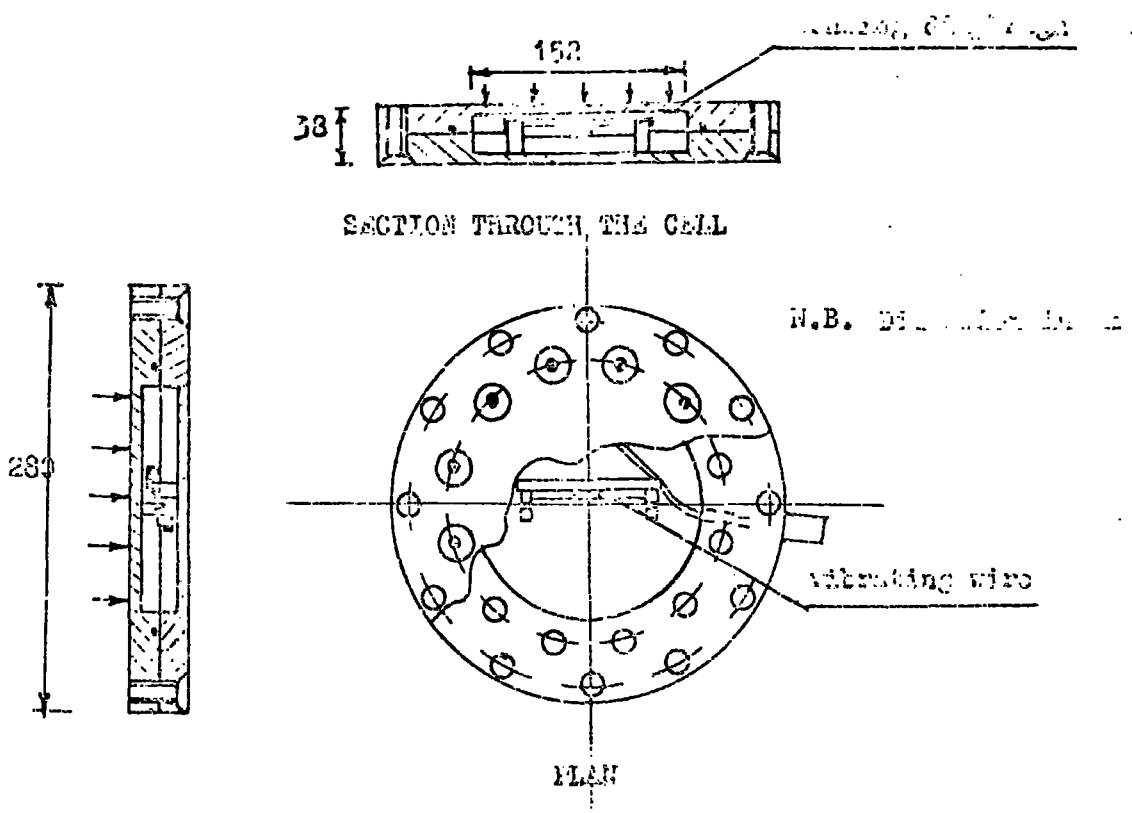


Figure 7 Vibrating wire pressure cell  
 (after THOMAS and WOOD, 1959)

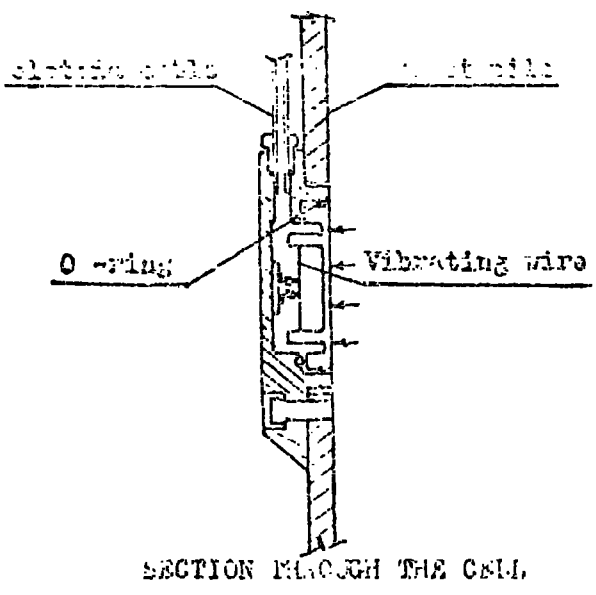


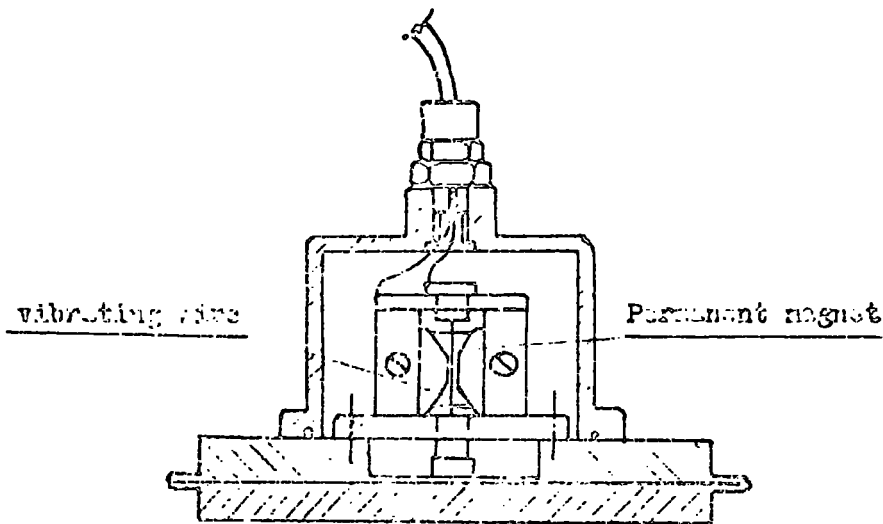
Figure 8 Vibrating wire earth pressure cell  
 (after BARNETT, KENNY and MURPHY, 1965)

diameter, the vibrating wire being stretched between the upper plate and a supporting frame fixed to the body of the cell. The deflection of the plate, as a result of any external pressure, causes a change of stress in the wire and so its frequency, and by using the calibration charts the acting pressure may be evaluated.

b) Hydraulic-type pressure cell:

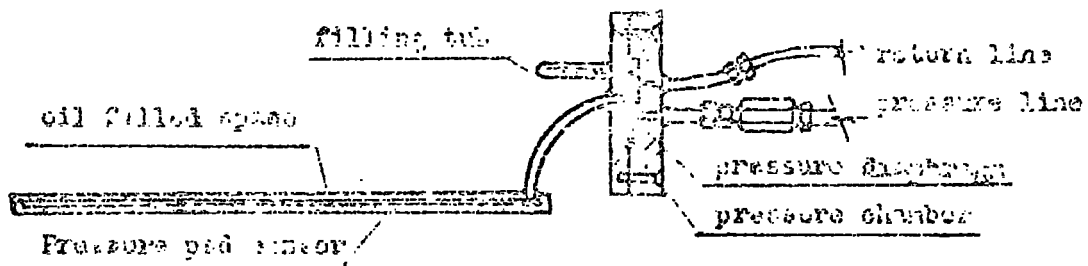
The most common type of hydraulic earth pressure cell is the Glötzl cell. As shown in Figure 10 the cell has a thin sensing pressure pad of high area-to-thickness ratio in order to minimize the effects of stress distortion caused by the difference between the stress-strain characteristics of the sensing pad and those of the soil. The external pressure acting on the sensing pad is determined by measurement of the compensating hydraulic pressure. This can be achieved by the following procedure:

- i) the sensing pad and the pressure chamber are filled with oil by pumping it through the filling tube;
- ii) the primary pressure (zero gauge reading) inside the sensing pad and the pressure chamber is determined by applying pressure through the pressure line. When the pressure line exceeds the pad pressure, the pressure diaphragm deflects and allows oil to flow in the return line. This means that the pressure in the line cannot exceed the cell pressure, and hence the cell pressure is equal to the line pressure at the entrance to the bypass orifice.
- iii) After installation of the cell, the oil in the pad and the pressure chamber is pressurized as a result of the surrounding earth pressure. The earth pressure is equal to the pressure line gauge reading minus zero gauge reading plus gauge elevation correction  $\gamma_o h$ , where  $\gamma_o$  is the specific gravity of the oil and  $h$



SECTION THROUGH THE CELL

Figure 9 Vibrating wire earth pressure cell  
(after SLEPNER, 1967)



SECTION THROUGH THE CELL

Figure 10 Crystal earth pressure cell

is the difference in elevation between the cell and the pressure gauge.

c) Pressure cell used in the present study:

The pressure cell used in this present study is considered as a combination of both the diaphragm and the hydraulic type of cell. This arises because the deflection of the primary sensing diaphragm, caused by the external pressure, creates a pressure in an oil medium, the latter itself then causing a secondary deflection of a sensing diaphragm within an electrical transducer. Fundamental features of the system are the design of the primary diaphragm stiffness, the low volume of the oil medium, and the recovery facility for the expensive electrical transducer head when the recording work is completed. The design and calibration of such a pressure cell are given in detail in Chapter 2.

## CHAPTER 2

### DESIGN, CONSTRUCTION AND CALIBRATION OF THE PRESSURE CELL USED IN THE PRESENT STUDY.

#### 2.1 Design of the pressure cell used in the present study

The function of a pressure cell is to measure the total earth pressure acting on it. Earth pressure measurements can be classified into two general types: pressure in a soil mass and pressure on the boundary at the soil-structure interface.

The pressure cells used in this present study for a first sequence of experiments were designed in the form and dimensions shown in Figures 11, 12 and 13, to effect mainly the second type of measurements.

Each cell is composed of three main parts: part "A" which represents the steel body of the cell and consists of the sensing diaphragm which is fixed to a rigid circular ring and a supporting steel plate; part "B" which represents the connecting pipe, its length depending on the lining thickness; and part "C" which represents the electrical pressure transducer the most valuable and expensive part of the cell. The body of the cell is completely filled with very low compressibility oil to act as the pressure transmitting medium. On the basis of the experience gained from the first experiment, the cell design was modified (as shown in Figures 14, 15 and 16) by adding part "D", the cell holder. The new design allows the adjustment of the position of the cell sensing diaphragm so that it is in direct contact with the soil. The effect of the non-uniformity of the grout thickness (resulting from uneven over-cutting during hand excavation of the clay) around the tunnel lining can thus be minimized.

According to previous research and experience in the field of pressure cell design, the following factors and principles were taken into

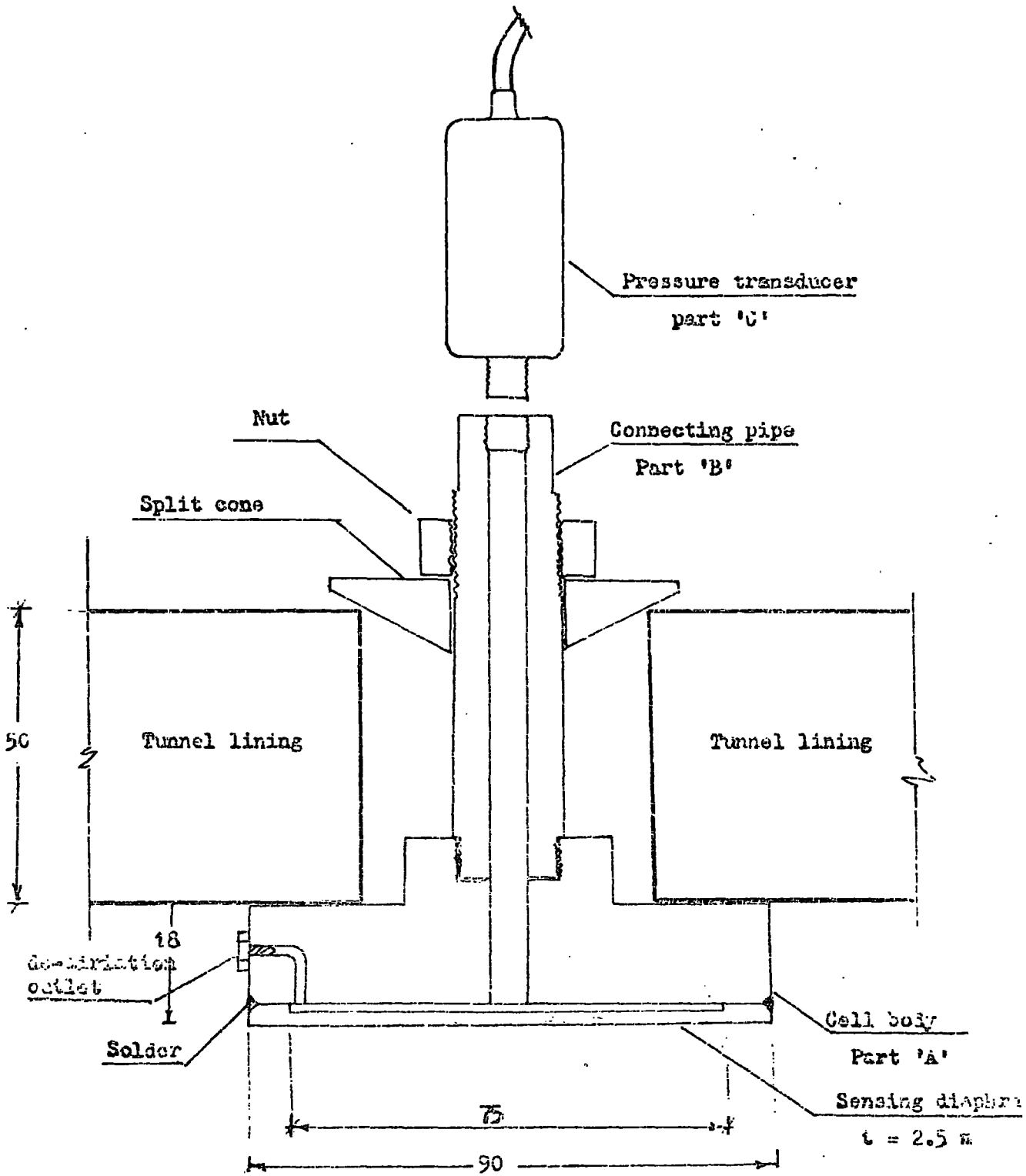


Figure 11 Section through the type of coil used in the first sequence of experiments.

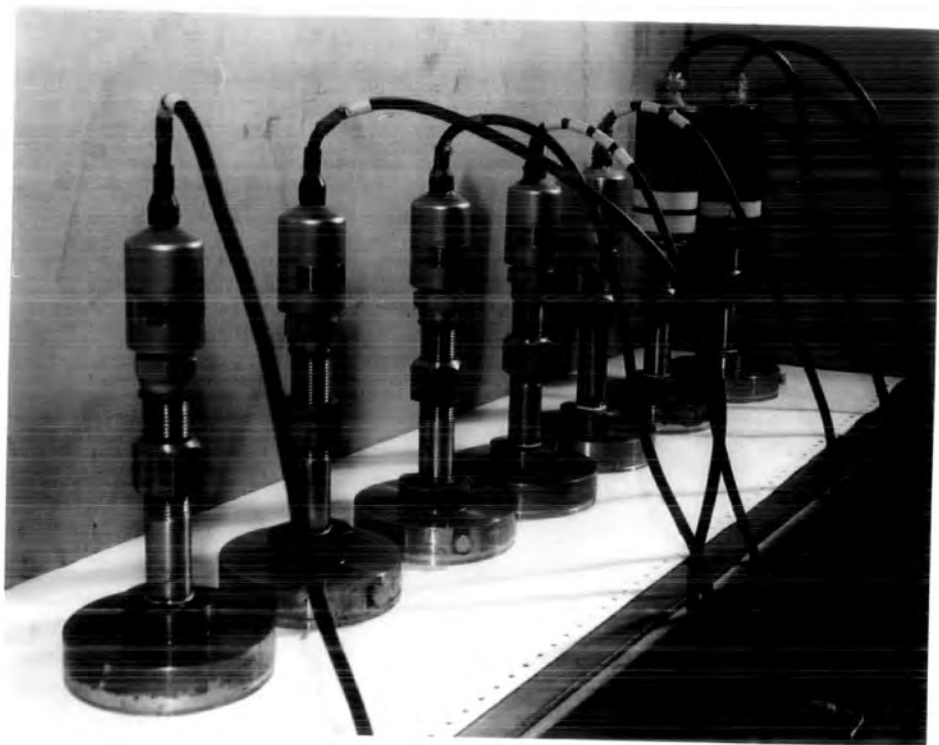


Figure 12 The pressure cells used in the first experiment



Figure 15 One of the pressure cells used in the first experiment

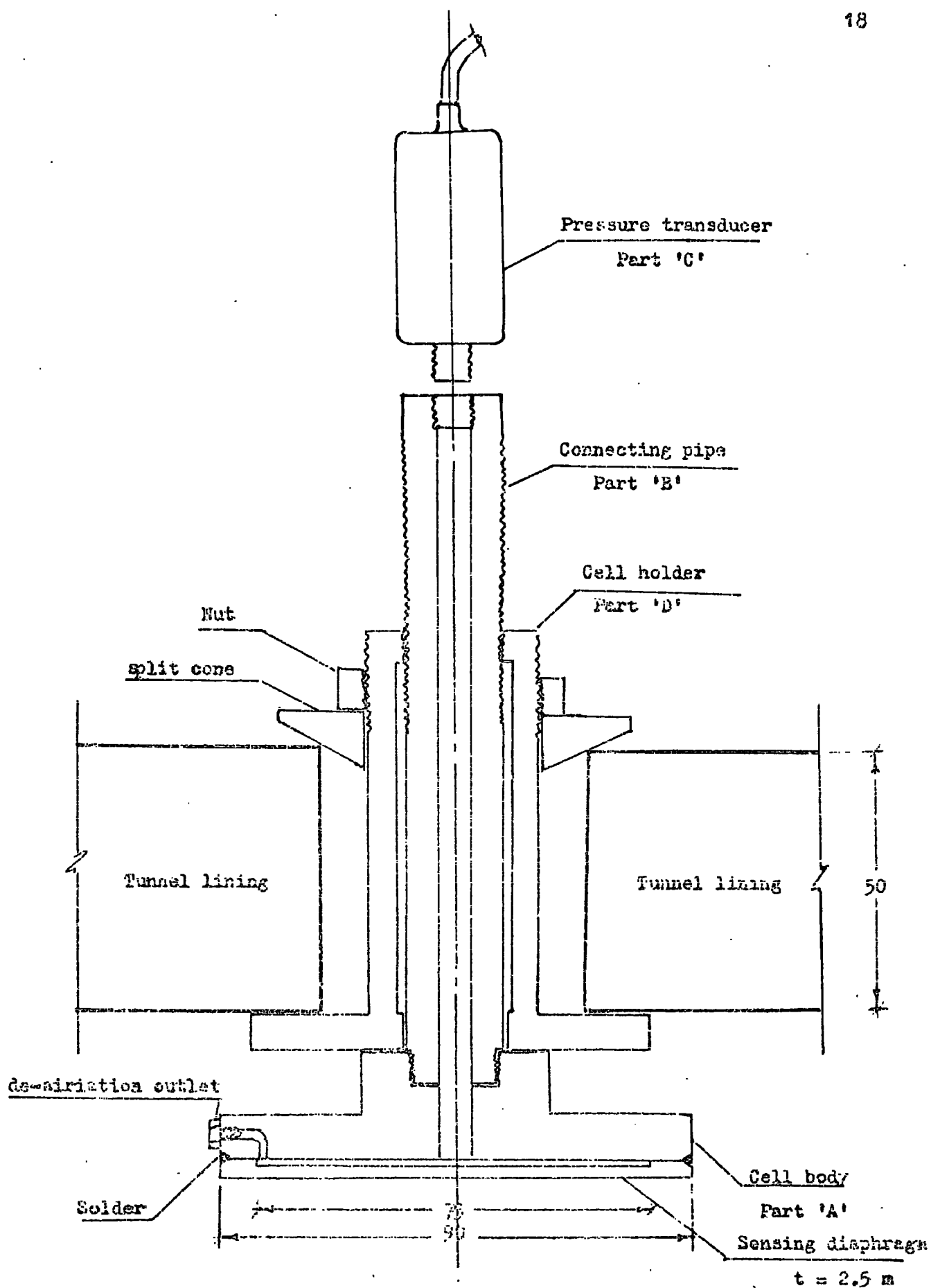


Figure 14. Section through the type of cell used in the second sequence of experiments.



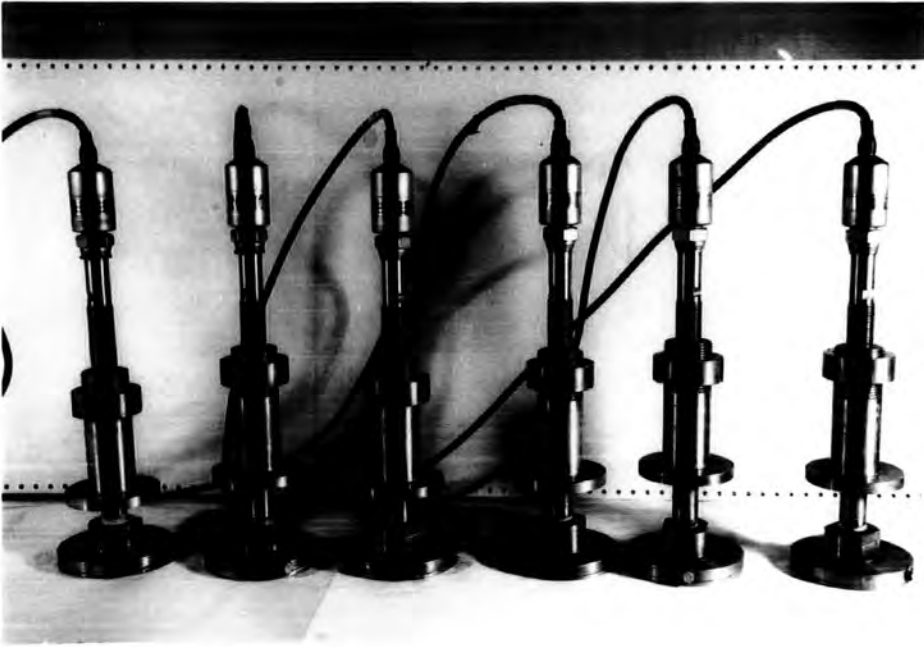


Figure 15 The pressure cells used in the second experiment



Figure 16 One of the pressure cells used in the second experiment

consideration:

a) The sensitivity of the cell should be consistent with the stress level to be measured.

b) It is well known that the stresses measured by a given cell depend to a great extent on the relative stiffness of the cell and the soil in which it is placed. Previous studies have proved that the error in pressure measurements using pressure cells is directly influenced by cell geometry and cell-soil stiffness, as shown in Figures 17 and 18 (after Peattie and Sparrow, 1954 and Tory and Sparrow, 1967 respectively). Many of the soil-cell interaction problems with the pressure cell can be minimized if the ratio between the pressure cell thickness ( $t$ ) and the diameter ( $D$ ) is small and its stiffness is high ( $t/D < 0.2$  - Waterways Experiment Station, 1944).

c) Many research results have suggested that the deflection ( $\delta$ ) at the centre of the cell-sensing diaphragm should not exceed a certain value ( $\delta / D < 1/2000$  - Waterways Experiment Station, 1944).

d) In order to obtain representative pressure measurements, the diameter of the cell-sensing diaphragm ( $D$ ) should be at least 50 times the maximum particle size of the soil in which the cell is placed (Kallstenios and Bergau, 1956).

e) The maximum skin stress in the diaphragm must be less than the allowable stresses in the cell material.

f) The cell must be of low thermal sensitivity or at least be easily corrected for temperature changes. Accordingly, for the present cells, detailed calibration tests were performed to evaluate a temperature correction factor ( $C_t$ ).

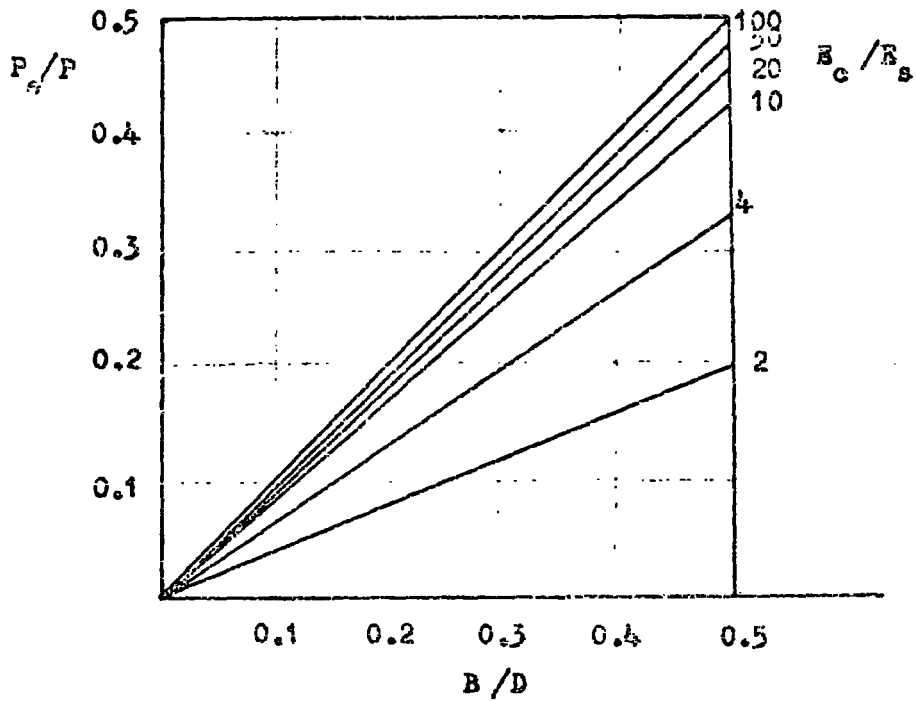


Figure 17 Effect of cell geometry and cell-soil stiffness on the cell error (after Peattie and Sparrer, 1954 ).

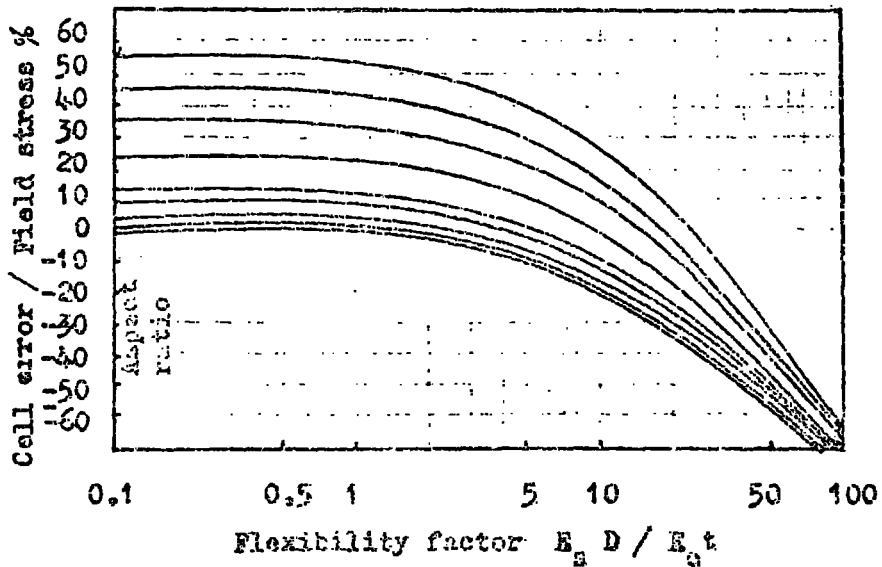


Figure 18 Effect of flexibility factor on the cell error (after Tory and Sparrer, 1957).

g) The cells were designed, as shown in Figures 11 and 14, in such a way that the part "A" will be installed on the clay-contact side of the tunnel linings with the sensing diaphragm facing the soil. The pressure transducer remains inside the tunnel during the whole period of field data recording. Such an arrangement improves the reliability of the system and permits recovery of the expensive transducer element once the field measurement programme is terminated.

### 2.1.1. Calculation of Design Pressure:

For design purposes, the maximum possible radial pressure may be taken as the overburden pressure ( $\gamma h$ ). Since, at the installation point,

$$h = 13,00 \text{ m and } \gamma = 2,1424 \text{ t/m}^3$$

then,

$$\begin{aligned} \text{maximum radial stress} &= 13,00 \times 2,1424 \\ &= 27,9 \text{ tf/m}^2 \\ &= 2,79 \text{ kgf/cm}^2 \end{aligned}$$

Taking a factor of design safety of 1.5, the design pressure will then be  $4 \text{ kgf/cm}^2$  ( $\approx 400 \text{ kN/m}^2$ ).

### 2.1.2. Calculation of the diaphragm thickness:

It has been recommended, as mentioned before, that the ratio between the maximum deflection at the centre of the sensing diaphragm " $\delta$ " and its diameter " $D$ " should not exceed  $1/2000$ .

The relation between the deflection " $\delta$ " and the applied pressure " $p$ " is given by the following equation:

$$p = \delta \frac{96Et^3}{D^4} \quad (\text{after Hanna, 1973})$$

Therefore, for the condition of  $\delta/D \ll 1/2000$ , the maximum allowable pressure

$$P_{\text{max}} = \frac{96 E}{2000} \left( \frac{t}{D} \right)^3$$

where  $t$  is the diaphragm thickness and  $E$  is the Young's modulus of the diaphragm material.

$$\text{Thus, } t = \sqrt[3]{\frac{2000 D^3 P_{\max}}{96 E}}$$

Therefore, for

$$E = 2.1 \times 10^6 \text{ Kgf/cm}^2$$

$$P_{\max} = 4 \text{ Kgf/cm}^2$$

$$D = 7.4 \text{ cm,}$$

we have that

$$t = 0.2558 \text{ cm.}$$

### 2.1.3. Check for diaphragm skin stress

The maximum skin stress at the diaphragm centre " $f_d$ " is given by the following equation:

$$\begin{aligned} f_d &= 3/16 \left( P \left( \frac{D}{t} \right)^2 \right) \quad (\text{after Hanna, 1973}) \\ &= 3/16 \times 4 \left( \frac{7.4}{0.25} \right)^2 \\ &= 675 \text{ kg f/cm}^2 \end{aligned}$$

This value is less than  $1400 \text{ kgf/cm}^2$  and the design is thus well within tolerable limits.

### 2.1.4. Calculation of volume change

The equation of the deflection curve of the sensing diaphragm is given by:

$$\delta = \frac{P(a^2 - r^2)^2}{6 E t^3} \quad \dots\dots(1)$$

If  $dV$  is the incremental volume displaced by the diaphragm over a surface incremental area of  $2\pi r dr$  (see Figure 10a),

$$dV = 2\pi r \delta dr$$

Then, the total volume change over the whole area of the diaphragm  $V$  is given by:

$$V = \int_0^a \delta 2\pi r dr \quad \dots\dots(2)$$

From equation (1) and (2) we get

$$\begin{aligned}
 V &= \int_0^a \frac{2P(a^2 - r^2)^2}{6Et^3} \pi r \, dr \\
 &= \pi Pa^6 / 18 Et^3 \\
 &= \pi \times 4 \times 3.7^6 / 18 \times 2.1 \times 10^6 \times 0.25^3 \\
 &= 0.05459 \text{ cm}^3
 \end{aligned}$$

This volume is less than 0.2 to 0.3 cm<sup>3</sup> and is, therefore, satisfactory, based on an allowable volume change in the transducer as used of 0.2 to 0.3 cm<sup>3</sup>.

## 2.2 Construction of the pressure cells.

Each of the pressure cells consists mainly of three parts for the cells used in the first experiment, or four parts for the cells used in the second experiment. Part "A" in both types, which represents the cell body, had been constructed from a 92 mm diameter steel bar in the form and dimensions shown in Figures 11 and 14. Part "B" in both types, which represents the connecting tube, was constructed from 20mm steel bar. The length of the connecting tube depends mainly on the thickness of the lining; in the case of the first experiment, the length of the tube was 120 mm, and in the case of the second experiment it was 210 mm.

Parts A and B were connected together to form the steel body of the cell. A special type of sealing tape was used around the connecting screw in order to minimize any tendency for leaking. Part "C" represents the electrical pressure transducer having a range of 100 lb f/in<sup>2</sup> (689.5 kN/m<sup>2</sup>). Both the cell body and the pressure transducer were completely filled with oil before actually fitting the pressure transducer to the cell and a soft copper washer, in addition to the special sealing tape, was used to seal the connecting screw.

During the filling of the cell body with oil, de-aeration was accomplished via the screw outlet at the side of the cell base. The screw outlet was also used to adjust the initial pressure inside the cell, after the fitting of the transducer; this was attained by releasing the oil through the screw outlet.

Part "D" of the cells used for the second experiment was constructed from 50 mm steel bar.

### 2.3 Laboratory Calibration.

Each of the pressure cells used in the first experiment was calibrated and tested according to the following programme:

a) Each pressure transducer was individually calibrated by fitting it to the standard hydraulic system used for pressure development in a soil triaxial test (see Figure 20). The calibration test was carried out three times for each transducer; each time the pressure was applied at  $0.5 \text{ Kgf/cm}^2 (\approx 50 \text{ kN/m}^2)$  increments up to a total pressure of  $6 \text{ Kgf/cm}^2$ .

b) Before fitting the pressure transducers, each of the cell bodies was individually tested and checked for leaks using a hydrostatic pressure of  $7 \text{ Kgf/cm}^2 (\approx 700 \text{ kN/m}^2)$  from the same system used above.

c) Each pressure cell was calibrated under hydrostatic pressure using a triaxial test cell which was modified to allow continuity of the pressure transducer cable from the cell to the recording equipment during the tests, as shown in Figures 19 and 20. The calibration test was performed five times for each cell at two different degrees of temperature. The pressure was applied at  $0.5 \text{ Kgf/cm}^2 (\approx 50 \text{ kN/m}^2)$  increments up to a total pressure of  $5.0 \text{ Kgf/cm}^2 (\approx 500.0 \text{ kN/m}^2)$ . Figures 21 to 26 inclusive show the calibration charts for the pressure cells used in the first experiment, the results of the calibration tests being listed in Table 1.

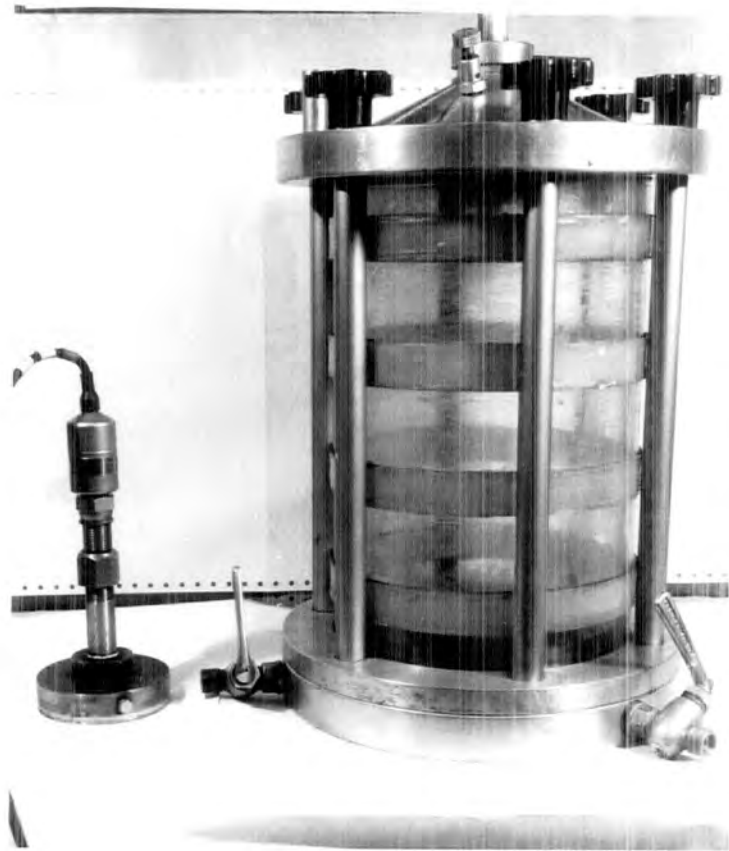


Figure 19 the cell used in hydraulic calibration

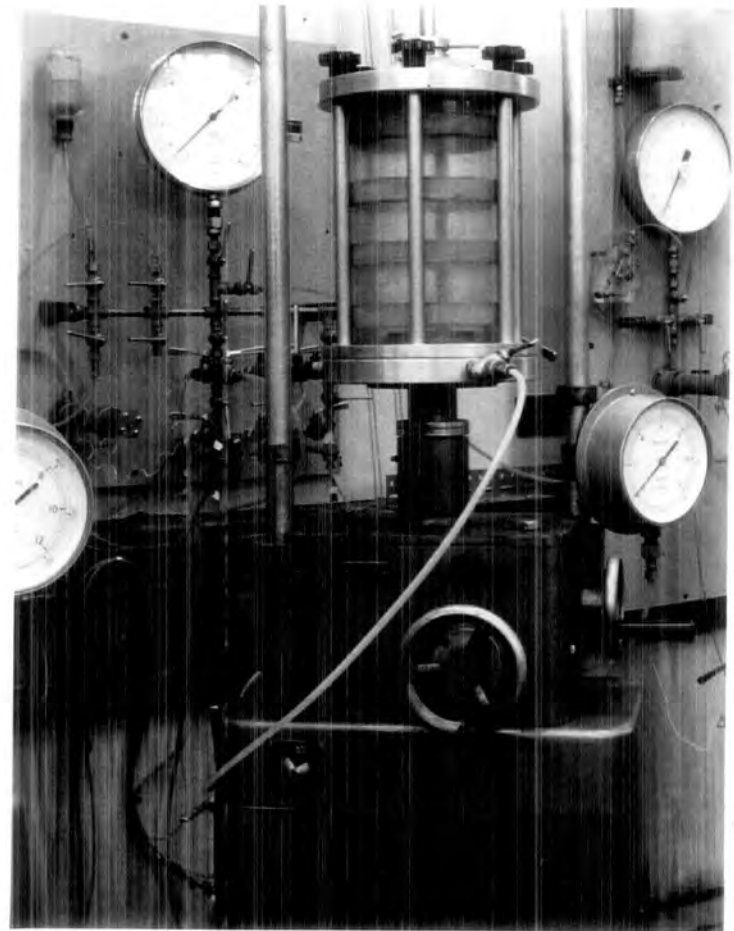


Figure 20 The pressure system used in calibration



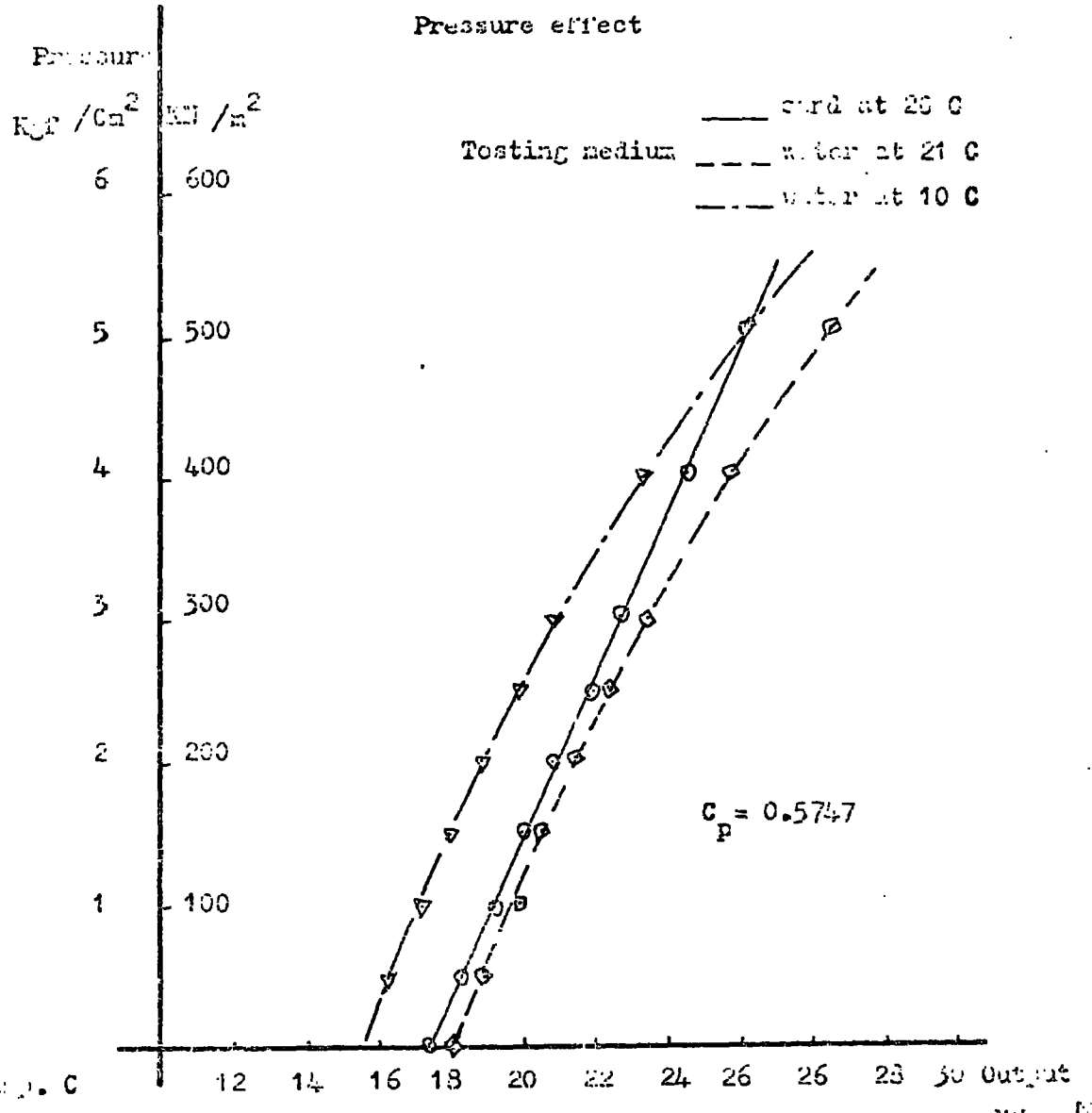
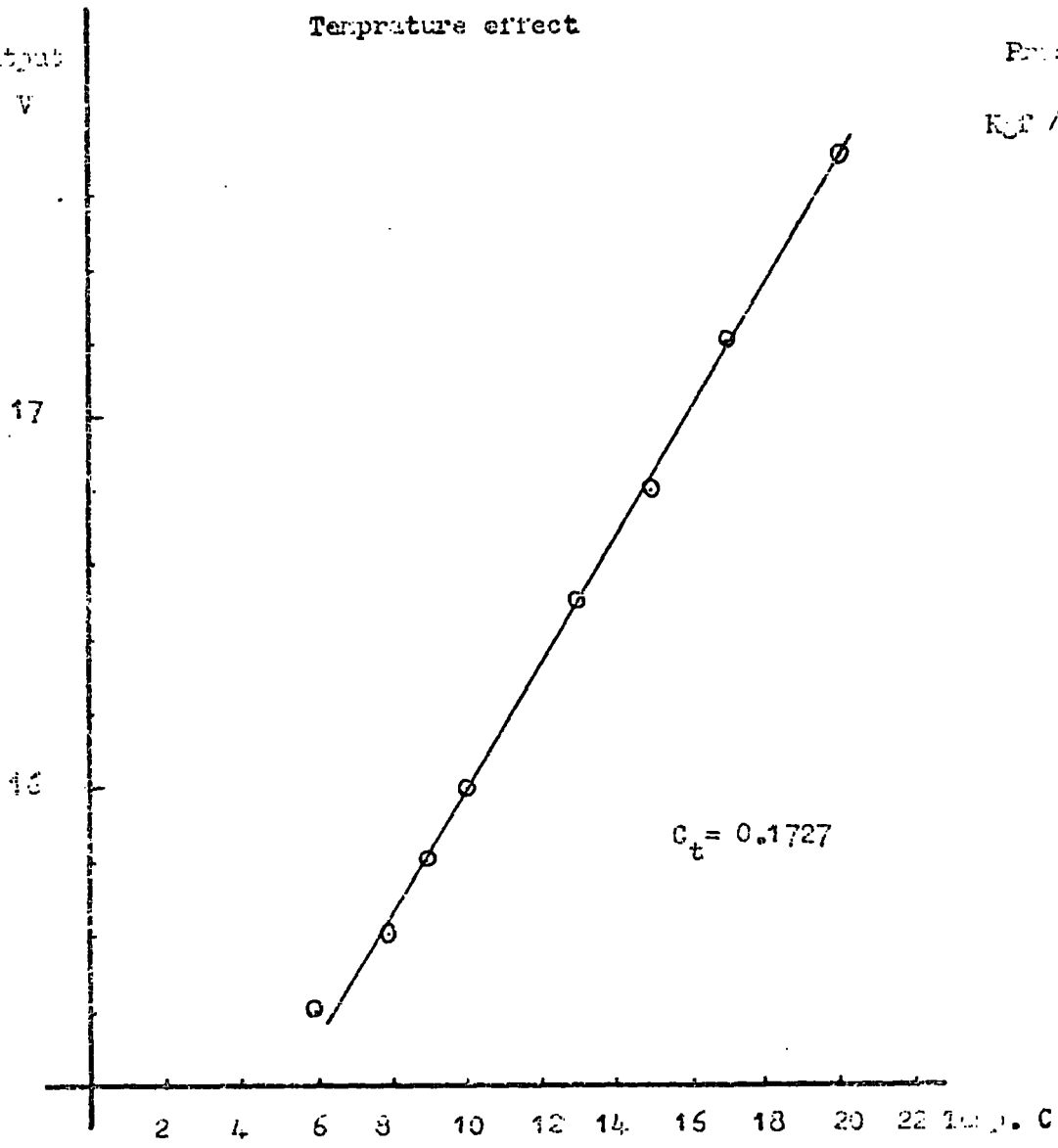


Figure 21 Calibration charts for pressure cell No. 1

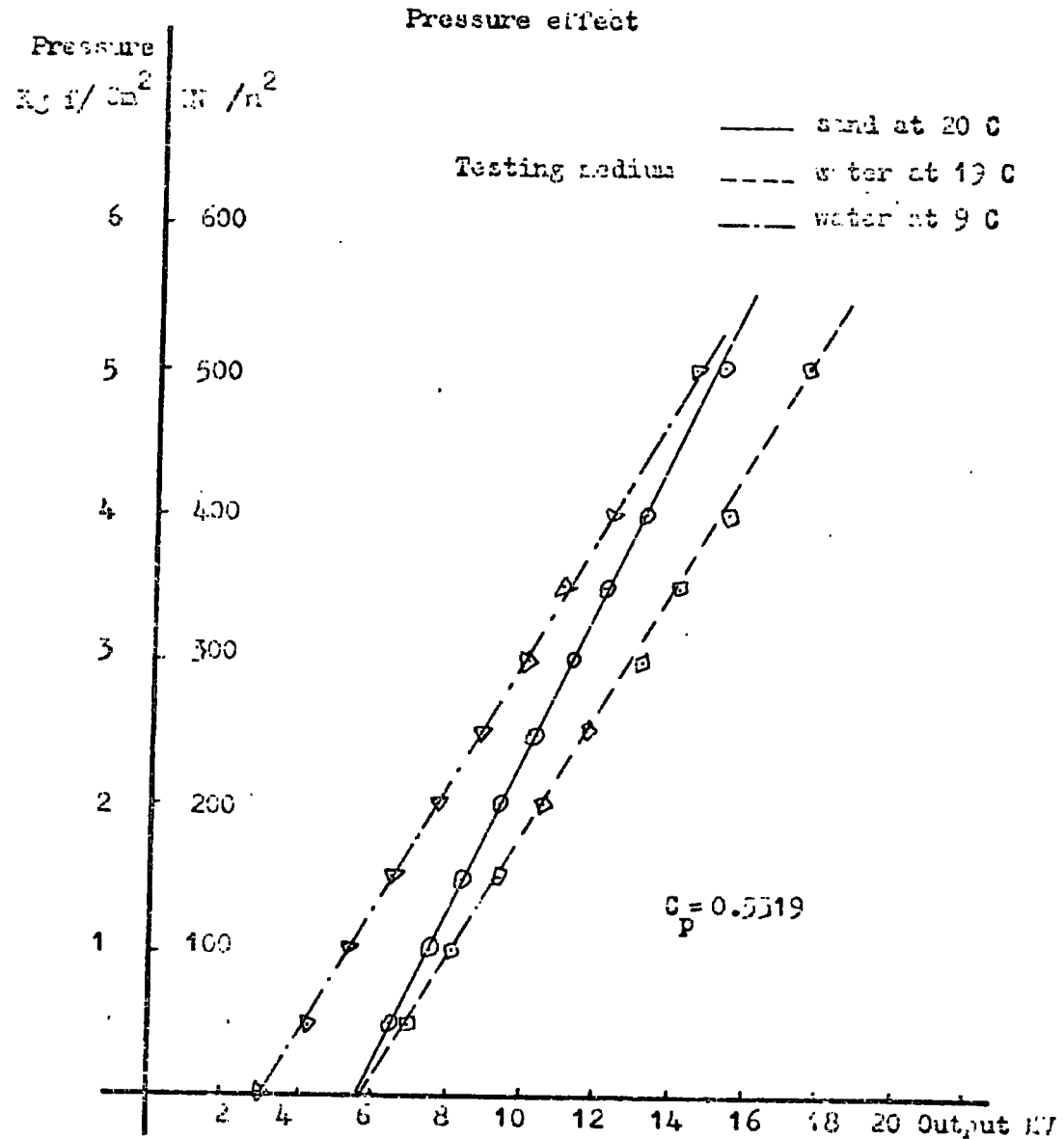
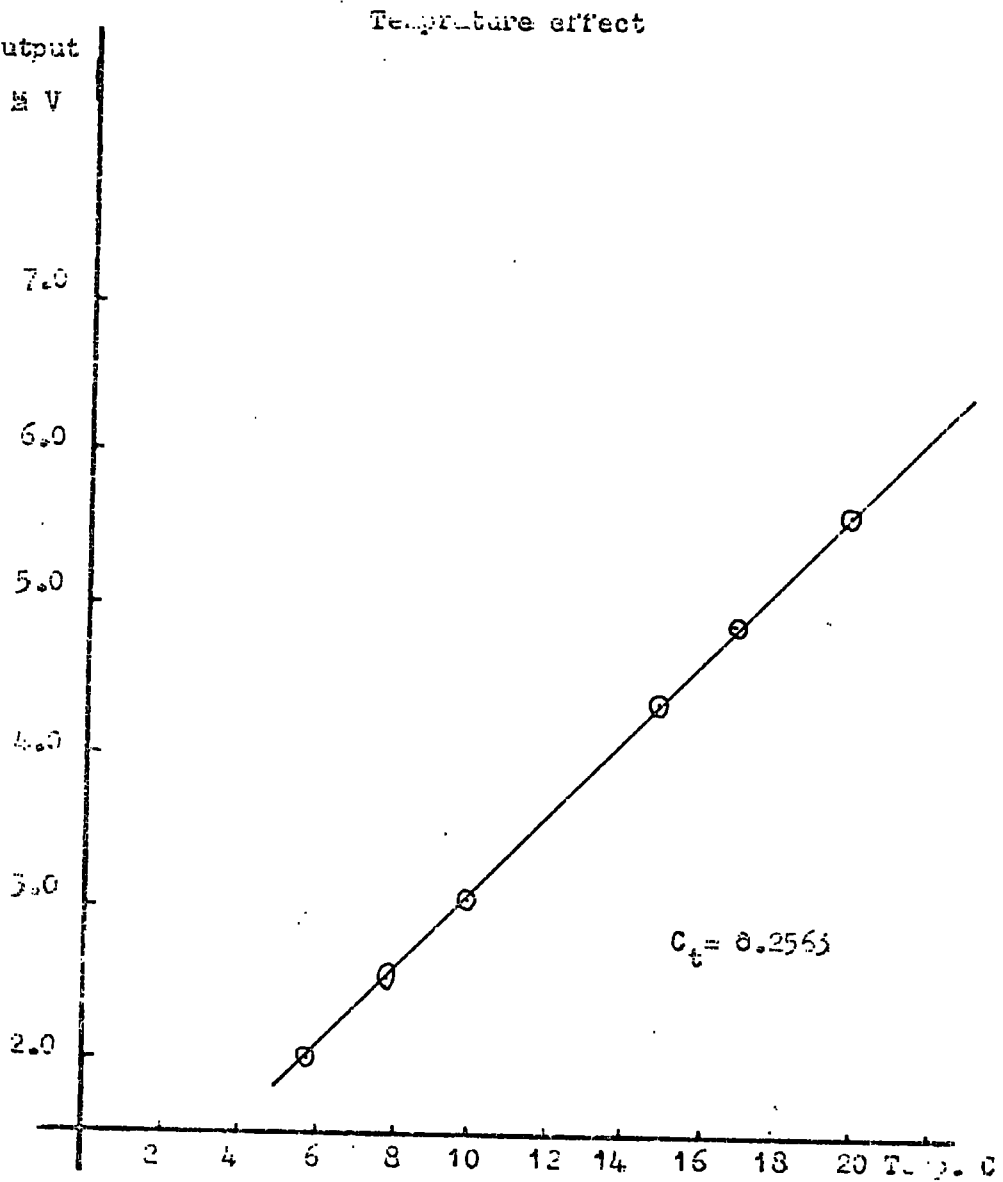


Figure 22 Calibration charts for pressure Cell No. 2

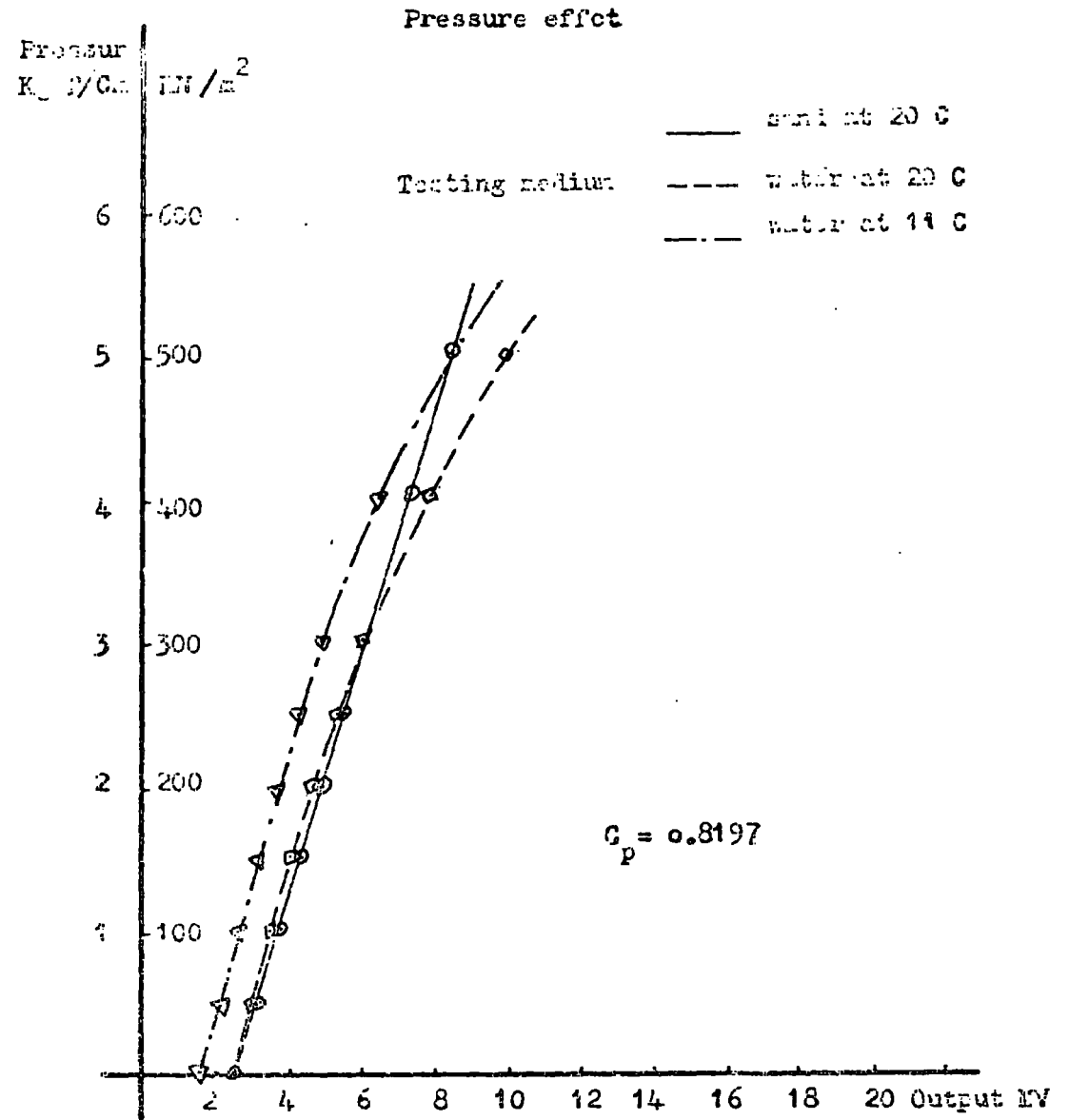
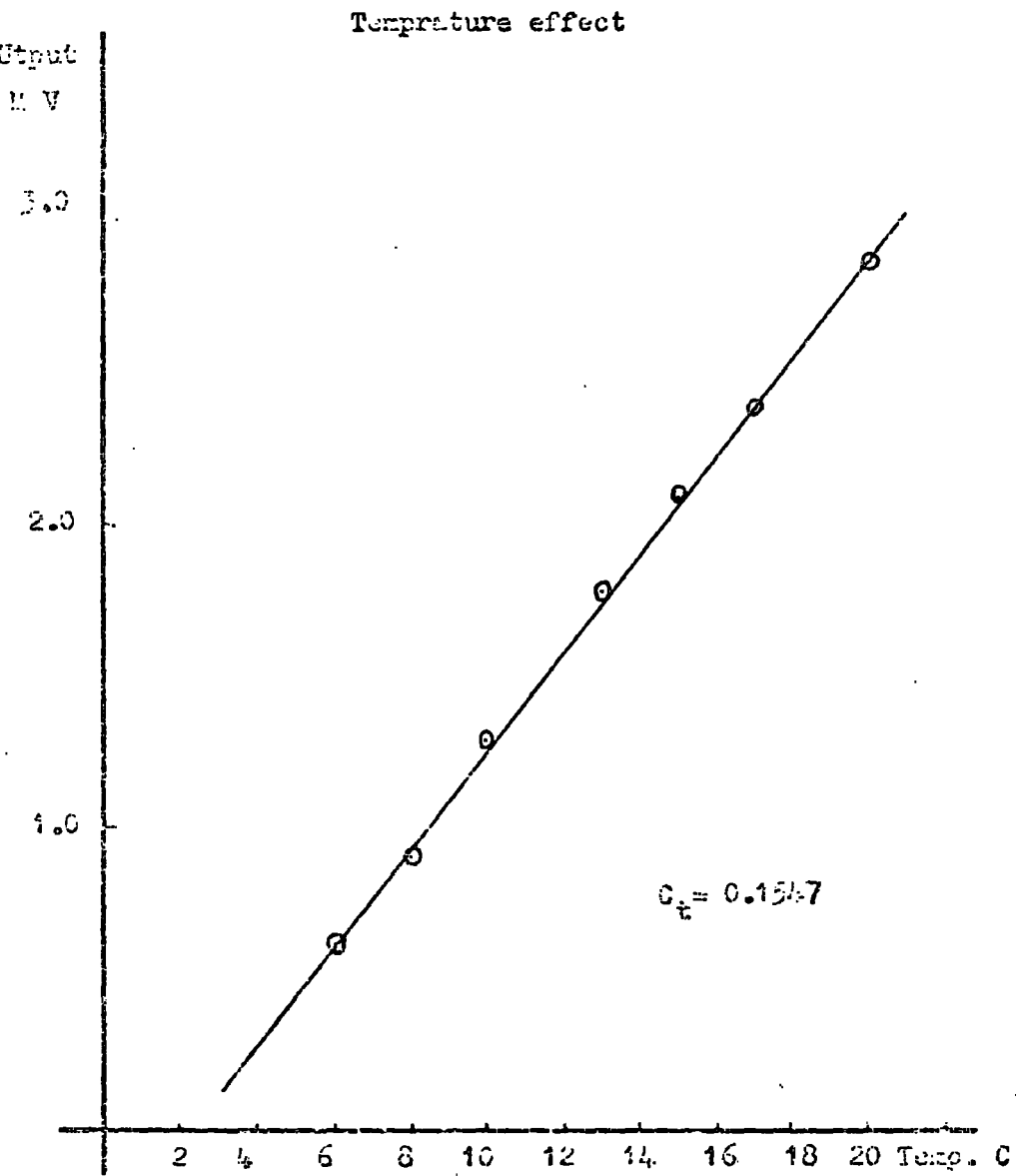
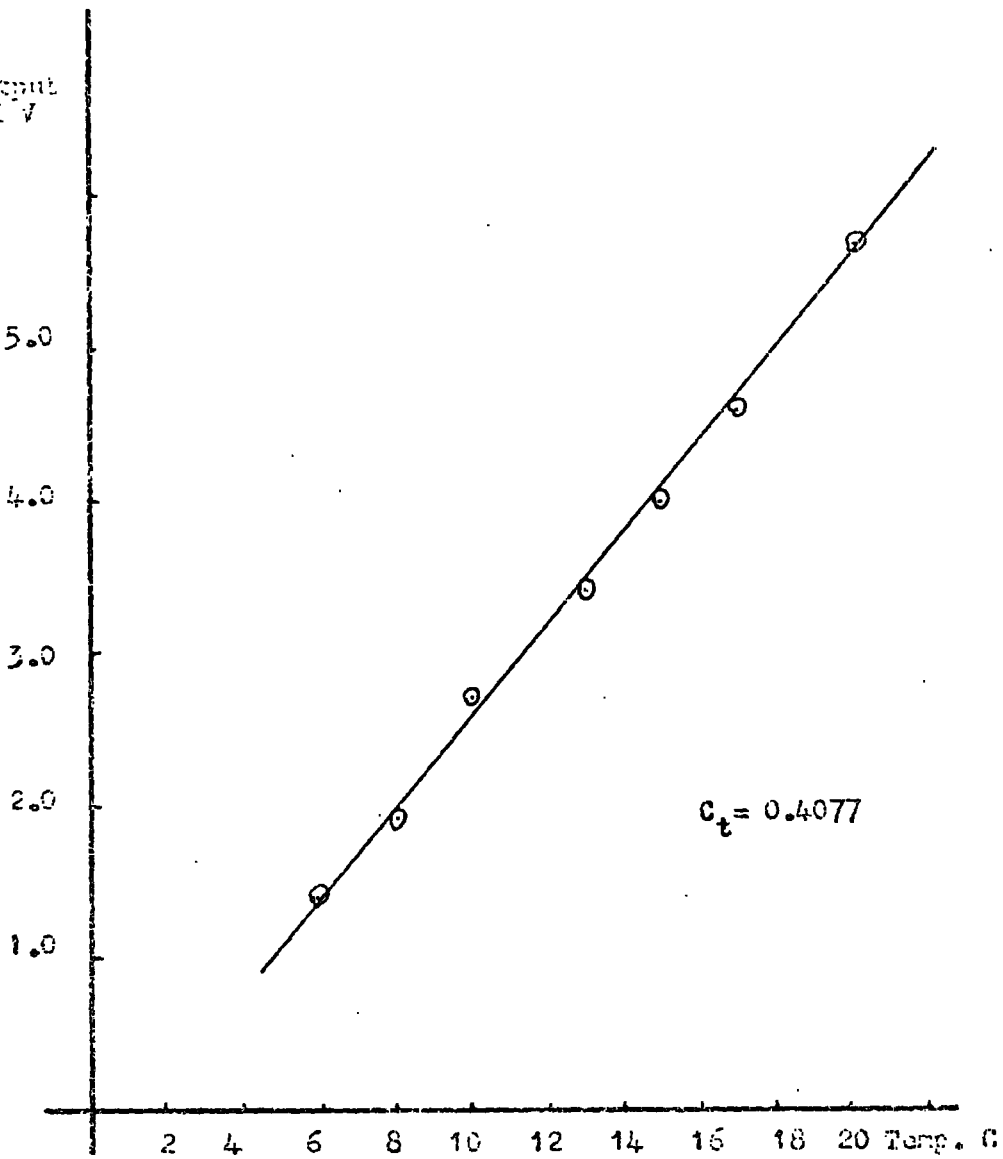


Figure 23 Calibration charts for pressure cell No. 3

Temperature effect



Pressure effect

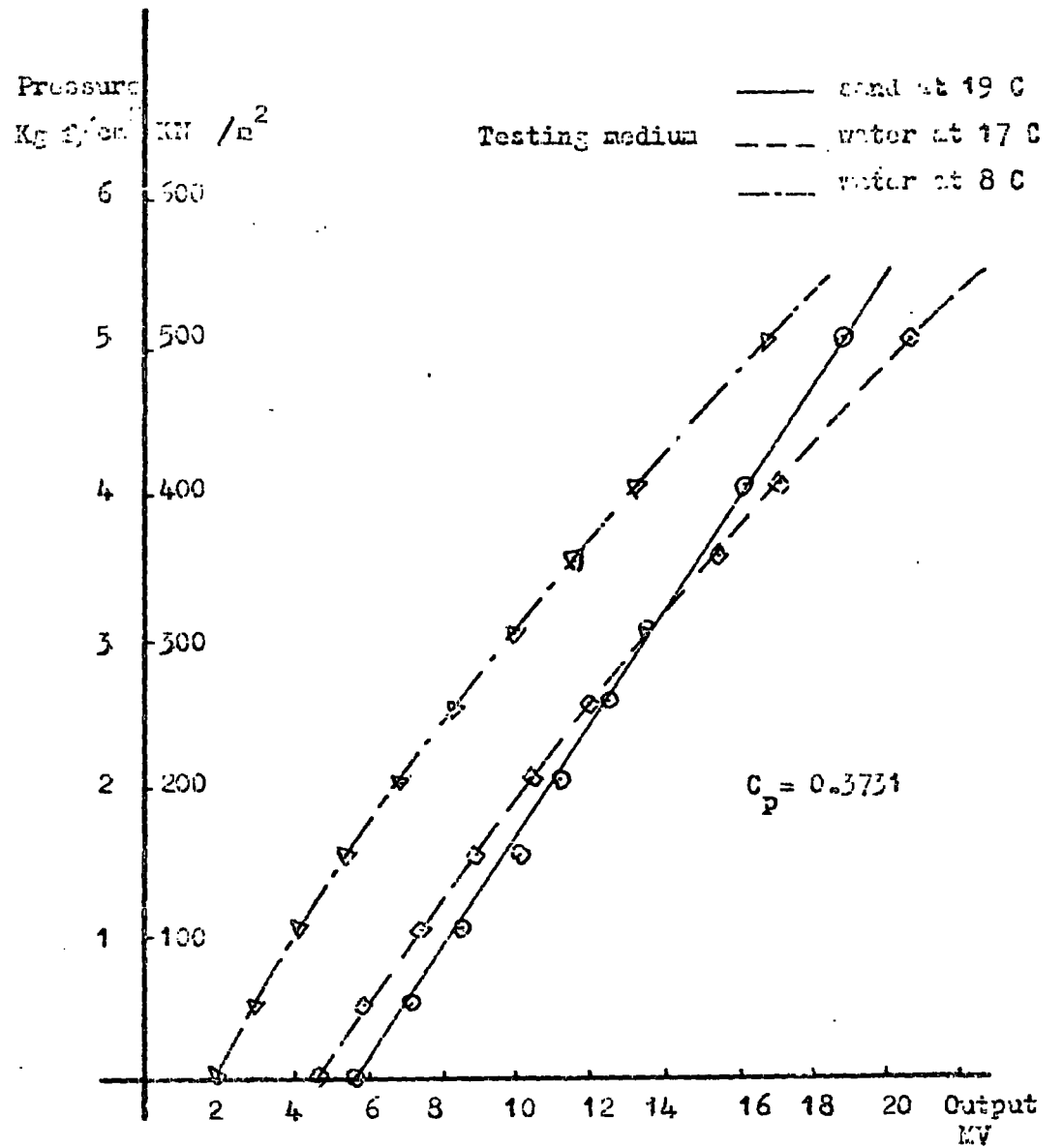
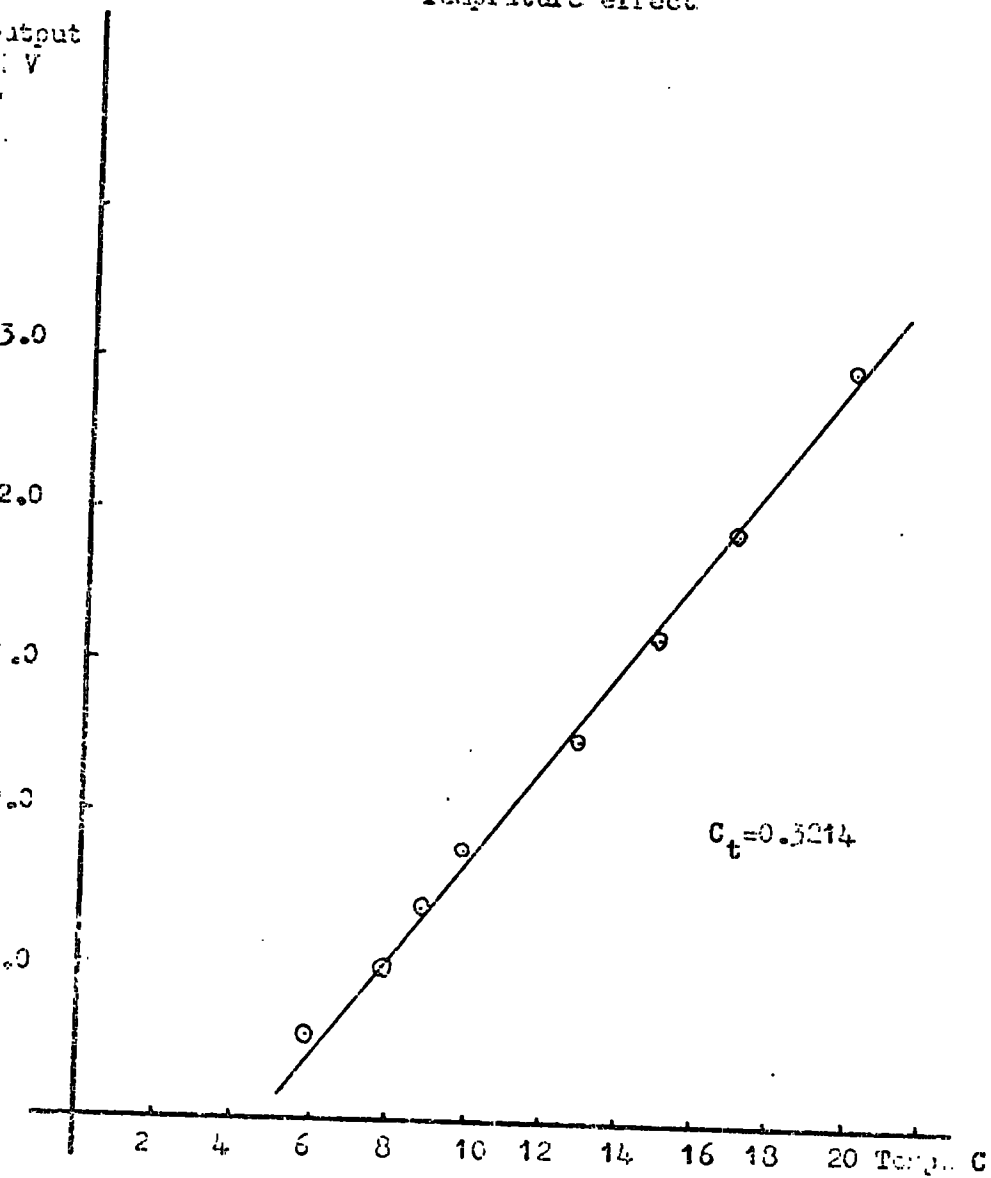


Figure 24 Calibration charts for pressure cell No. 4

Temperature effect



Pressure effect

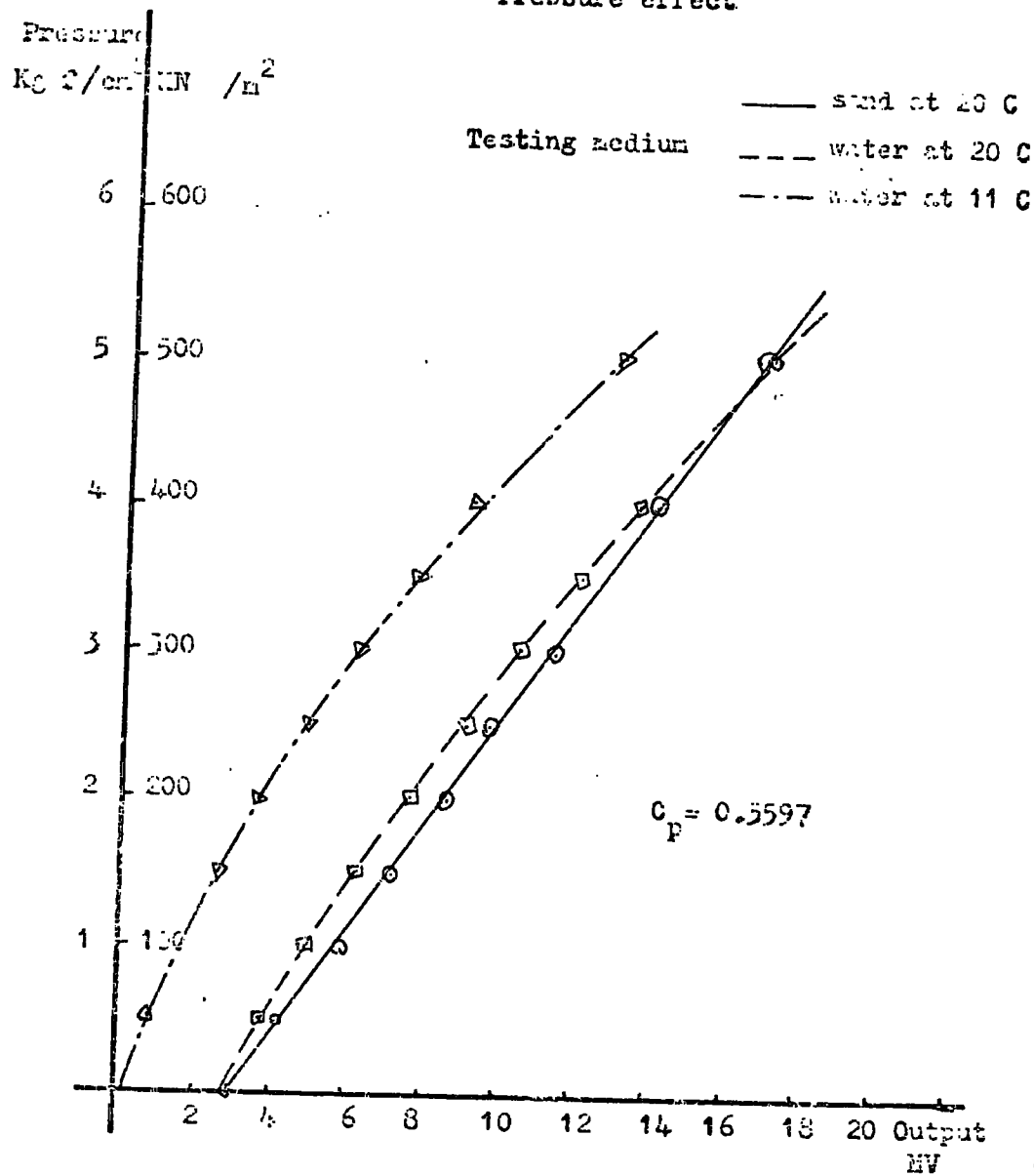
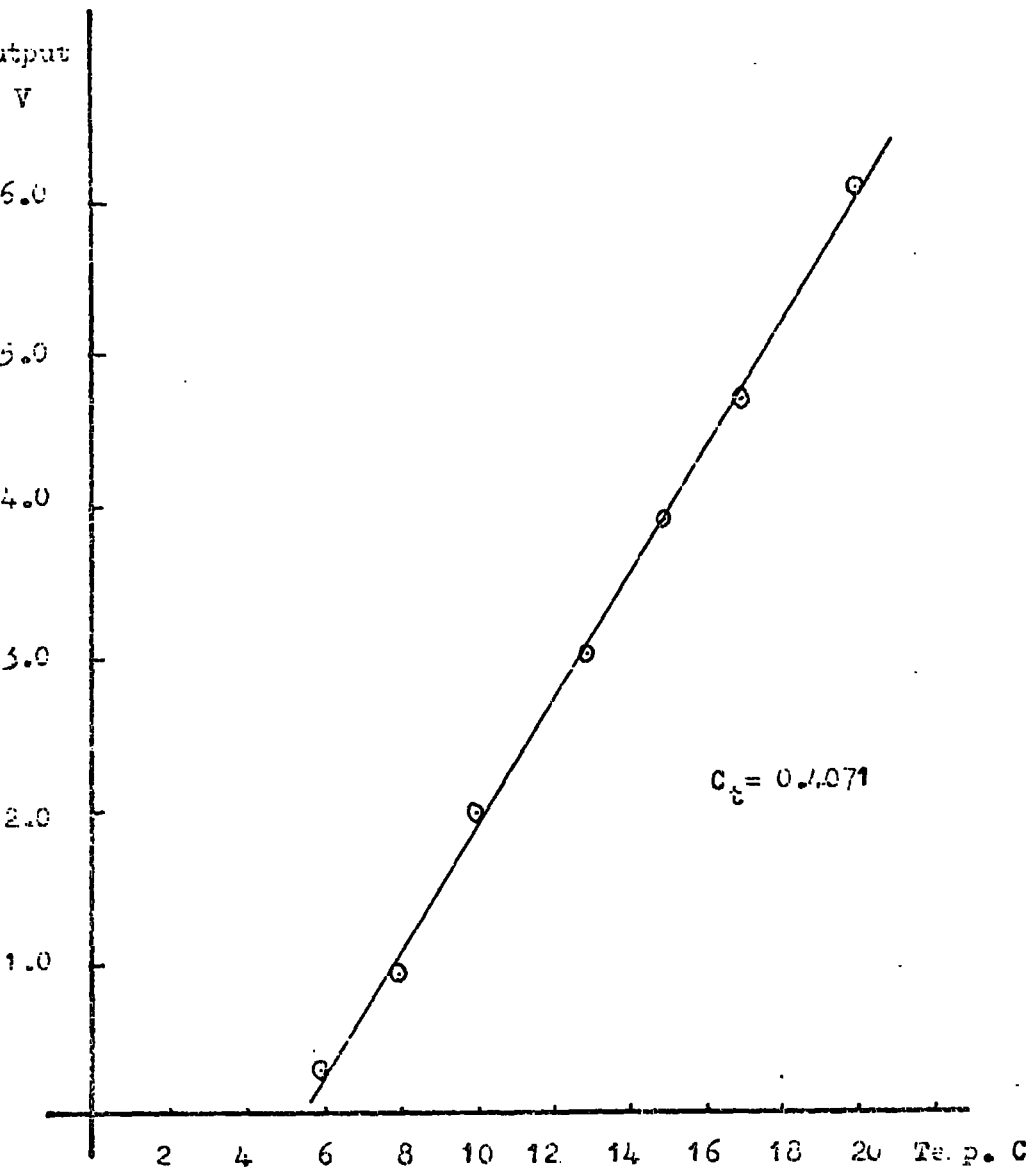


Figure 25 Calibration charts for pressure cell No. 5

Temperature effect



Pressure effect

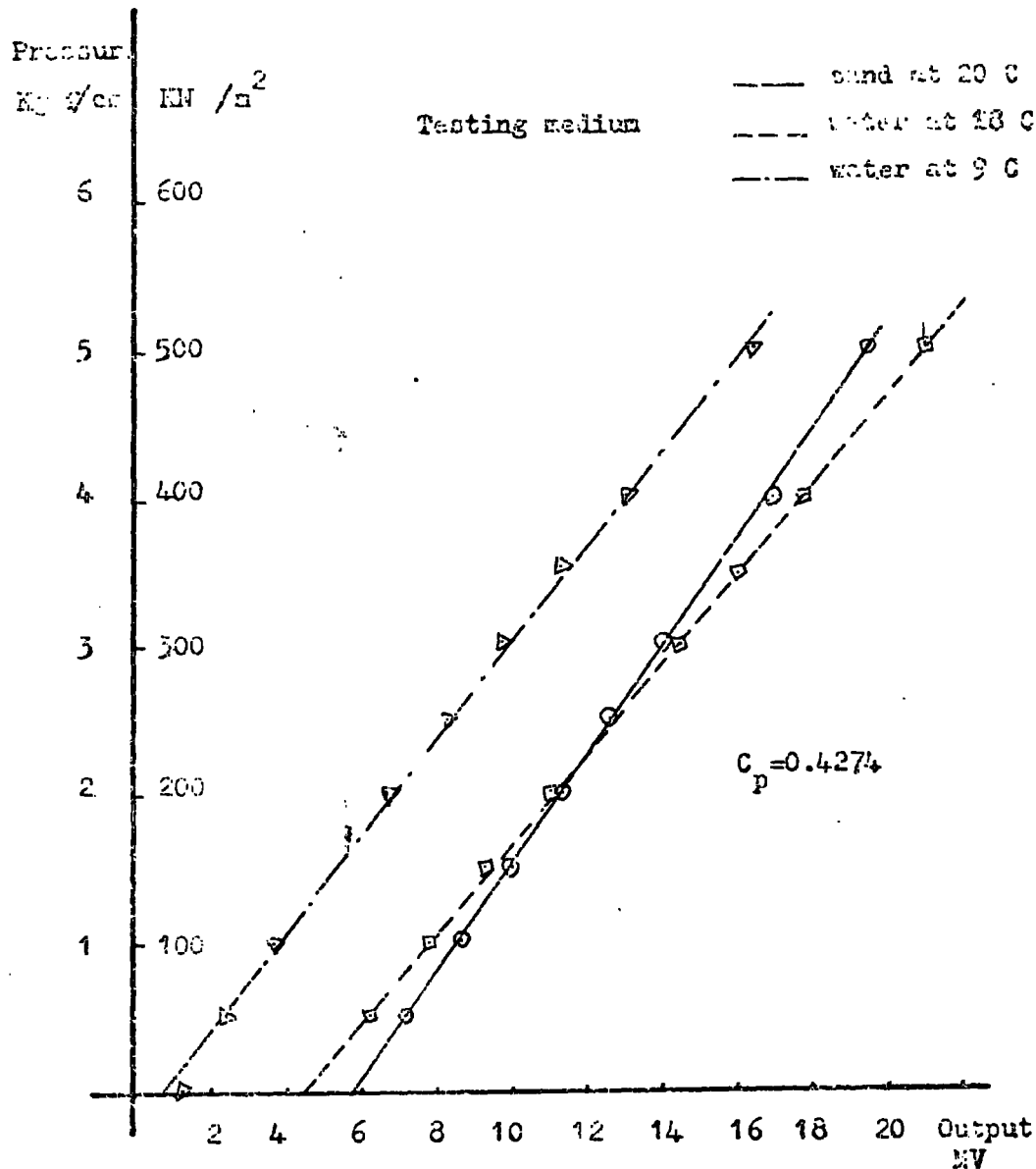


Figure 26 Calibration charts for pressure cell No. 6

CELL kg/cm <sup>2</sup> Pressure	No. 1		No. 2		No. 3		No. 4		No. 5		No. 6	
	23 C	10 C	19 C	9 C	20 C	11 C	17 C	8 C	20 C	12 C	20 C	9 C
0.0	18.3	15.9	5.4	3.0	2.7	1.5	4.7	1.9	2.9	0.2	5.2	1.5
0.5	18.9	16.4	6.9	4.1	3.2	2.2	5.9	2.9	3.8	0.8	6.4	2.5
1.0	19.7	17.3	8.2	5.3	3.7	2.8	7.4	4.1	4.9	1.5	7.9	3.8
1.5	20.6	18.1	9.4	6.5	4.3	3.3	9.0	5.5	6.3	2.6	9.6	5.3
2.0	21.6	19.0	10.6	7.8	4.8	3.8	10.6	7.0	7.7	3.5	11.2	6.8
2.5	22.7	20.1	11.8	9.0	5.4	4.4	12.2	10.0	9.2	5.0	12.9	8.4
3.0	23.7	21.0	13.0	10.2	6.1	5.0	13.8	11.8	10.6	6.2	14.5	9.9
4.0	26.1	23.5	15.3	12.6	8.0	6.5	17.2	13.5	13.7	9.2	17.9	13.2
5.0	28.3	25.1	17.6	15.1	10.1	8.4	20.7	16.9	16.9	12.3	21.2	16.6

Table 1 Results of calibration tests for the pressure cells using hydraulic pressure.  
( first experiment )

d) Each of the pressure cells was then calibrated using dry sieved sand as a testing medium. Figure 27 shows the particle size distribution of the sand used. The calibration tank was designed and constructed in the form shown in Figures 28 and 30. The tank consists of a steel tube 49 cm in diameter and 61 cm high, a circular supporting plate welded to the tank body at a distance of 30 cm from the base, and a circular loading plate. During the test, the pressure cell is placed inside the upper part of the calibration tank facing the testing medium. The rest of the cell body remains in the lower part of the calibration tank through a 2 inch (50 mm) hole in the supporting plate. The hydraulic testing machine used in these tests is shown in Figure 29.

Tests were performed to determine the effect of thickness of the sand cover, when the sand and the cell were compressed, upon the output of the pressure cell. Figures 31 and 32 show this effect. It is implied that for a sand cover equal to, or greater than 25 cm, there is no effect of sand cover changes on the output of the cell. Accordingly, a sand cover of 27.5 cm was used for all the calibration tests in which sand was used as a testing medium.

The calibration test using 27.5 cm sand cover was performed five times for each cell, the pressure being applied at  $0.5 \text{ Kg/cm}^2$  increments up to a total pressure of  $5.0 \text{ Kg/cm}^2$  ( $\approx 500 \text{ kN/m}^2$ ). Figures 21 to 26 represent the calibration charts for the pressure cells used in the first experiment. Values are expressed by means of five tests. From these charts the cell pressure coefficients 'Cp' - 'Cp' is the indicated pressure per unit output 'mv' - were calculated. The results of the calibration tests are listed in Table 2.



PARTICLE SIZE DISTRIBUTION

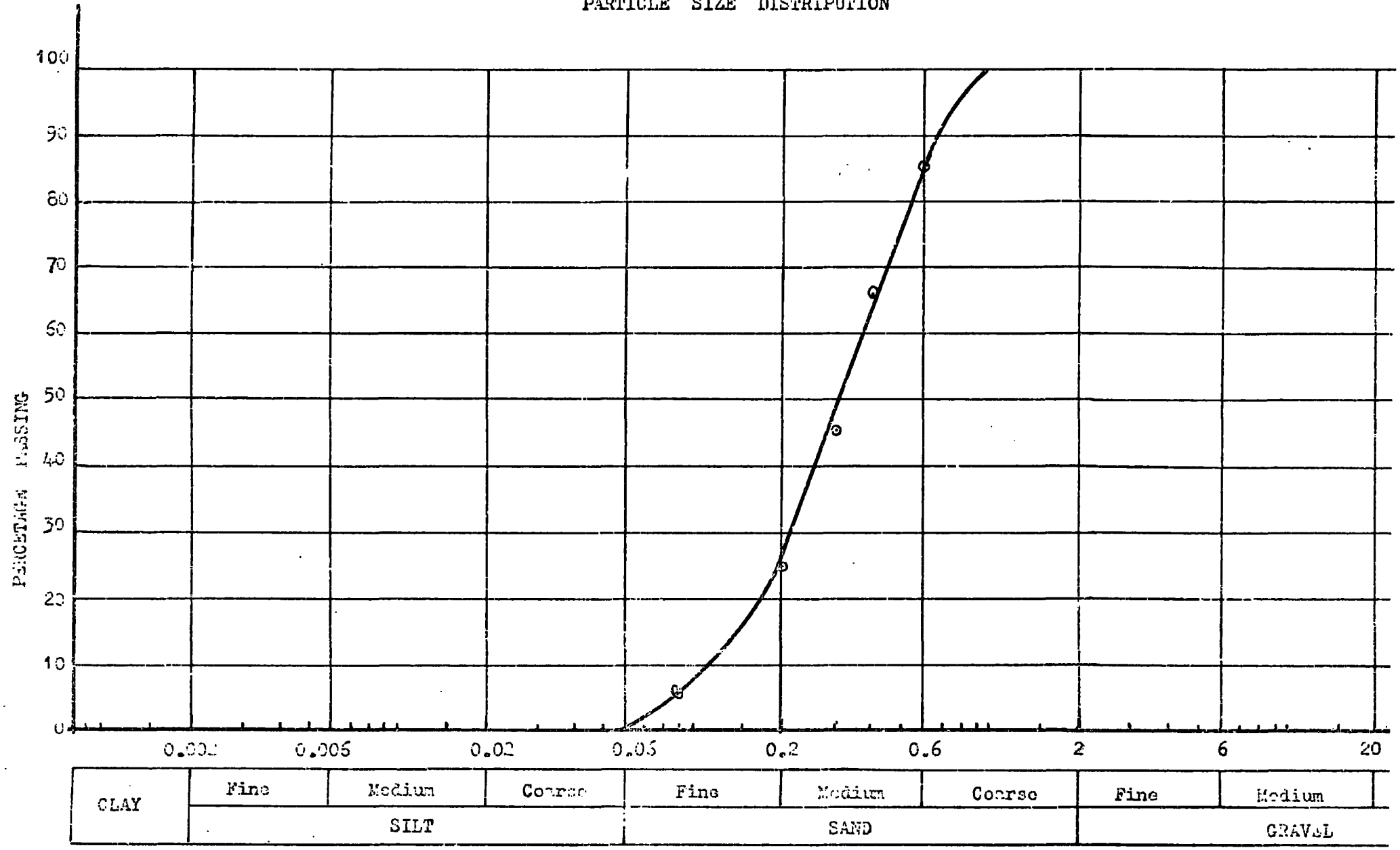


Figure 27 Particle size distribution of the sand used in calibration

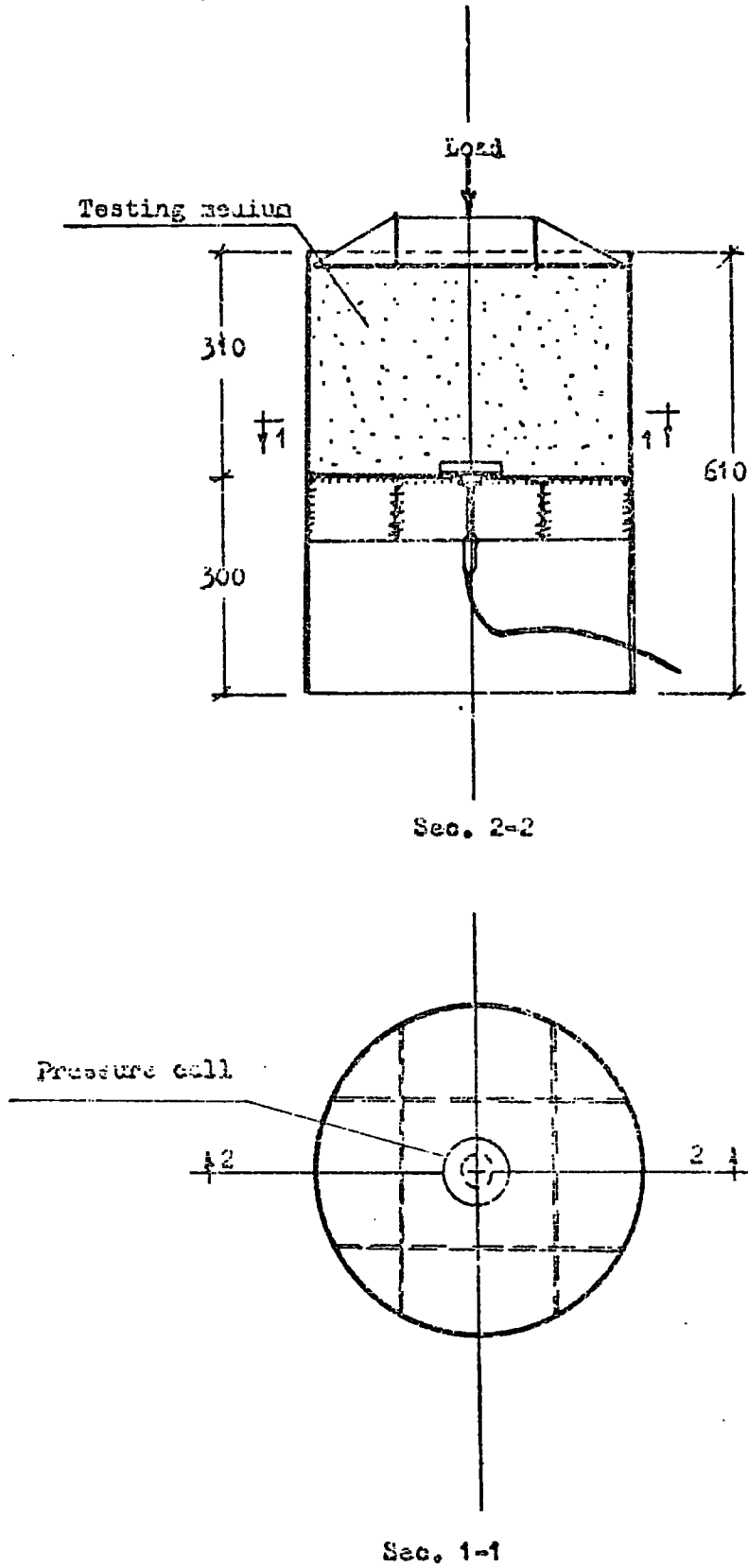


Figure 28 Sections through the testing tank

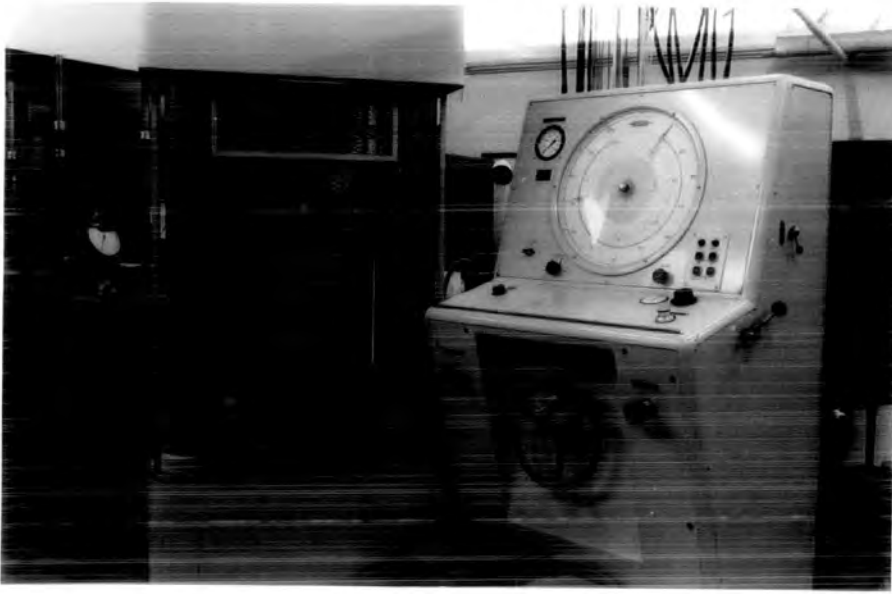


Figure 29 The machine used in calibration



Figure 30 The calibration tank

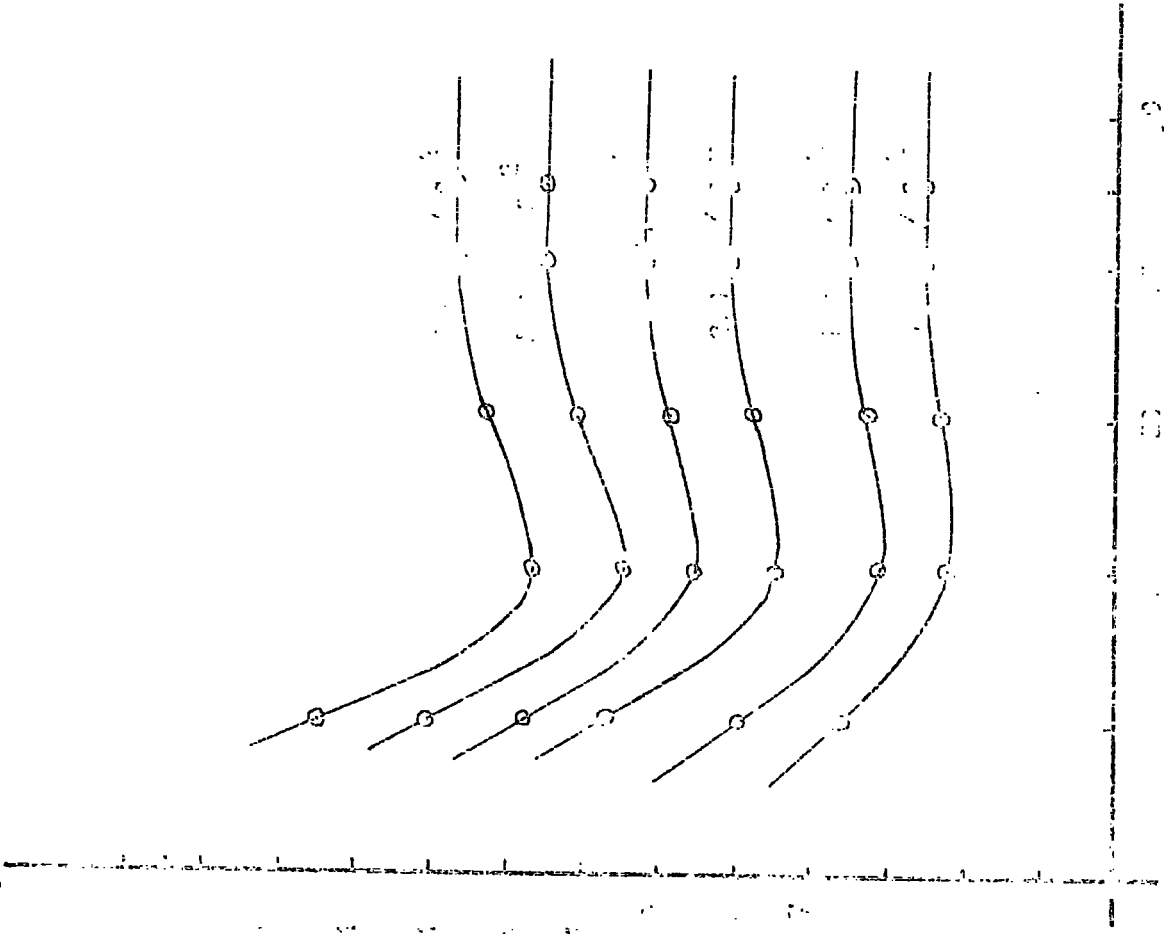
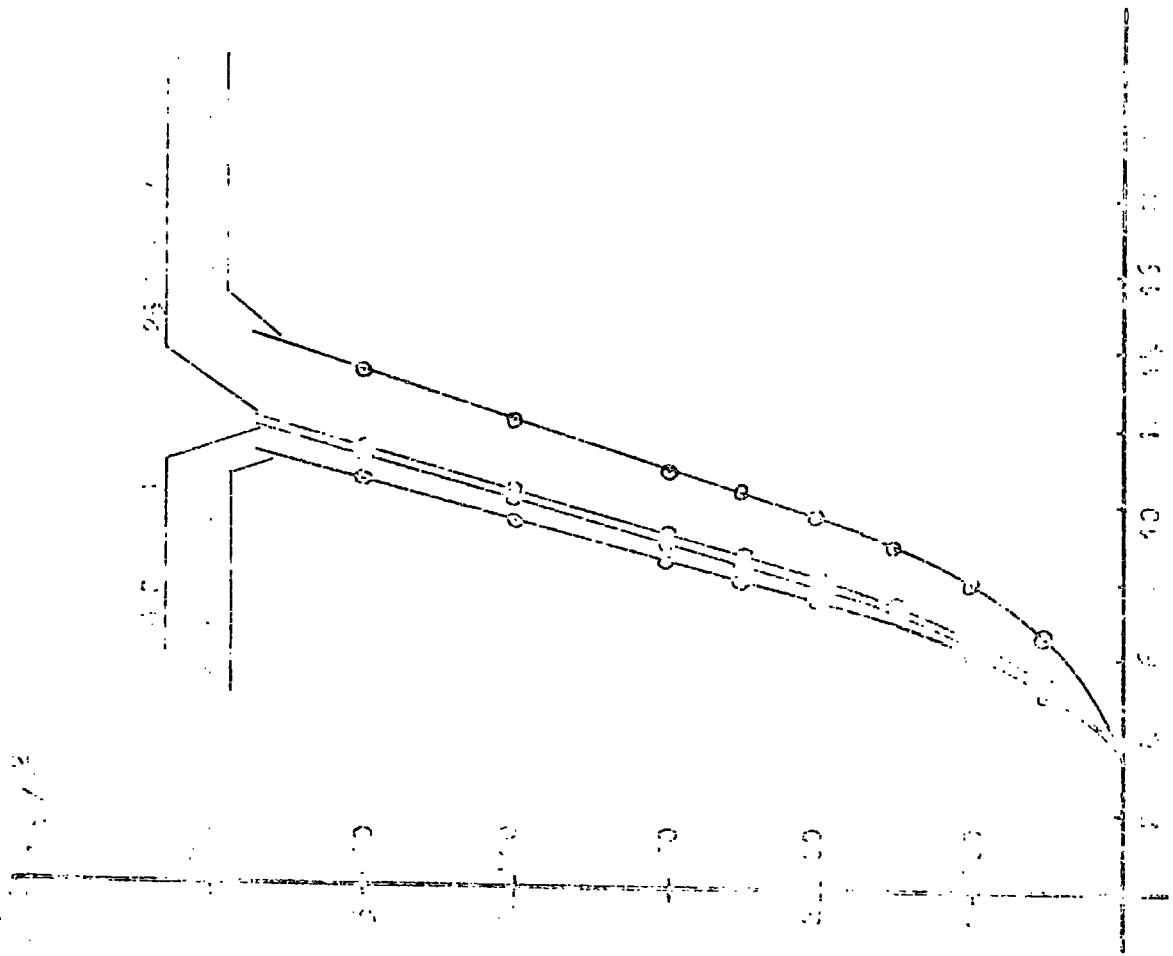


Figure 1. The curves are calculated for the case of  $\alpha = 0.5$  and  $\beta = 0.5$ .

Figure 2. The curves are calculated for the case of  $\alpha = 0.5$  and  $\beta = 0.5$ .

CELL Kg/cm <sup>2</sup> PRESSURE	No. 1 at 20 C°	No. 2 At 20 C°	No. 3 at 20 C°	No. 4 at 19 C°	No. 5 at 20 C°	No. 6 at 20 C°
0.0	17.7	5.6	2.7	5.4	2.9	5.9
0.5	18.6	6.4	3.5	7.4	4.5	7.0
1.0	19.3	7.4	4.1	8.5	5.9	8.2
1.5	20.2	8.5	4.6	9.8	7.4	9.5
2.0	21.2	9.4	5.1	11.4	9.0	10.7
2.5	21.9	10.4	5.6	12.6	10.4	11.8
3.0	22.8	11.4	6.0	13.7	11.4	12.8
4.0	24.6	13.3	7.3	16.2	14.0	15.3
5.0	26.3	15.0	8.6	18.9	16.8	17.6

Table 2 Results of calibration tests for the pressure cells using dry sand as a testing medium

CELL C° TEMP.	No. 1	No. 2	No. 3	No. 4	No. 5	No. 6
6	15.4	2.0	0.6	1.4	-1.4	0.3
8	15.6	2.5	0.9	1.9	-1.0	0.9
10	16.0	3.1	1.3	2.7	-0.2	2.0
13	16.5	3.8	1.8	3.4	0.3	3.0
15	16.8	4.4	2.1	4.0	1.2	3.9
17	17.2	4.9	2.4	4.6	1.9	4.7
20	17.7	5.6	2.7	5.7	2.9	6.0

Table 3 Results of temperature calibration tests (first experiment)

e) Tests were performed to evaluate the effect of the temperature changes on the cell output under no load conditions. Tests were performed three times for each cell using a variable temperature water bath. The results of these tests are tabulated in Table 3. The calibration charts are represented by Figures 21 to 26 from which the cell temperature coefficients ' $C_t$ ' - ' $C_t$ ' is defined as the change in the pressure cell output per one degree change in temperature - were calculated.

Each of the pressure cells used in the second experiment were calibrated and tested according to the following programme:

i) The pressure transducer and the cell bodies were tested and calibrated according to the same procedure as before for the cells used in the first experiment.

ii) Each of the pressure cells was calibrated using dry sieved sand as a testing medium, following the same procedure mentioned before for the cells used in the first experiment. The results of the calibration tests are tabulated in Table 4. Figures 33 to 38 show the calibration charts from which the cell pressure coefficients ( $C_p$ ) were calculated.

iii) Each of the pressure cells was calibrated using a cylindrical clay sample, 20 cm in diameter and 15 cm high, as a contact medium to the cell-sensing diaphragm. The rest of the testing tank volume was filled with dry sieved sand. These test results were identical to those obtained from the calibration test using sand only. Figure 39 shows a section in the calibration tank and indicates the position of the clay cylinder.

iv) Tests were performed in order to evaluate the effect of temperature changes. These tests followed the same procedure as mentioned before for the cells used in the first experiment. Figures 33 to 38 show the calibration charts from which the cell temperature coefficients ( $C_t$ ) were calculated.

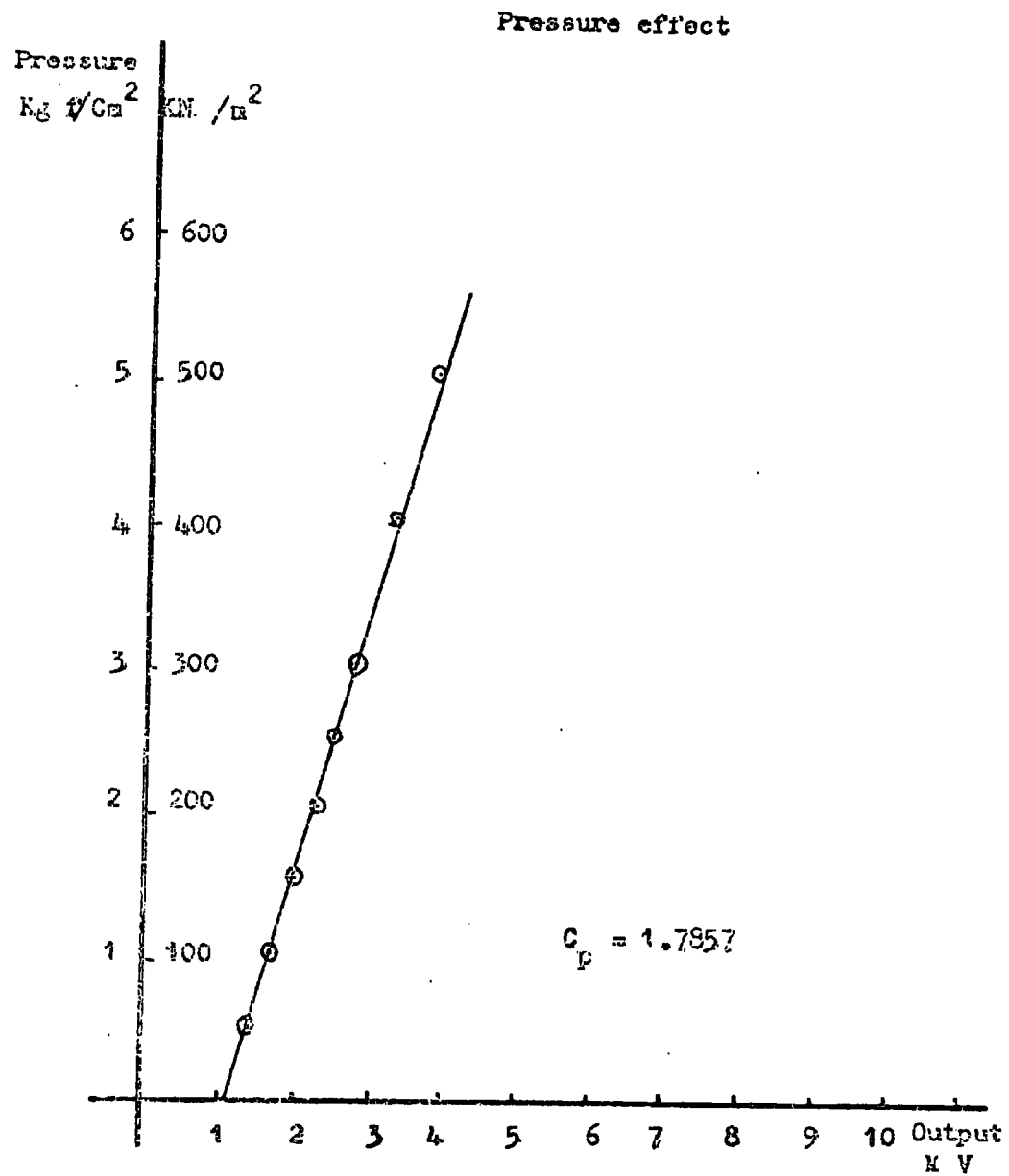
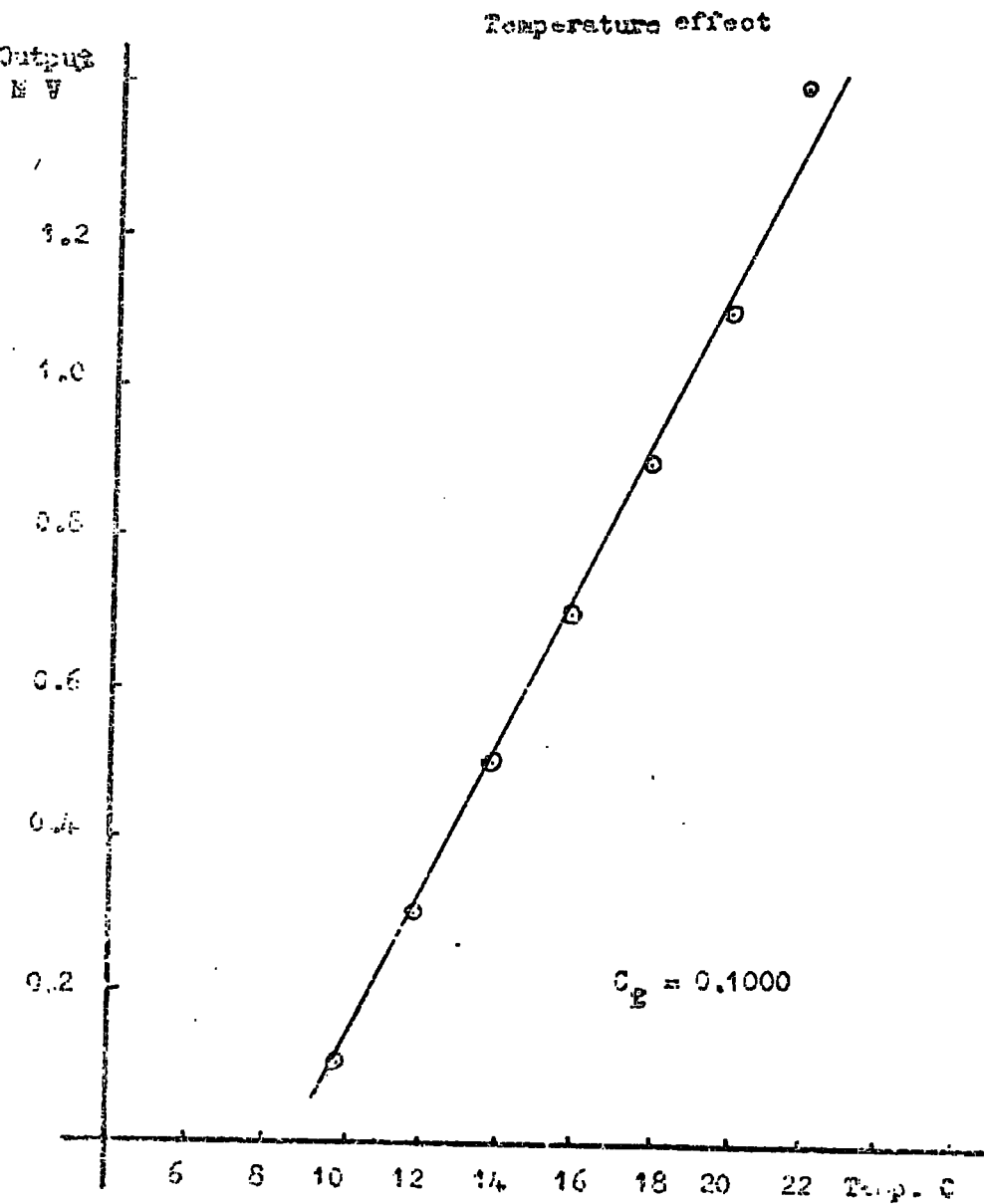
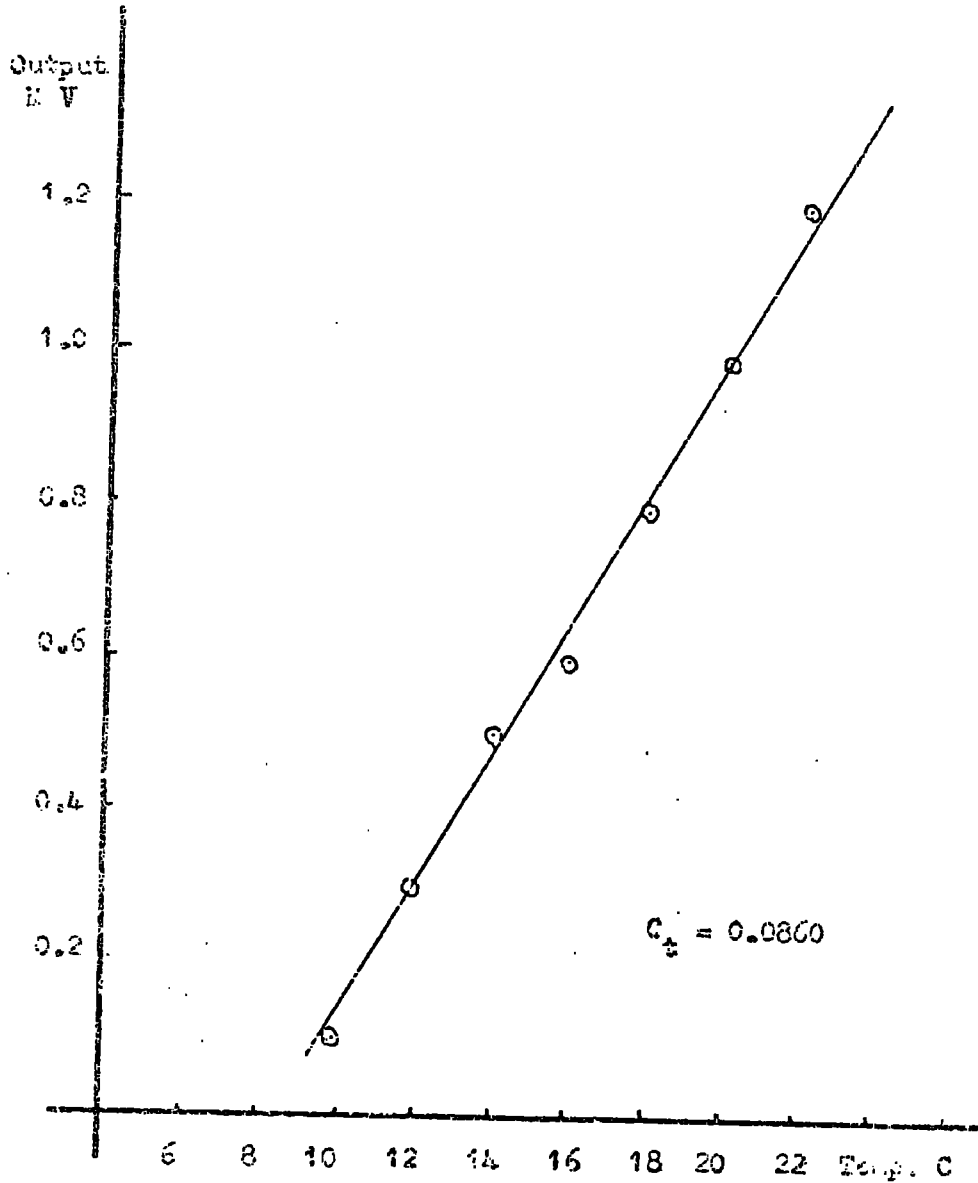


Figure 55 Calibration charts for pressure Cell No. 1

Temperature effect



Pressure effect

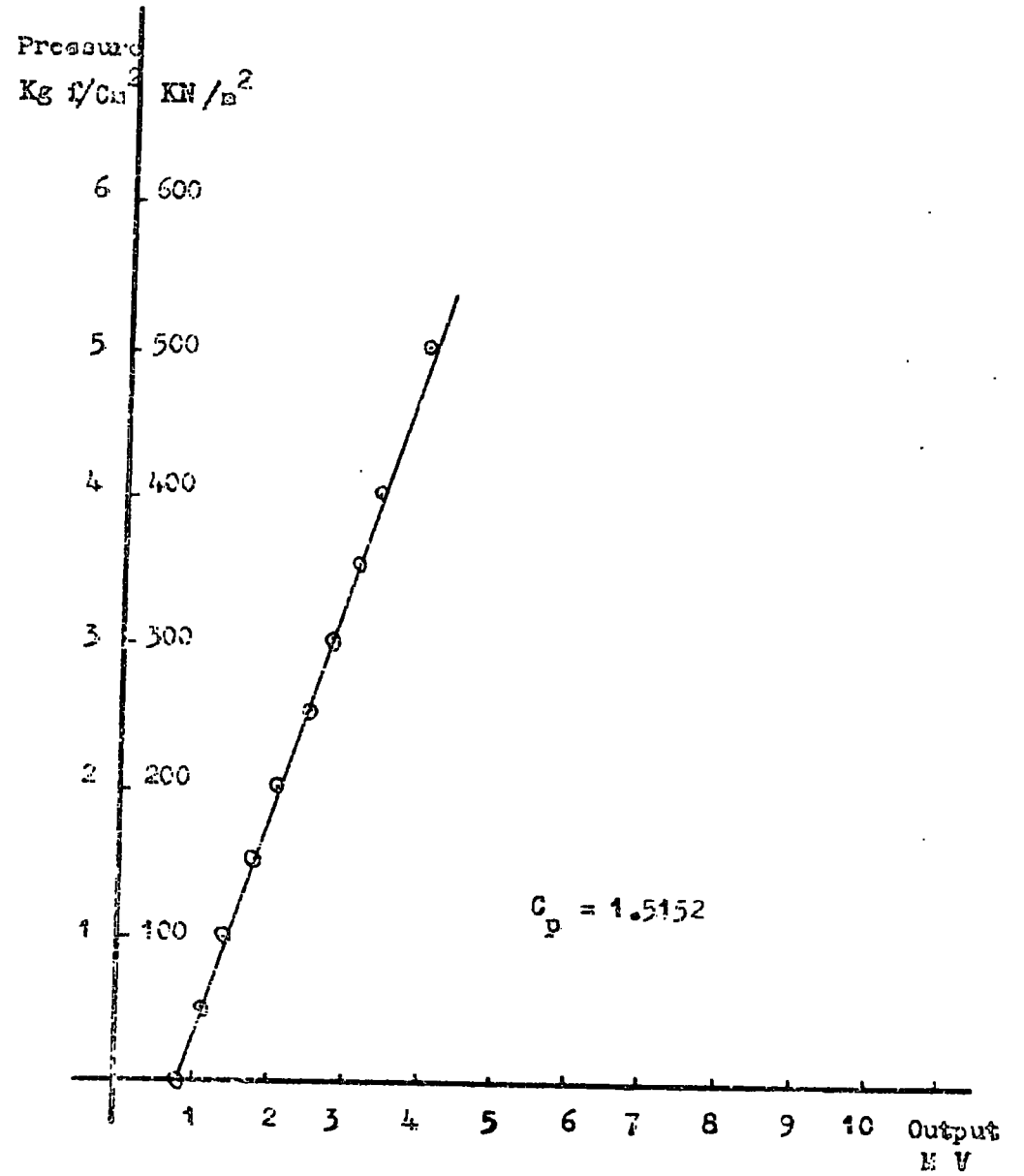
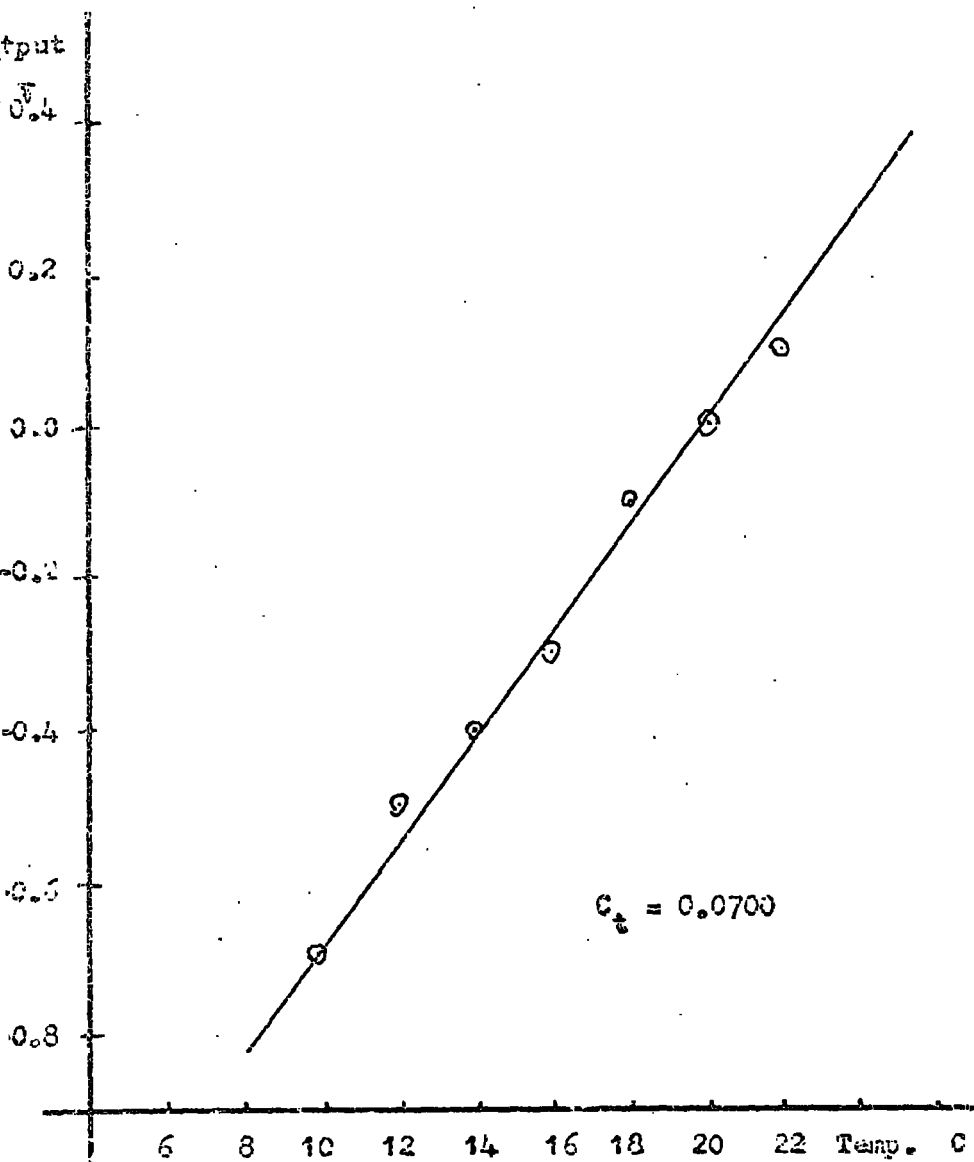


Figure 34 Calibration charts for pressure Cell No. 2



Temperature effect



Pressure effect

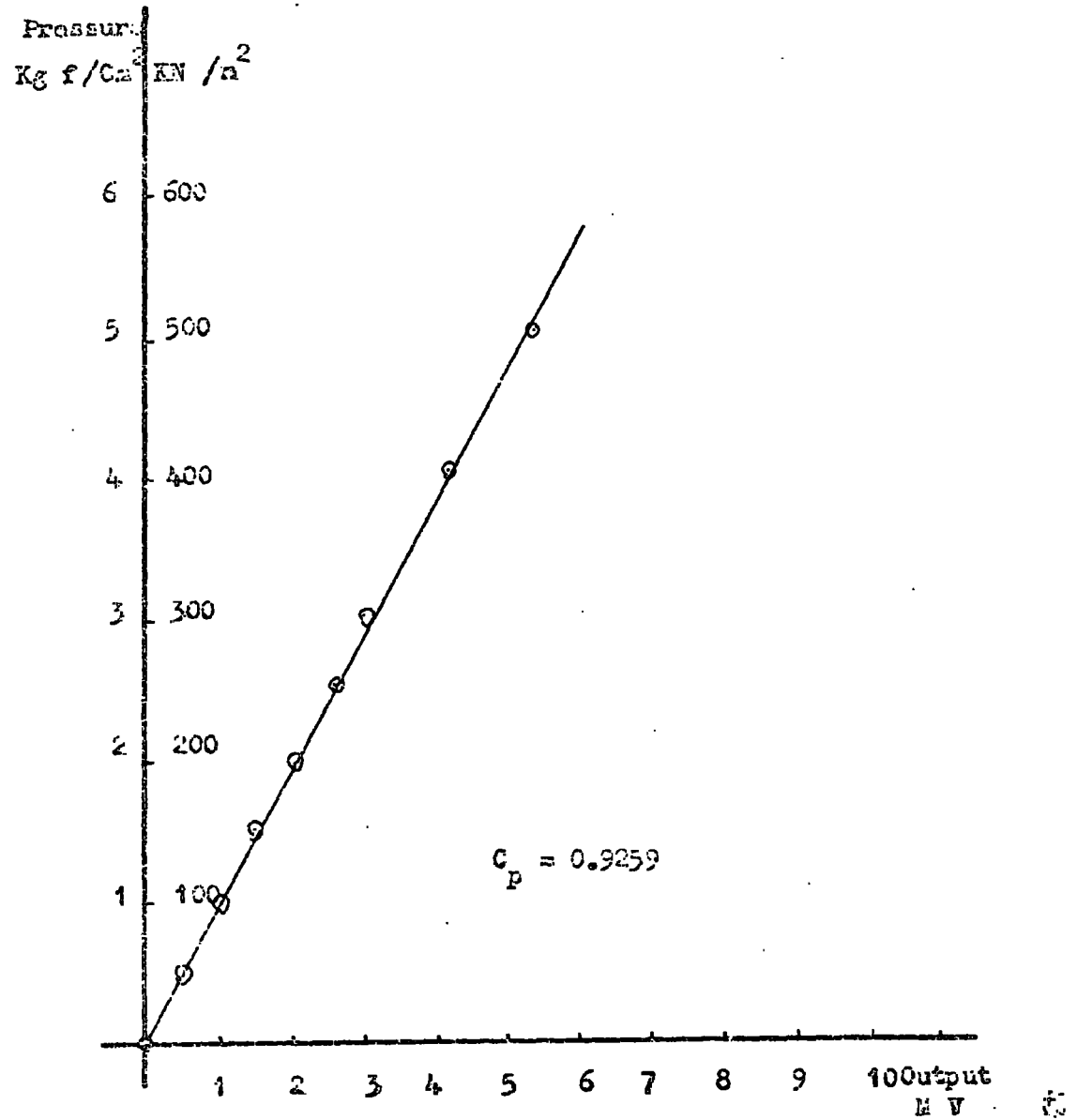


Figure 35 Calibration charts for pressure Cell No. 3

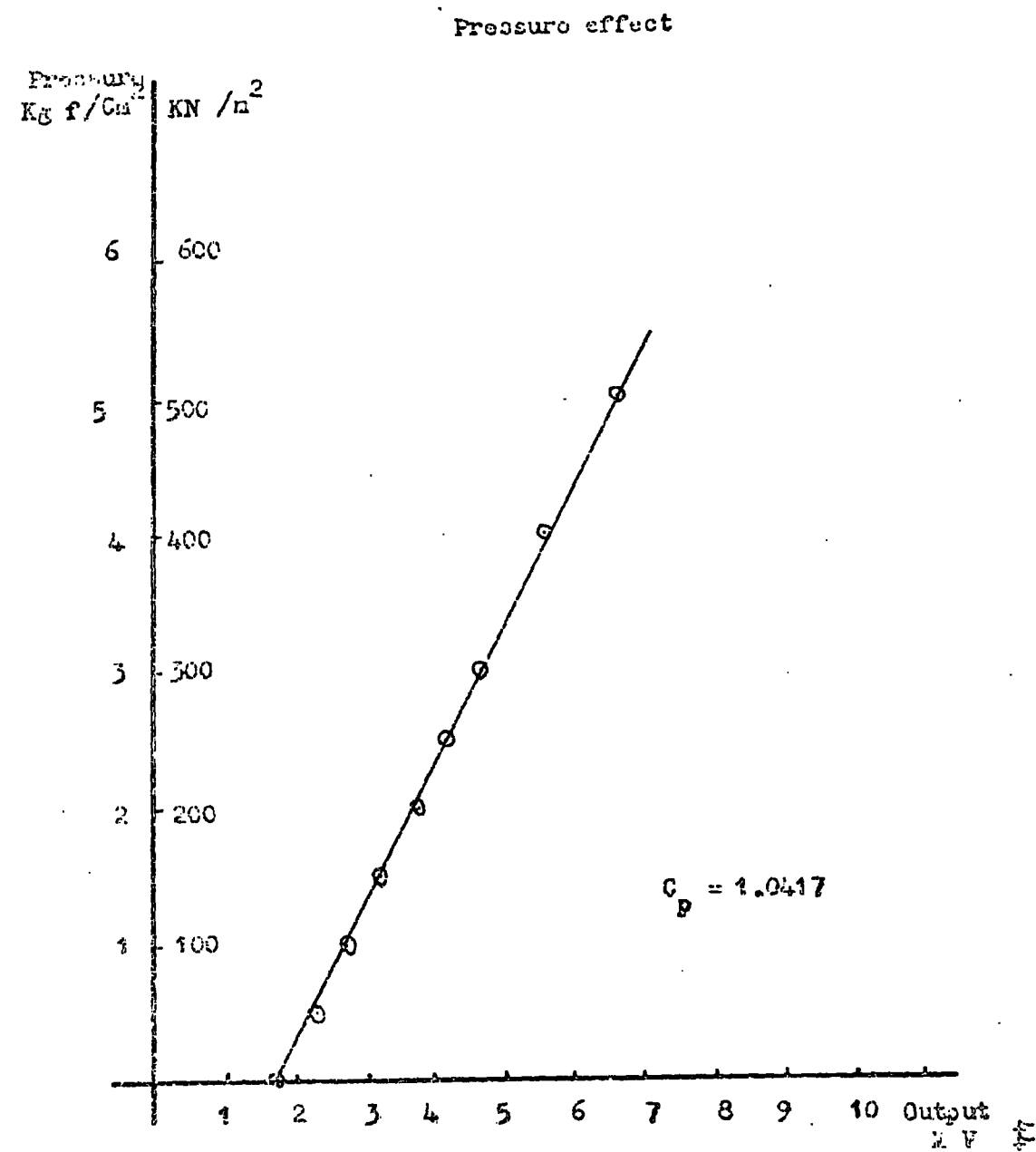
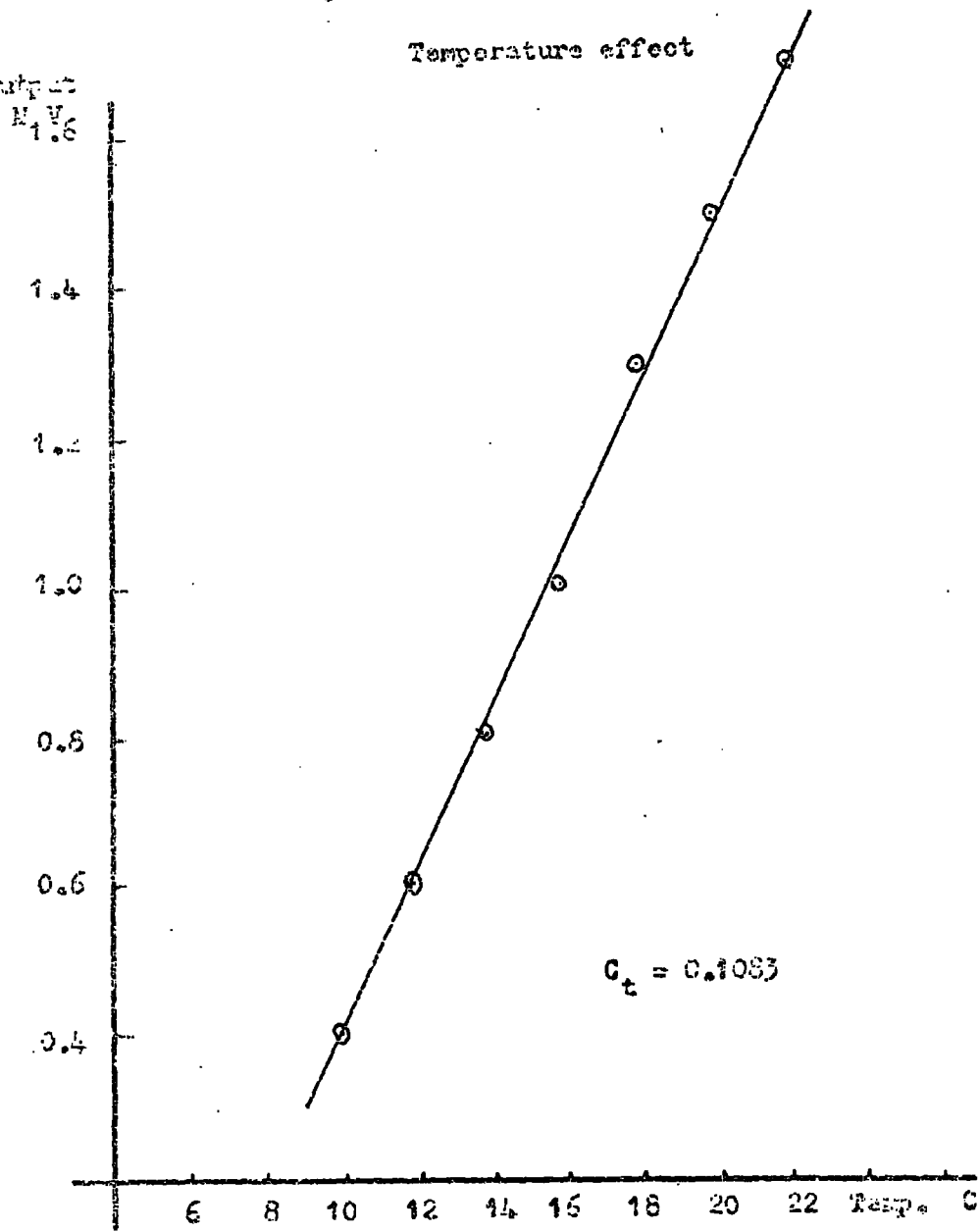
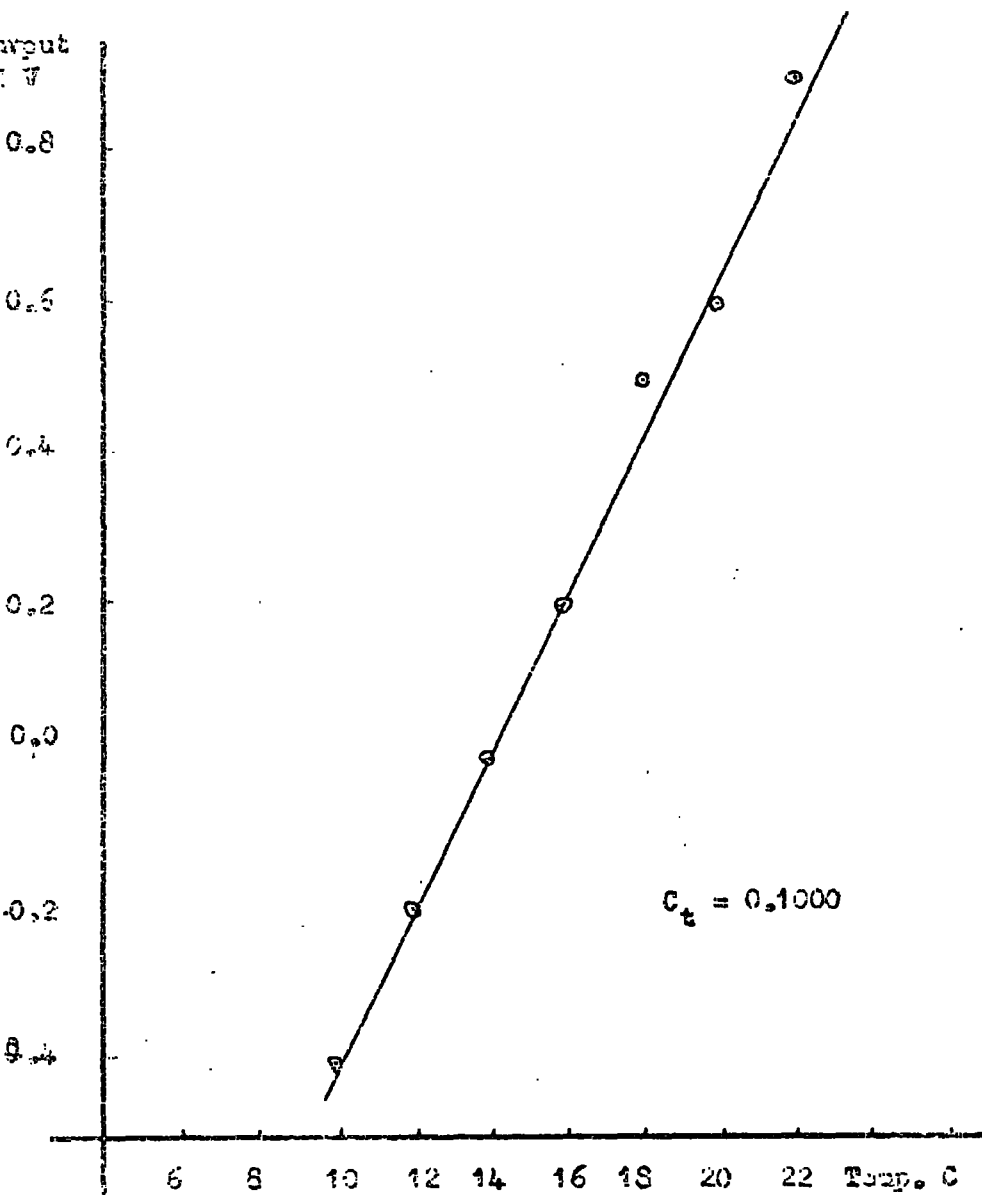


Figure 36 Calibration charts for pressure Cell No. 4

Temperature effect



Pressure effect

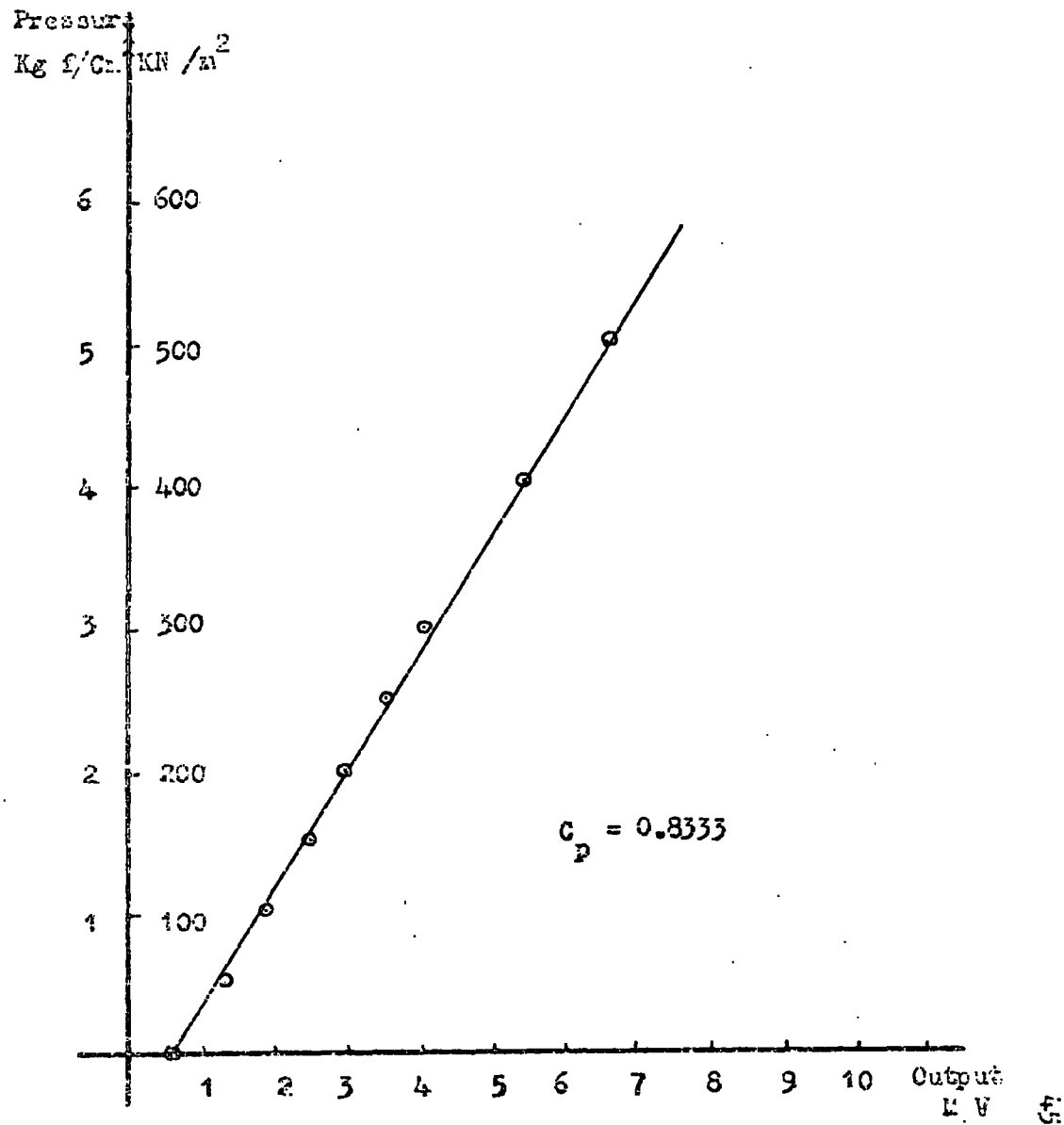
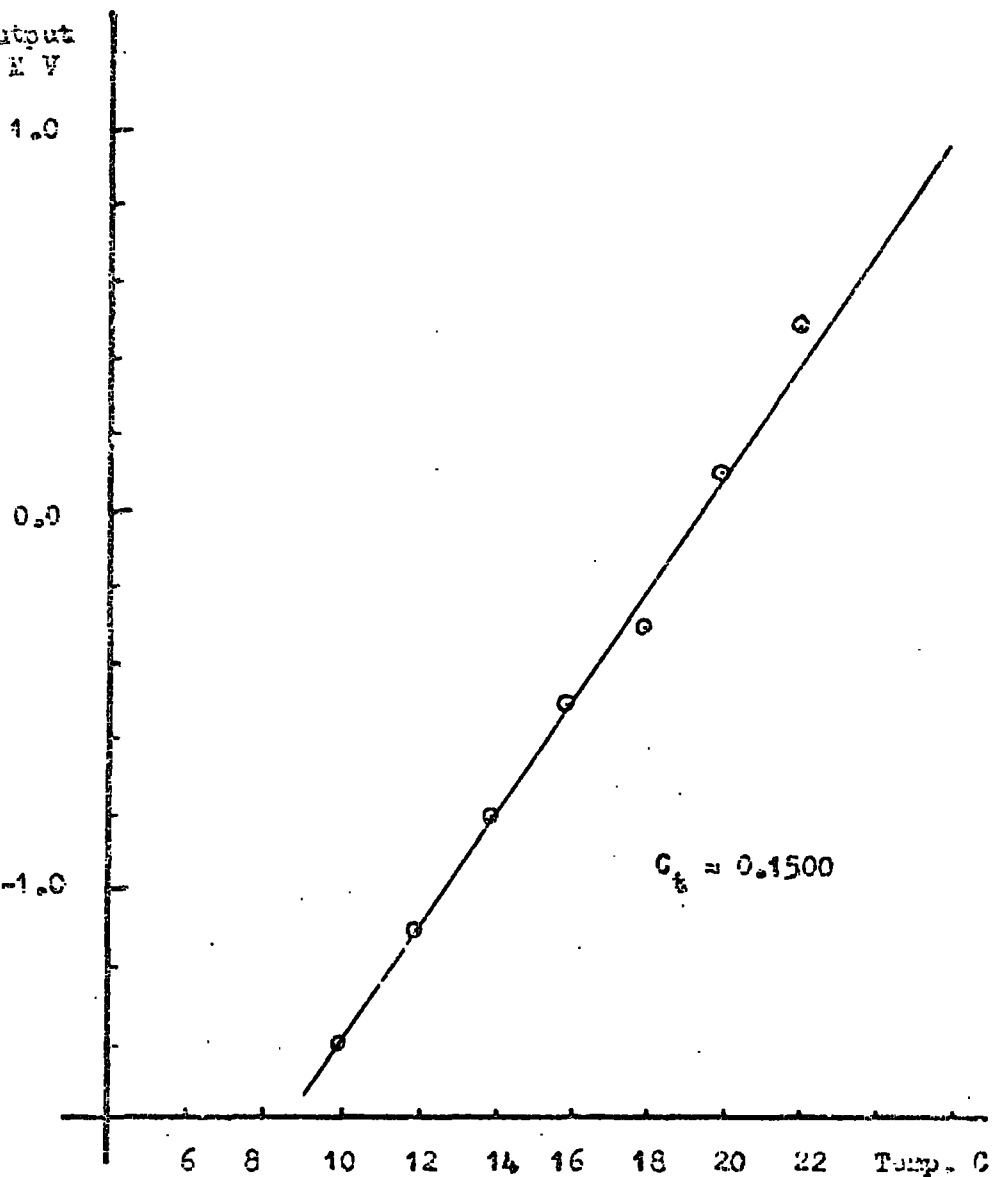


Figure 37 Calibration charts for pressure Cell No. 5

Temperature effect



Pressure effect

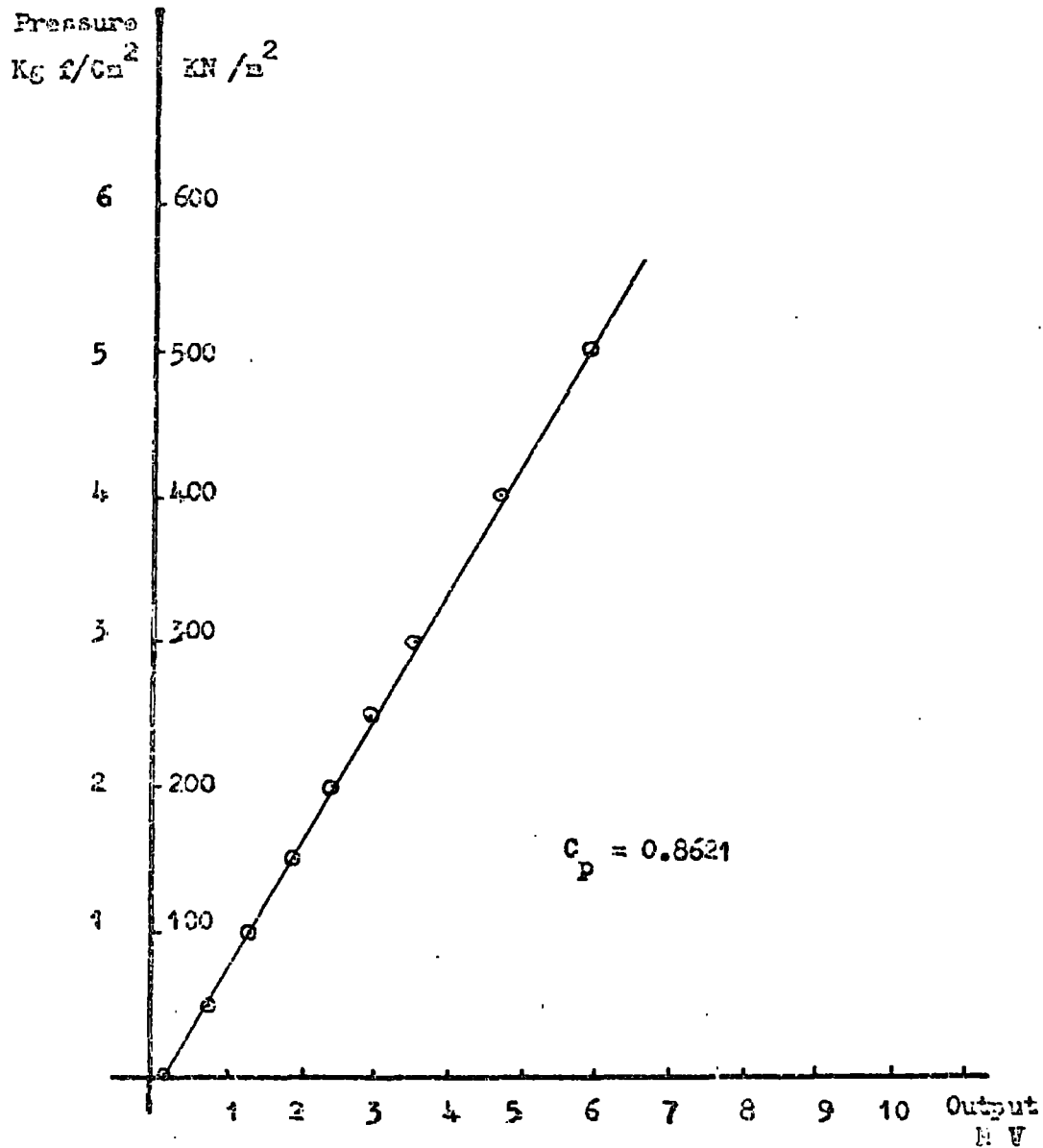


Figure 38 Calibration charts for pressure Cell No. 6

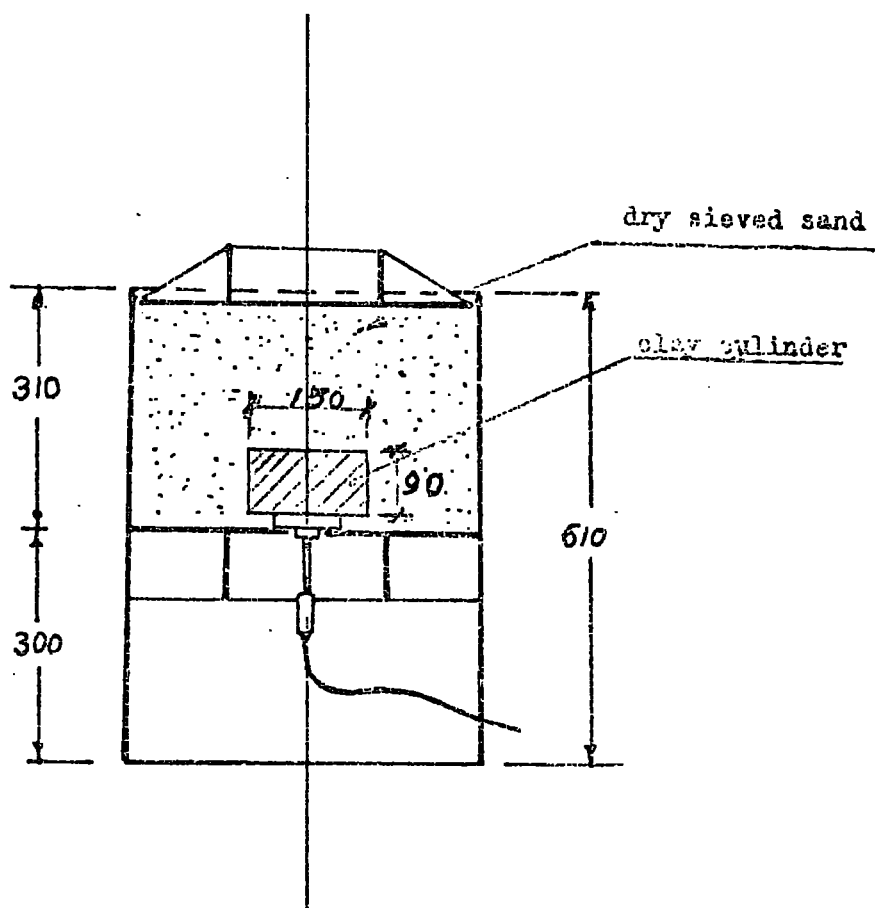


Figure 59 Section through the calibration tank showing the position of the clay cylinder .

CELL Kg/cm <sup>2</sup> Pressure	No. 1 at 20 C	No. 2 at 18 C	No. 3 at 20 C	No. 4 at 22 C	No. 5 at 20 C	No. 6 at 20 C
0.00	1.1	0.8	0.0	1.7	0.6	0.1
0.5	1.4	1.1	0.5	2.3	1.3	0.7
1.0	1.7	1.4	1.0	2.8	1.9	1.3
1.5	2.0	1.8	1.5	3.3	2.5	1.9
2.0	2.3	2.1	2.0	3.8	3.0	2.4
2.5	2.5	2.5	2.5	4.2	3.5	2.9
3.0	2.8	2.8	3.0	4.6	4.0	3.5
4.0	3.3	3.3	4.2	5.6	5.4	4.7
5.0	3.8	4.0	5.4	6.5	6.6	5.9

Table 4 Results of calibration tests for the pressure cells using dry sand as a testing medium

CELL °C TEMP.	No. 1	No. 2	No. 3	No. 4	No. 5	No. 6
10	0.1	0.1	-0.7	0.4	-0.4	-1.4
12	0.3	0.3	-0.5	0.6	-0.2	-1.1
14	0.5	0.5	-0.4	0.8	0.0	-0.8
16	0.7	0.6	-0.3	1.0	0.2	-0.5
18	0.9	0.8	-0.1	1.3	0.5	-0.3
20	1.1	1.0	0.0	1.5	0.6	0.1
22	1.4	1.2	0.1	1.7	0.9	0.5

Table 5 Results of temperature calibration tests (second experiment)

### Calibration Equations.

The calibration tests specified earlier result in the calculation of cell pressure coefficient " $C_p$ " and cell temperature coefficient " $C_t$ ".

It was noted that the two calibration curves derived under hydraulic pressure at two different temperatures (Figures 21 to 26) are mutually parallel, so implying that a temperature change of  $t^{\circ}\text{C}$  shifts the calibration chart an amount equal to " $C_t t$ ". Thus the calibration equations for the cells may be expressed in the following form:

$$P = C_p \{ R - (R' - C_t (T' - T)) \}$$

where  $P$  = the external measured pressure,

$C_p$  = cell pressure coefficient,

$C_t$  = cell temperature coefficient,

$T'$  = calibration temperature,

$T$  = measured temperature,

$R'$  = calibration - no load-output,

and  $R$  = measured output.

The values of  $C_p$ ,  $C_t$ ,  $R'$ ,  $T'$  and the calibration equations of the pressure cells used in the first experiment are tabulated in Table 6, and that of the pressure cells used in the second experiment are tabulated in Table 7.

CELL	$C_p$	$C_t$	R	T	Calibration equation
No.1	0.5747	0.1727	17.7	20	$P = 0.5747 ( R - ( 17.7 - 0.1727 ( 20 - T ) ) )$
No.2	0.5319	0.2563	5.6	20	$P = 0.5319 ( R - ( 5.6 - 0.2563 ( 20 - T ) ) )$
No.3	0.8197	0.1547	2.7	20	$P = 0.8197 ( R - ( 2.7 - 0.1547 ( 20 - T ) ) )$
No.4	0.3731	0.4077	5.4	19	$P = 0.3731 ( R - ( 5.4 - 0.4077 ( 19 - T ) ) )$
No.5	0.3597	0.3214	2.9	20	$P = 0.3597 ( R - ( 2.9 - 0.3214 ( 20 - T ) ) )$
No.6	0.3145	0.4071	5.9	20	$P = 0.3145 ( R - ( 5.9 - 0.4071 ( 20 - T ) ) )$

Table 6  $C_p$ ,  $C_t$ , R, T and calibration equations of the pressure cells used in the first experiment.



CELL	$C_p$	$C_t$	$R'$	$T'$	Calibration equation
No. 1	1.7857	0.1000	1.1	20	$P = 1.7857 ( R - ( 1.1 - 0.1000 ( 20 - T ) ) )$
No. 2	1.5152	0.0860	0.8	18	$P = 1.5152 ( R - ( 0.8 - 0.0860 ( 18 - T ) ) )$
No. 3	0.9259	0.0700	0.0	20	$P = 0.9259 ( R - ( 0.0 - 0.0700 ( 20 - T ) ) )$
No. 4	1.0417	0.1083	1.7	22	$P = 1.0417 ( R - ( 1.7 - 0.1083 ( 22 - T ) ) )$
No. 5	0.8333	0.1000	0.6	20	$P = 0.8333 ( R - ( 0.6 - 0.1000 ( 20 - T ) ) )$
No. 6	0.8621	0.1500	0.1	20	$P = 0.8621 ( R - ( 0.1 - 0.1500 ( 20 - T ) ) )$

Table 7  $C_p$ ,  $C_t$ ,  $R'$ ,  $T'$ , and calibration equation of the pressure cells.

(second experiment)

## CHAPTER 3

### FIELD INSTALLATION, FIELD MEASUREMENT AND DATA

#### RECORDING

##### 3.1 Installation of the pressure cells.

Installation of the pressure cells was performed with great care, since the quality of installation influences directly the accuracy and the reliability of the results. The pressure cells were installed, during the construction of the lining segments, through six of the twelve grouting holes in each lining ring.

Each pressure cell was installed in such a way that the cell body, part A, remained outside the lining with the sensing diaphragm facing the soil. The pressure transducer, the most delicate part of the cell, remained inside the tunnel in order to minimize the possibility of damage and also to allow its recovery once its useful recording life was over. Each cell axis was adjusted in such a way that the sensing diaphragm was parallel to the tangent passing through the cut circular surface of the clay at the point of cell installation. Thus, the measured pressures represented the normal, radial soil-lining interaction pressures active at the point in question. The lower cells were protected against any damage which could occur from the traffic inside the tunnel.

The cables connecting the pressure cells to the electronic recording equipment were protected against dampness and damage by using a special protective tape. The electronic equipment used in the experiments was kept inside a locked cupboard, as shown in Figure 44.

The arrangement and the positions of the pressure cells are shown in Figures 40 and 41 for the first and second experiment respectively. Figures 43 to 49 represent photographs of the pressure cells and the electronic equipment used in the two experiments.

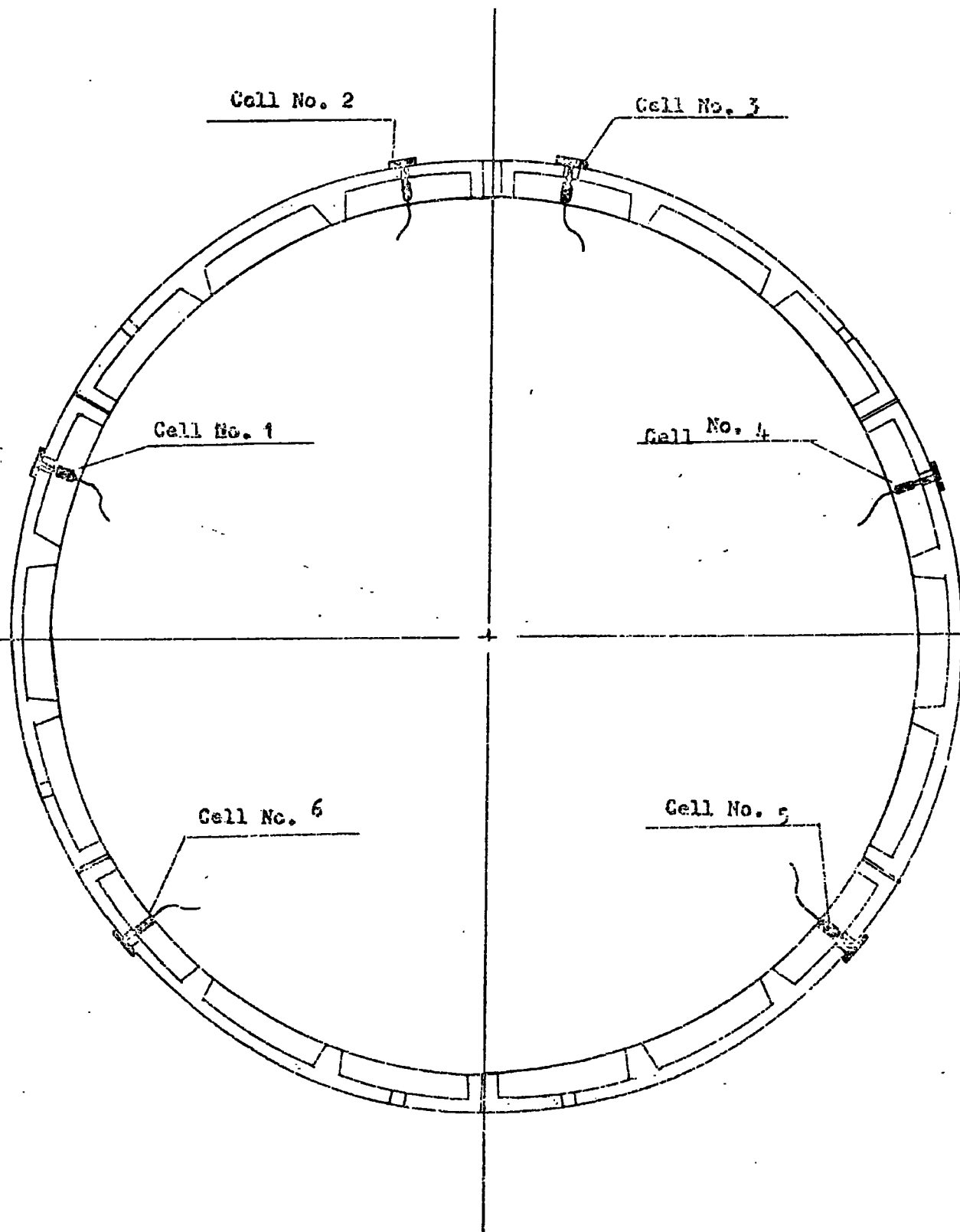


Figure 40 Position of cells (first experiment)

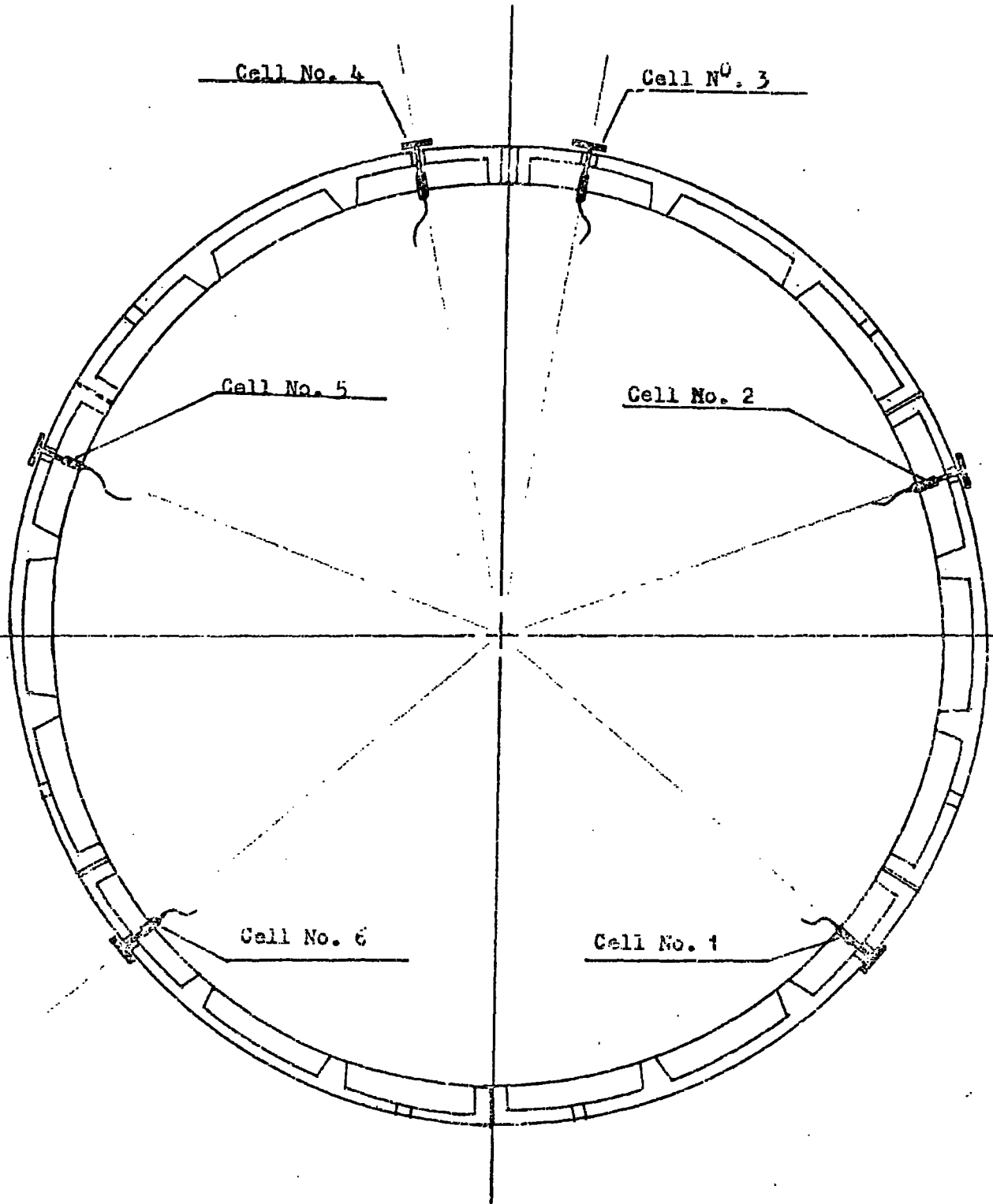


Figure 41 Position of cells (second experiment)



Figure 42 Pressure cells Nos 2 and 3 in the first experiment



Figure 43 View of the tunnel showing the box used for the protection of the electronic equipment



Figure 44 Electronic equipment used for data recording  
in the first experiment



Figure 45 Pressure cells Nos 3 and 4 in the second experiment

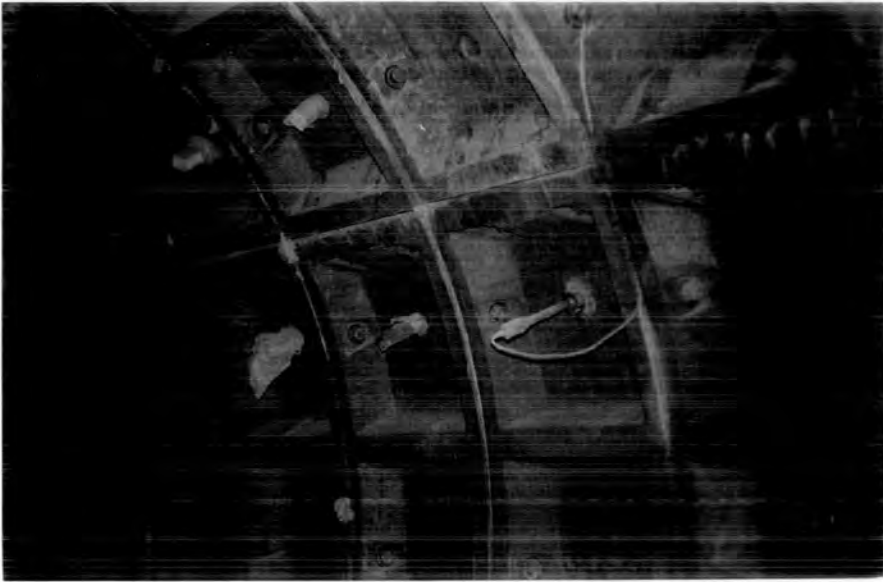


Figure 46 Pressure cell No 2 in the second experiment

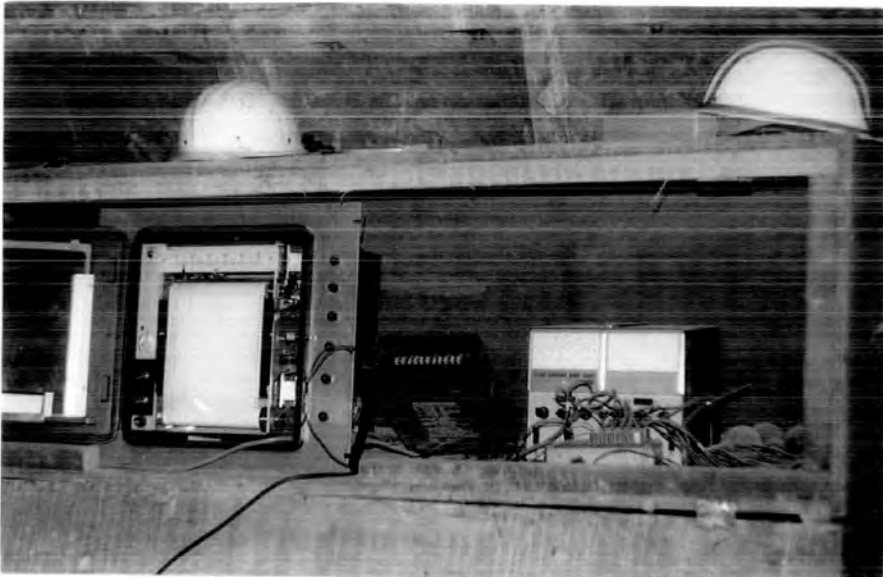


Figure 47 Electronic equipment used for data recording  
in the second experiment

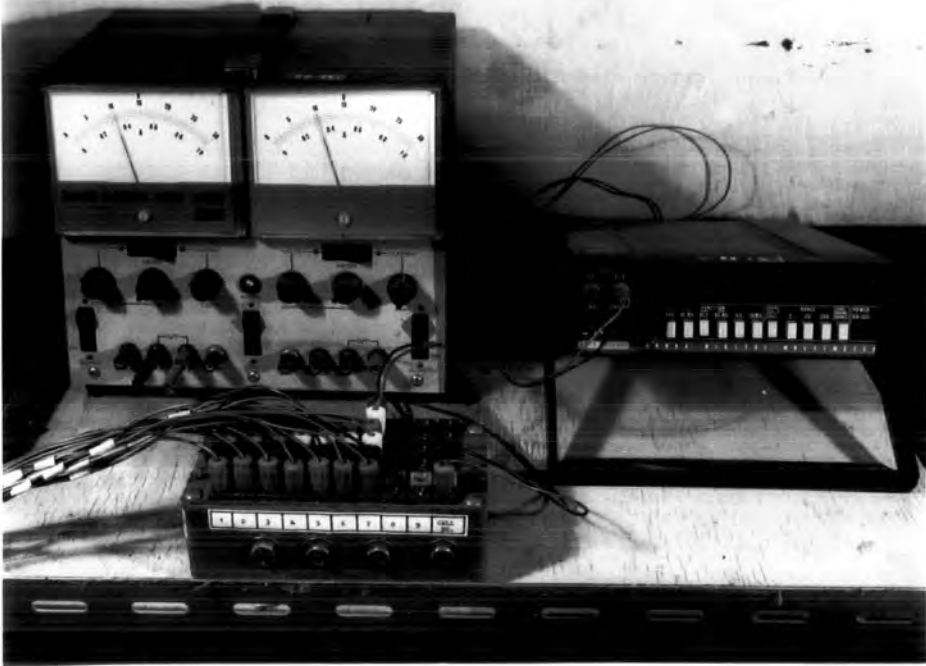


Figure 48 Power supply, voltmeter, and connecting box

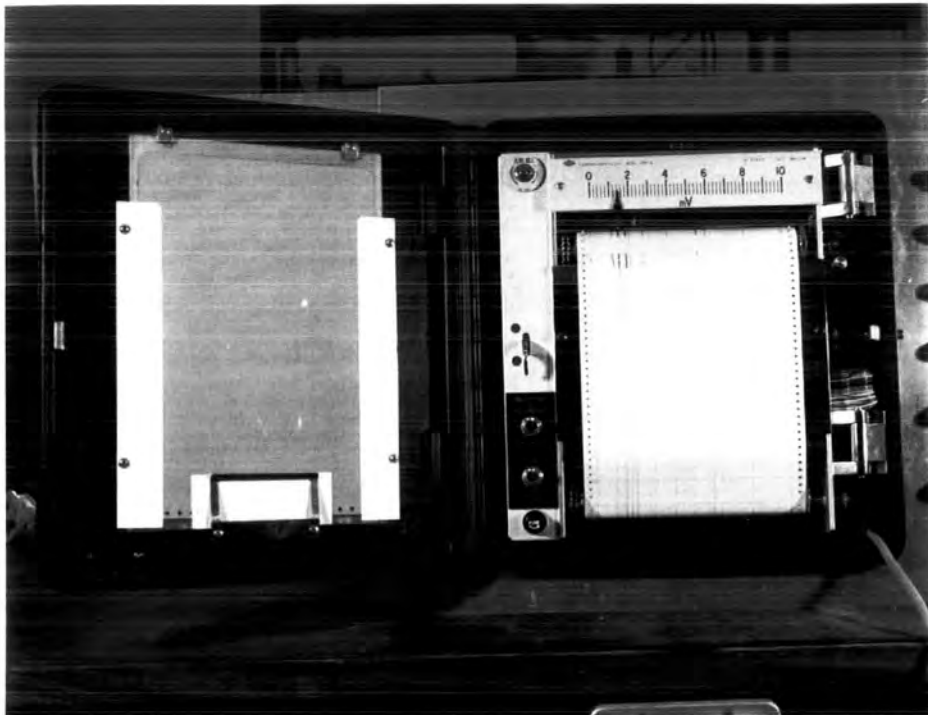


Figure 49 The six channel recorder used for the data recording



### 3.2 The soil formation

The tunnel was driven through layers of stiff stony clay and laminated clay. Figures 50 and 51 show the logs of boreholes No.C1 and H53, the locations of which are shown in Figure 1. Laboratory tests were conducted on representative samples obtained from the tunnel face in order to evaluate the soil unit weight " $\gamma$ ". Limits of consistency and the unconfined strength (via the undrained triaxial test) were also determined. The results of these laboratory tests are tabulated in Table 8.

### 3.3 Measurement of the changes in the tunnel diameter.

Changes in the internal tunnel diameter were measured in the four directions shown in Figure 52. Eight rectangular steel plates, 20 x 30 x 4 mm, were fixed on the internal side of the lining. The measuring points were located by a circular hole 3 mm diameter in each of the plates.

Diametral changes were monitored using a 0.01 mm dial gauge fixed to a circular aluminium bar 50 mm in diameter, with a conical end, as shown in Figure 52. Figures 53 and 54 are photographs taken during the tunnel measurements of lining deformation.

### 3.4 Data recording.

A six channel recorder (Figure 49) was used for recording the output of the pressure cells continuously during the two experiments. The pressure cells were connected to the power supply and the output recorder through a connecting box, as shown in Figure 48.

The results of the two experiments are tabulated in Tables 9 and 10, and a detailed discussion and analysis of the derived data will be found in Chapter 4.

# RECORD OF BOREHOLE NO. C 1

Ground level : 83.8ft above O.D. Newlyn

Dia. of boring : 8in

Type of boring : Shell and Auger

Lining tubes : 8in to 15ft


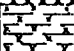
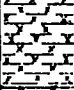
Daily Progress	Samples		Change of Strata			Description of Strata
	Depth	Type	Legend	Depth	O.D. level	
	2'6"	D				FILL (clay, gravel and ashes)
	3'6" - 4'6"	C(7) BD				
	3'0" - 4'6"					
	6'6"	D		6'0"	77.6	Firm to stiff mottled grey and brown silty CLAY
	8'0" - 9'6"	U(4) D				
	11'6"	D		11'6"	72.3	Stiff to very stiff grey-brown sandy silty CLAY with fine to medium gravel, becoming less sandy below 35ft
	16'6"	D				
	18'6" - 19'6"	U(4)* D				
	19'6"					
	21'6"	D				
25.11.68	26'0"	D				
	28'6" - 30'0"	U(4) D				
	30'0"					
	32'6"	D				
	33'6" - 35'0"	U(4) D				
	35'0"					
	37'6"	D				
	38'6" - 40'0"	U(4) D				
	40'0"					
	42'6"	D				
	43'6" - 45'0"	U(4) C				
	45'0"					
	47'6"	D				
26.11.68	48'6" - 50'0"	U(4) D				
	50'0"					
	52'6"	D				
	53'6" - 55'0"	U(4) D				
	55'0"					
	57'6"	D				
27.11.68	58'6" - 60'0"	U(4) D				
	60'0"		60'0"	23.8		

Figure 50 Record of borehole No. C 1 .

# RECORD BOREHOLE H53

Co-Ords. 33409 m.E. 66617 m.N.

Ground level: 78.3 ft above O.D. Newlyn

Dia. of boring: 8 in

Method of boring: Shell and Auger

Lining tubes: 8 in to 49ft 9 in


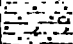
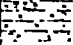
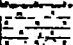
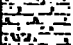
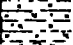
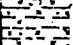
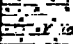
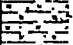
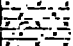
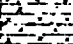
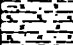
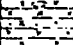
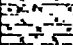
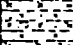
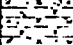
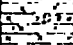
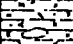
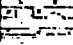
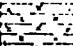
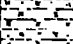
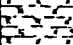
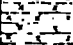
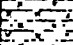
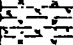
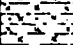
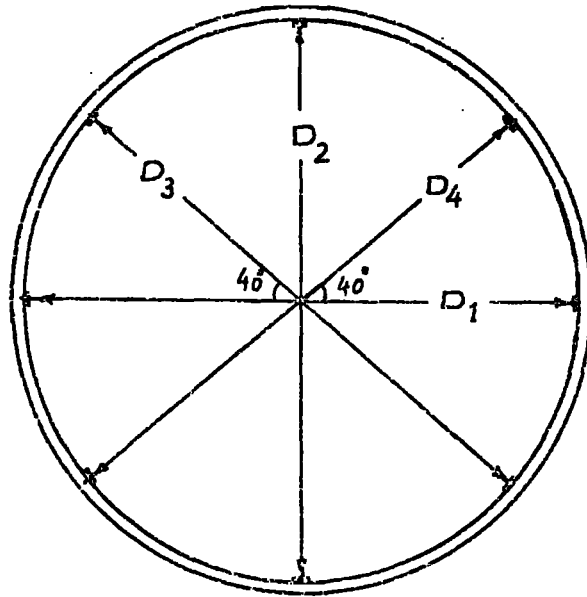
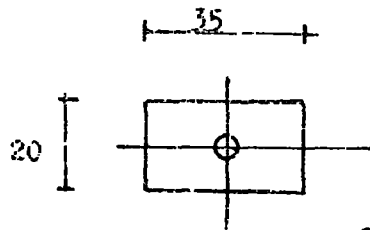
Daily Progress	Samples		Change of Strata			Description of Strata
	Depth	Type	Legend	Depth	O.D. Level	
	1'0"	D		1'9"	76.5	FILL (ashes and coal fragments)
	2'6" - 4'0"	U(4) D			73.3	Firm to stiff brown silty CLAY with occasional fine gravel and coal fragments
	5'6" - 7'0"	U(4) D		5'6"	72.8	
	9'0"	D			72.4	
	10'6" - 12'0"	U(4) D				Very stiff, becoming firm, brown with grey veining sandy silty CLAY with occasional gravel and coal fragments; thin bands of sand between 17ft 6in and 18ft 6in
	14'0"	D				
	15'6" - 17'0"	U(4) BD D				
	17'0" - 18'6"	U(4) D		18'6"	59.8	
	20'6"	D			59.2	
	22'0" - 23'6"	U(4) D				Stiff to very stiff brown sandy silty CLAY with fine gravel and occasional coal fragments; occasional cobbles below 30ft
	25'6"	D				
	27'0" - 28'6"	U(4) D				
8.9.69	30'6"	D				
	33'6"	D		32'0"	45.2	
	33'6" - 34'6"	U(4) D			45.2	
	35'0"	D				
	37'0"	D				
	38'6" - 40'0"	U(4) D				Firm to stiff laminated brown silty CLAY with partings of silty fine sand
	42'0"	D				
	43'6" - 45'0"	U(4) D				
	47'0"	D		47'0"	31.3	
	47'6" - 49'0"	U(4) C			31.3	
	51'6"	D				
	52'6" - 54'0"	U(4) D				Firm to very stiff grey-brown sandy silty CLAY with fine gravel and occasional coal fragments
	56'0"	D				
9.9.69	56'6" - 58'0"	U(4) D		58'0"	29.3	

Figure 51 Record of borehole No. H 53.



Section through the lining showing position  
of the steel plates .



one of the steel plates used

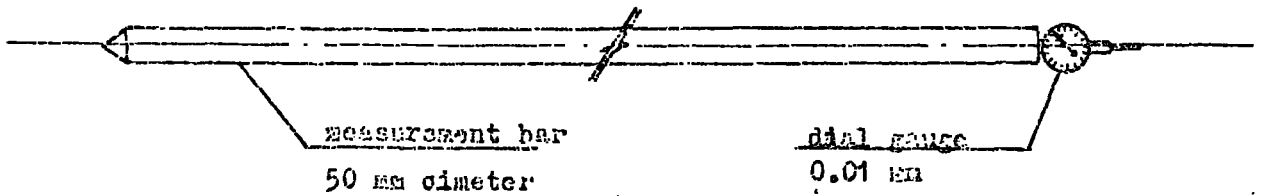


Figure 52 Position of steel plates , the steel plate , and  
the measurement bar used in the tunnel diameter measurement .



Figure 53 Measuring of the tunnel diameter changes

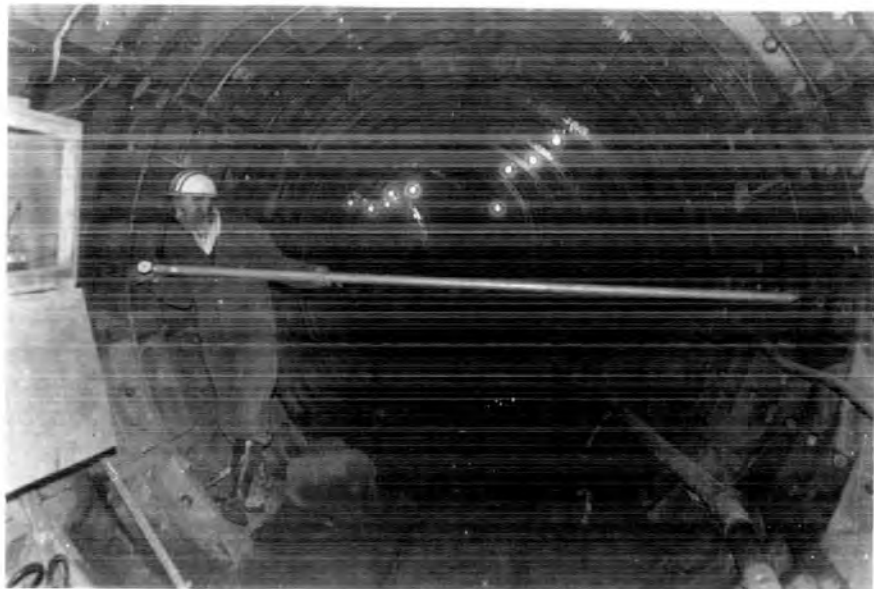


Figure 54 Measuring of the tunnel diameter changes

Clay type Lab. test	Laminated clay	Stony clay
$\gamma_s$ "unit weight"	2.0298 gm / cm <sup>3</sup> 126.8625 lb / ft <sup>3</sup>	2.2550 gm / cm <sup>3</sup> 140.9358 lb / ft <sup>3</sup>
L.L.	63.5	36.5
P.L.	30.00	18.18
e	27.17	12.09
c	0.9 Kgf/ cm <sup>2</sup> 12.80 lbf/ ft <sup>2</sup>	2.1 Kgf/ cm <sup>2</sup> 29.87 lbf/ ft <sup>2</sup>

Table 8 Results of the laboratory tests .

CELL	Angle of the cell axis with the Hl.	Depth "h" of the cell "m"	Over burden pressure " $\gamma h$ Kgf/Cm <sup>2</sup> "	Maximum measured Pressure "P <sub>max</sub> "	P <sub>max</sub> / $\gamma h$ %
No. 1	20°	13.01	2.79	1.097	39
No. 2	80°	11.77	2.52	0.954	38
No. 3	80°	11.77	2.52	1.298	52
No. 4	20°	13.01	2.79	1.062	38
No. 5	-40°	14.38	3.08	0.773	25
No. 6	-40°	14.38	3.08	0.705	23

Table 9 Over burden Pressure , maximum measured pressure , P<sub>max</sub> /  $\gamma h$  % of the pressure cells (first experiment) .

CELL	Angle of the cell axis with the Hl.	Depth 'h' of the cell 'm'	Over burden pressure ' $\gamma h$ Kg/cm <sup>2</sup> '	Maximum measured pressure ' $P_{max}$ '	$P_{max} / \gamma h$ %
No. 1	- 40	15.0000	3.2137	1.2500	38.9
No. 2	20	13.4228	2.8761	1.4303	49.7
No. 3	80	12.3943	2.6557	0.9629	36.3
No. 4	80	12.3943	2.6557	1.4234	53.6
No. 5	20	13.4228	2.8761	1.2500	43.5
No. 6	- 40	15.0000	3.2137	1.1207	34.9

Table 10 Over burden pressure , maximum measured pressure, and  $P_{max} / \gamma h$  % of the pressure cells (second experiment)



## CHAPTER 4

### ANALYSIS OF THE DERIVED DATA

#### 4.1 Analysis of the first experiment results

The outputs of the pressure cells were recorded continuously for a period of 50 days, the soil-lining interaction pressures being evaluated using the calibration charts shown in Figures 20 to 26. The pressure-time curves for the pressure cells are illustrated in Figures 55, 56 and 57.

Figure 56 shows that the maximum pressure recorded by pressure cells 2 and 3 near the tunnel crown is  $1.298 \text{ kgf/cm}^2$ , which is equivalent to 52% of the effective overburden pressure at the cell level.

Figure 55 shows that the maximum pressure indicated by pressure cells 1 and 4, the axes of which were at  $20^\circ$  with respect to the horizontal, is  $1.097 \text{ kgf/cm}^2$ , and this is equivalent to 39% of the effective overburden pressure at the cells level.

Figure 57 shows that the maximum pressure indicated by pressure cells 5 and 6, the axes of which were at  $-40^\circ$  with the horizontal, is  $0.775 \text{ kgf/cm}^2$ , which is equivalent to 25% of the effective overburden pressure at the cells level.

The pressure distribution around the tunnel lining after 1, 2, 5 days, and the final pressure distribution, are illustrated in Figures 58 to 61. From these Figures it is clear that the pressures were developed first of all at the crown and the invert of the tunnel, and as the tunnel lining began to deform the lateral passive pressures were gradually created.

The final pressure diagram (Figure 61) shows that the terminal pressure distribution around the tunnel lining is nearly uniform, and this means that

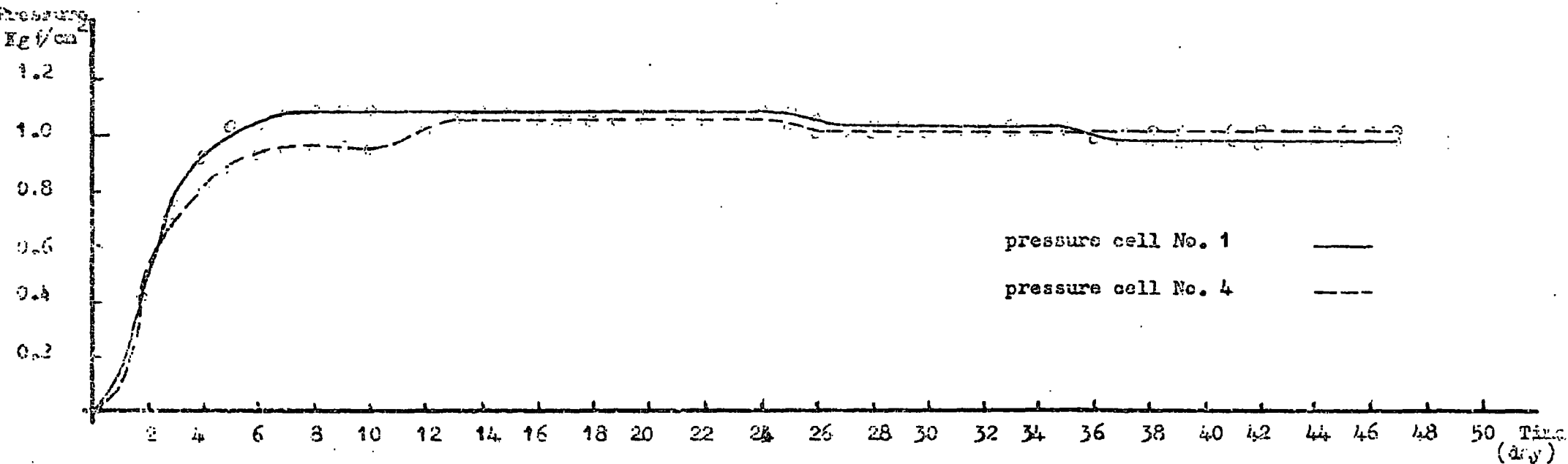


Figure 55 Pressure - time curve for the pressure cells No. 1 and 4.

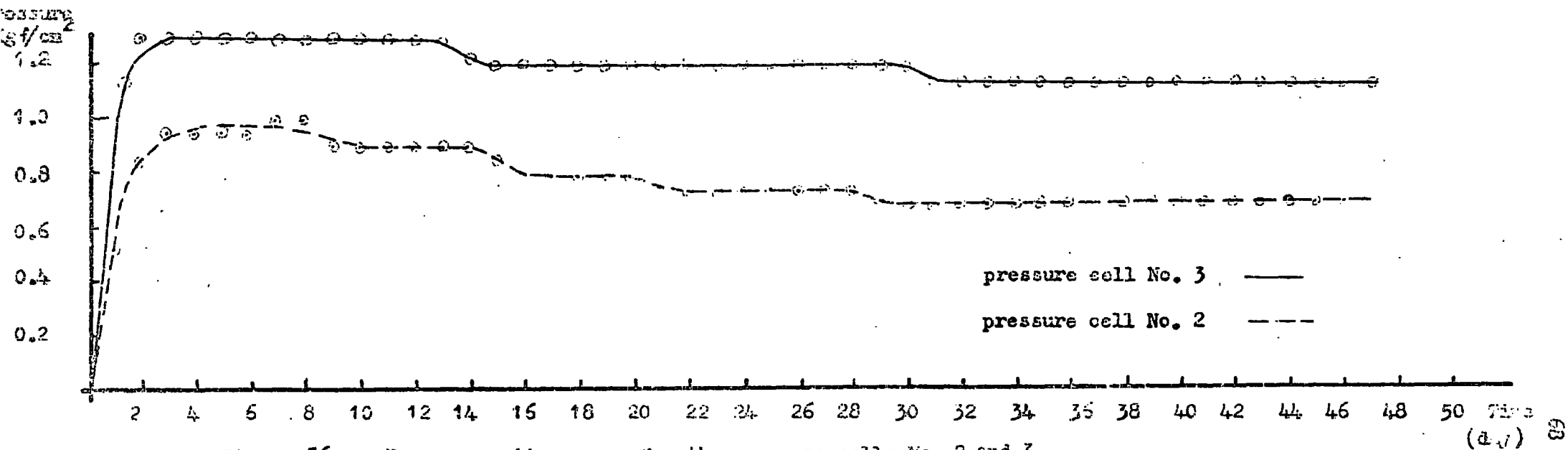


Figure 56 Pressure - time curve for the pressure cells No. 2 and 3.

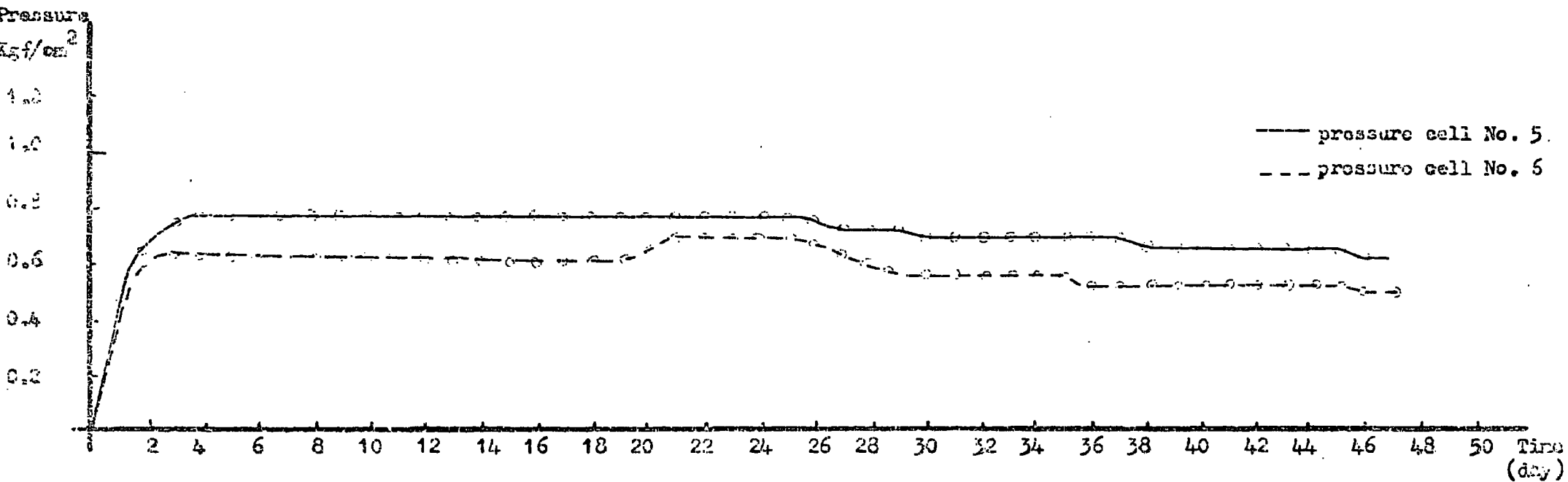


Figure 57 Pressure - time curve for the pressure cells No.5 and 6.

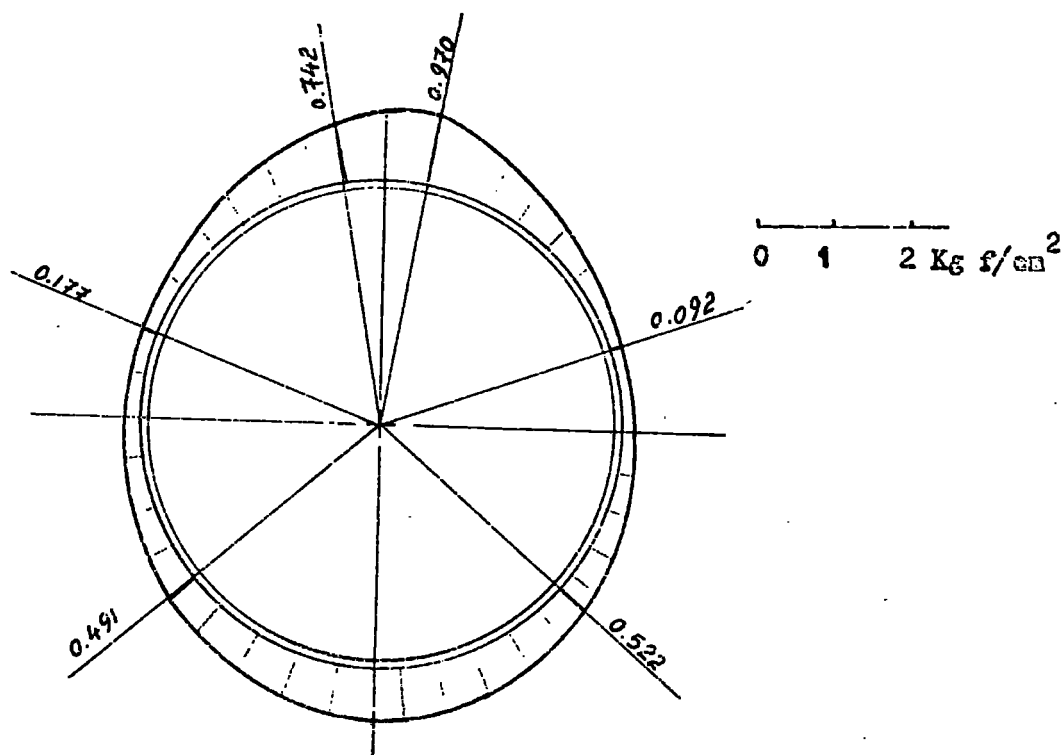


Figure 58 Pressure distribution around the tunnel lining one day after its construction.

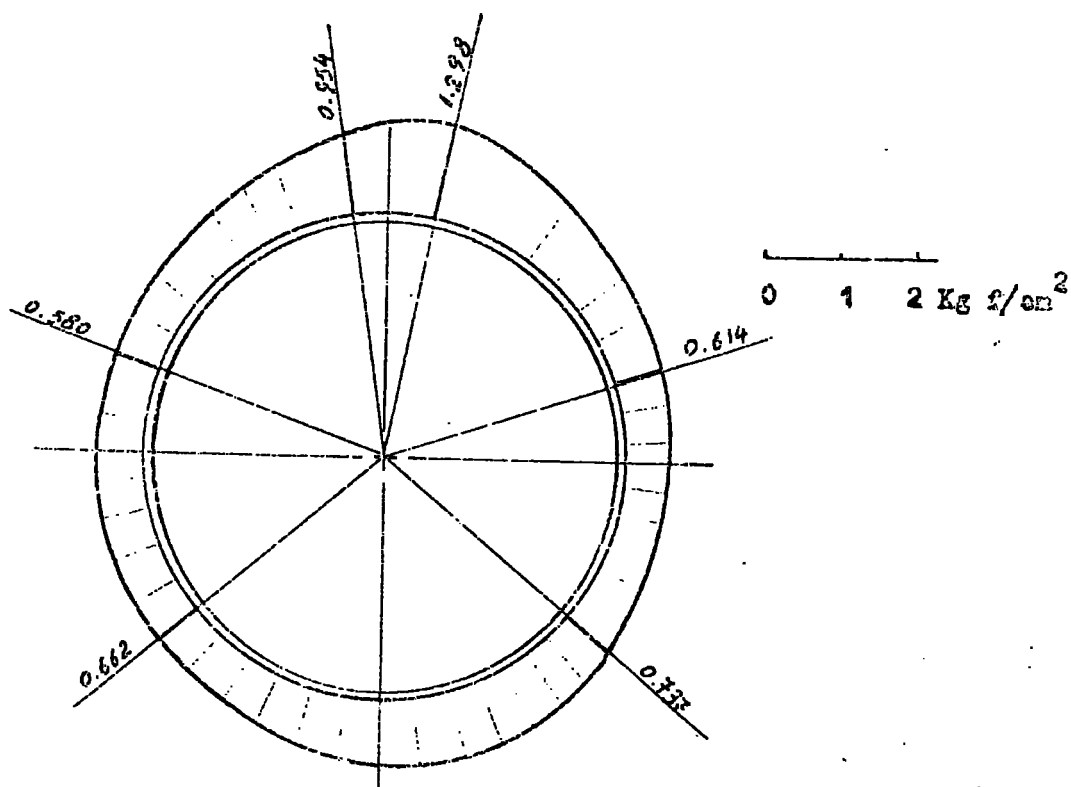


Figure 59 Pressure distribution around the tunnel lining two days after its construction.

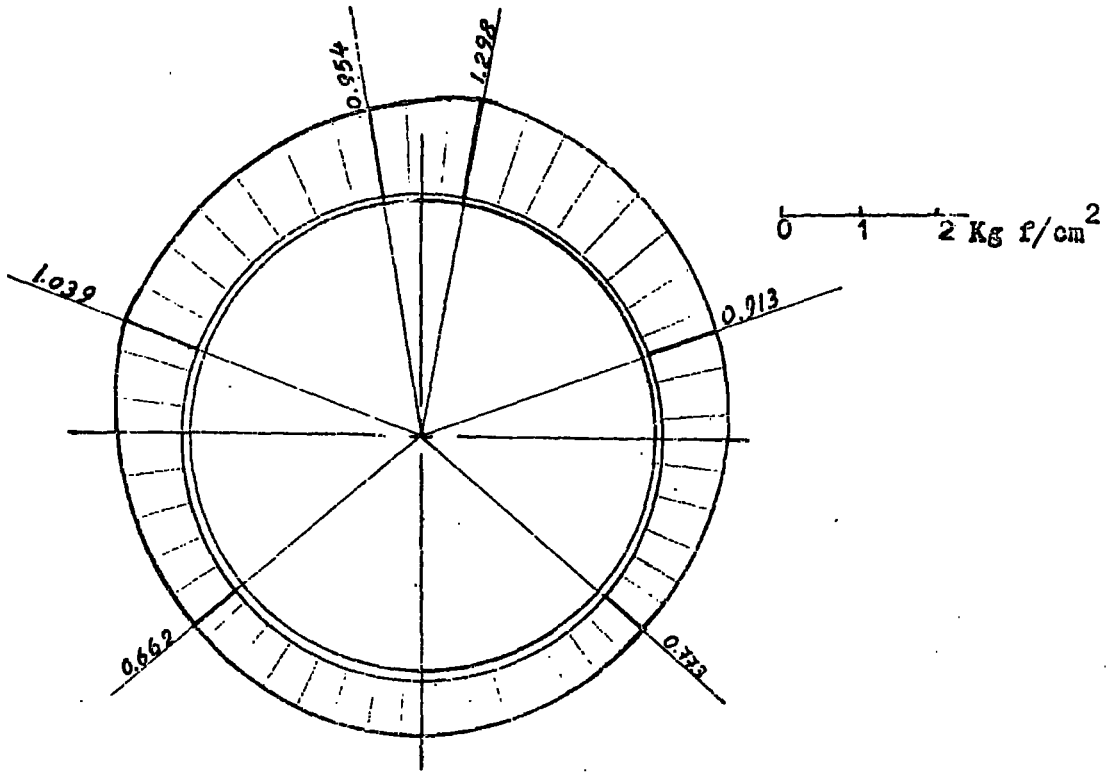


Figure 60 Pressure distribution around the tunnel lining five days after its construction.

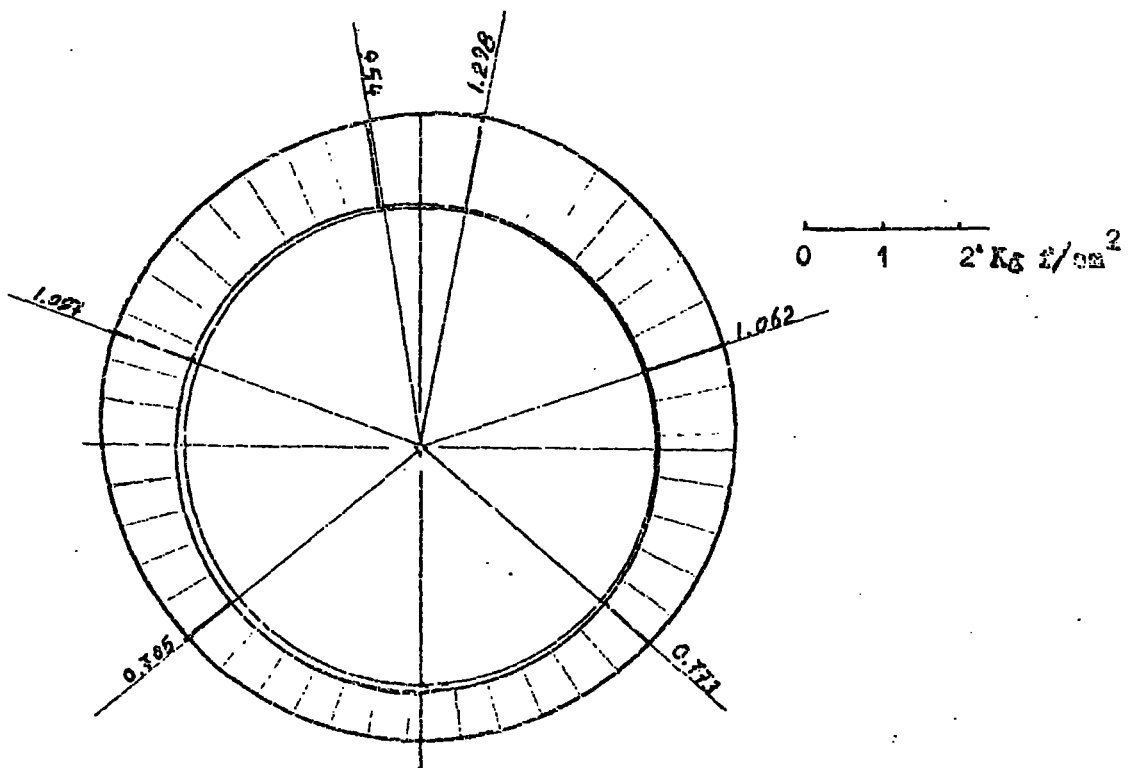


Figure 61 Final pressure distribution around the tunnel lining.

the tunnel lining is finally subjected to a uniform hoop stress.

Figures 62 to 67 represent  $P/P_{\max}$  and  $P/\gamma h$  against time curves for the six pressure cells used. From these figures it is clear that the top cells 2 and 3 reached their maximum pressures within a period of 2 to 3 days and this equally applied to the bottom cells 5 and 6. The lateral cells 1 and 4 achieved their maximum pressures within a period of 7 to 8 days. This suggests that the pressure distribution around the lining reached its final form after 7 to 8 days following lining erection.

#### 4.2 Analysis of the second experiment results.

The output of the pressure cells was recorded continuously for a period of 50 days, a time period similar to that of the first experiment. Pressure time curves for the pressure cells are illustrated in the Figures 68 to 70.

Figure 68 shows that the maximum pressure indicated by pressure cells 3 and 4 close to the tunnel crown is  $1.4234 \text{ kgf/cm}^2$ , which is equivalent to 53.6% of the effective overburden pressure at the cell level.

Figure 69 shows that the maximum pressure indicated by pressure cells 2 and 5, the axes of which were at  $20^\circ$  to the horizontal is  $1.4303 \text{ kgf/cm}^2$ , equivalent to 49.7% of the effective overburden pressure at the cell level.

Figure 70 indicates that the maximum pressure monitored by pressure cells 1 and 6, the axes of which were at  $-40^\circ$  with the horizontal, is  $1.2500 \text{ kgf/cm}^2$ , which is equivalent to 43.5% of the effective overburden pressure at the cell level.

The pressure distribution around the tunnel lining after 1, 2 and 5 days of its erection and the final pressure distribution are shown in Figures 71 to 74. These Figures prove that the pressure around the lining in the second experiment was generated in a similar manner to that in the first experiment. The final pressure distribution represented by Figure 74, shows

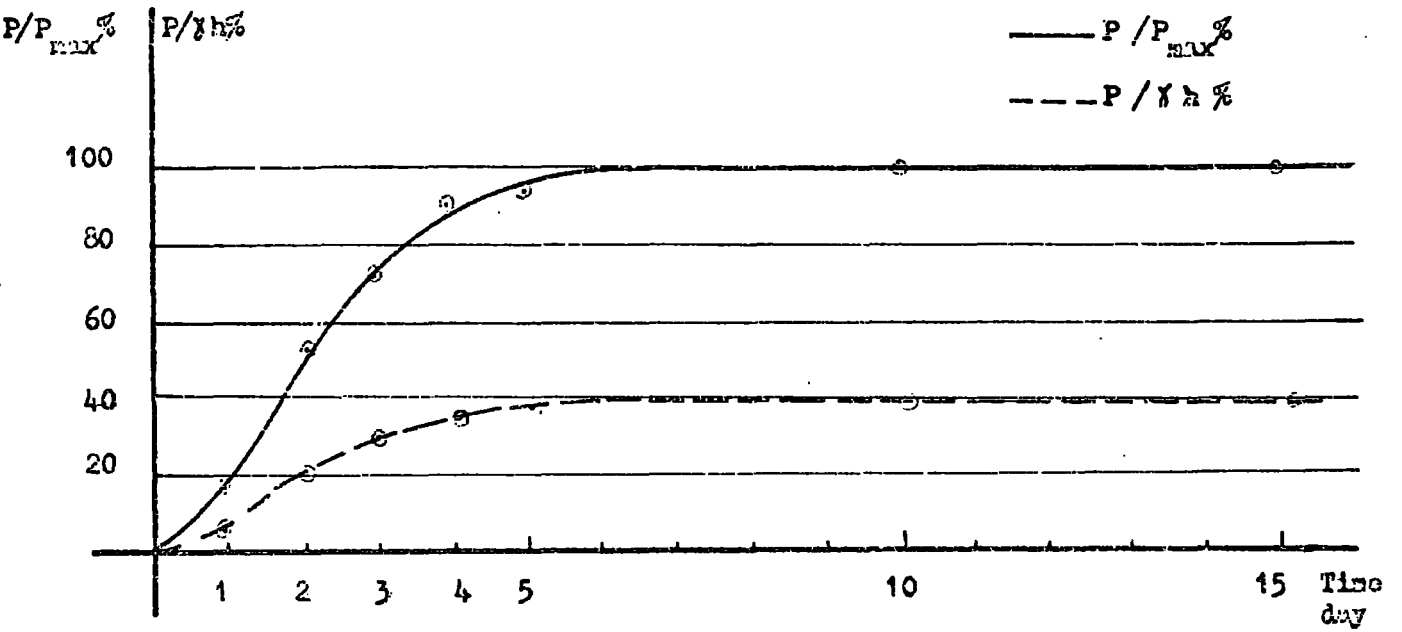


Figure 62  $P/P_{MAX} \%$  and  $P/g h \%$  -time curve of pressure call No. 1

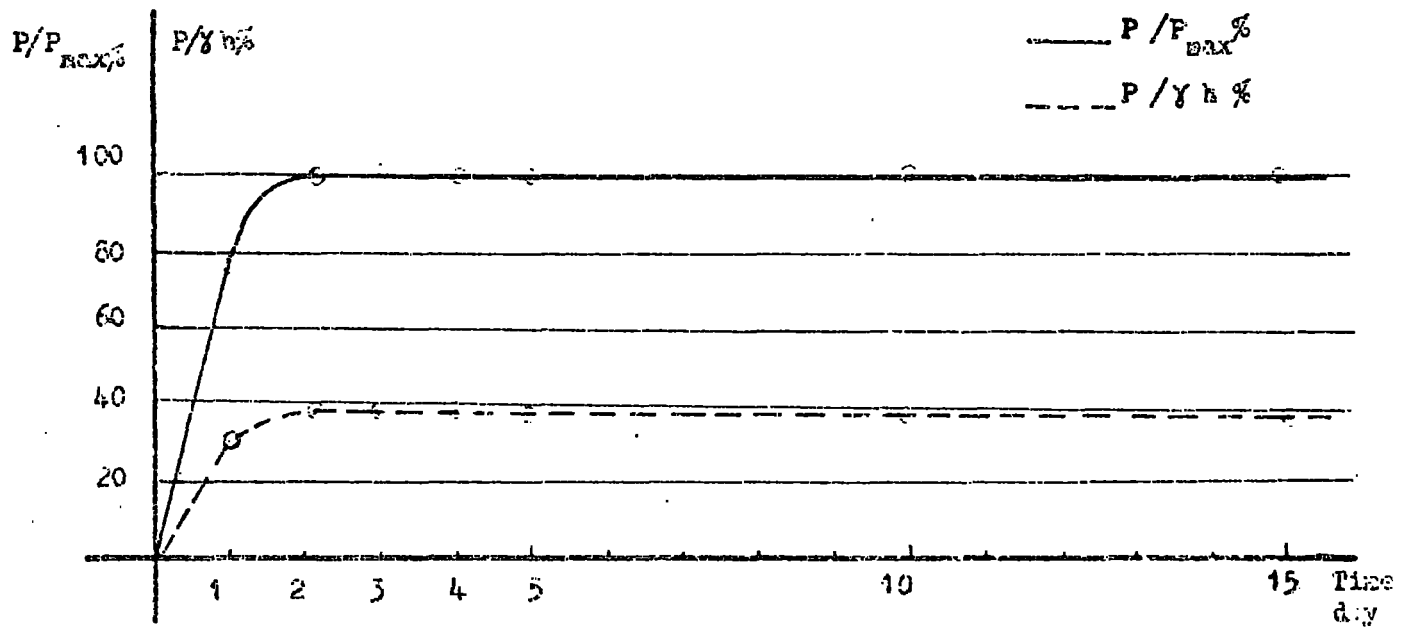


Figure 63  $P/P_{MAX} \%$  and  $P/g h \%$  - time curve of pressure call No. 2

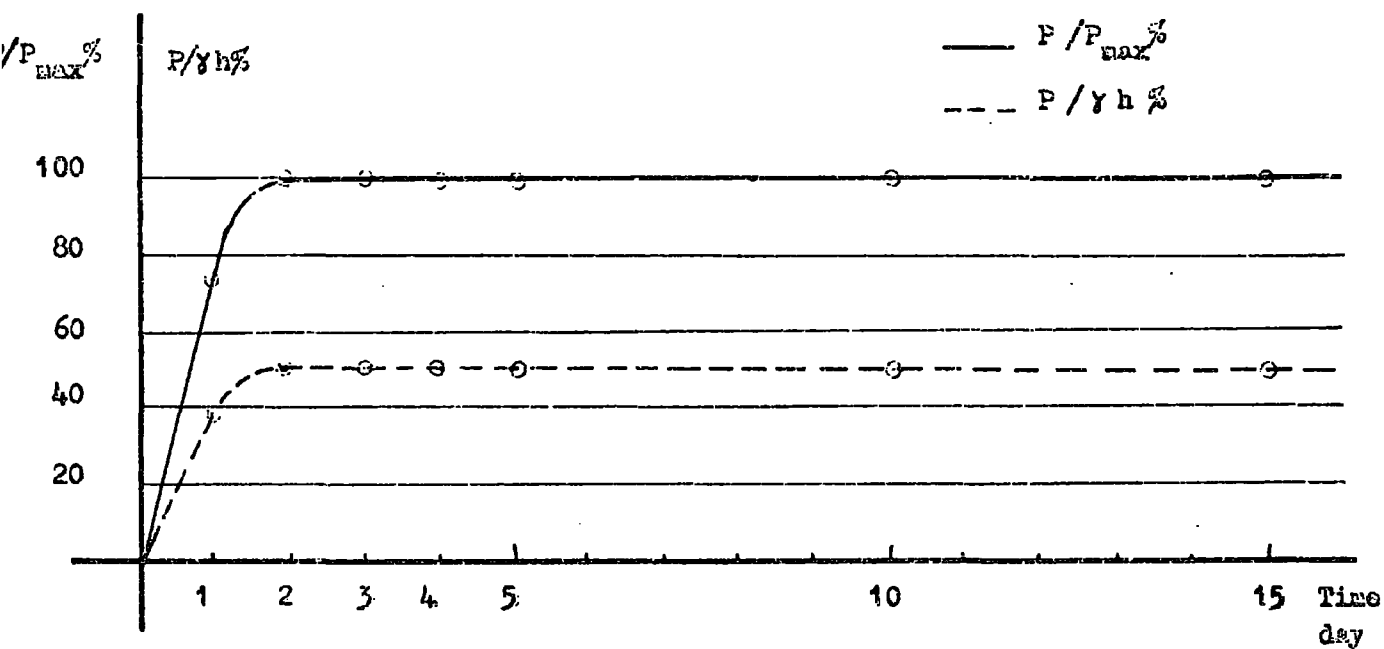


Figure 64.  $P/P_{max}$  % and  $P/\gamma h$  % - time curve of pressure cell No. 5

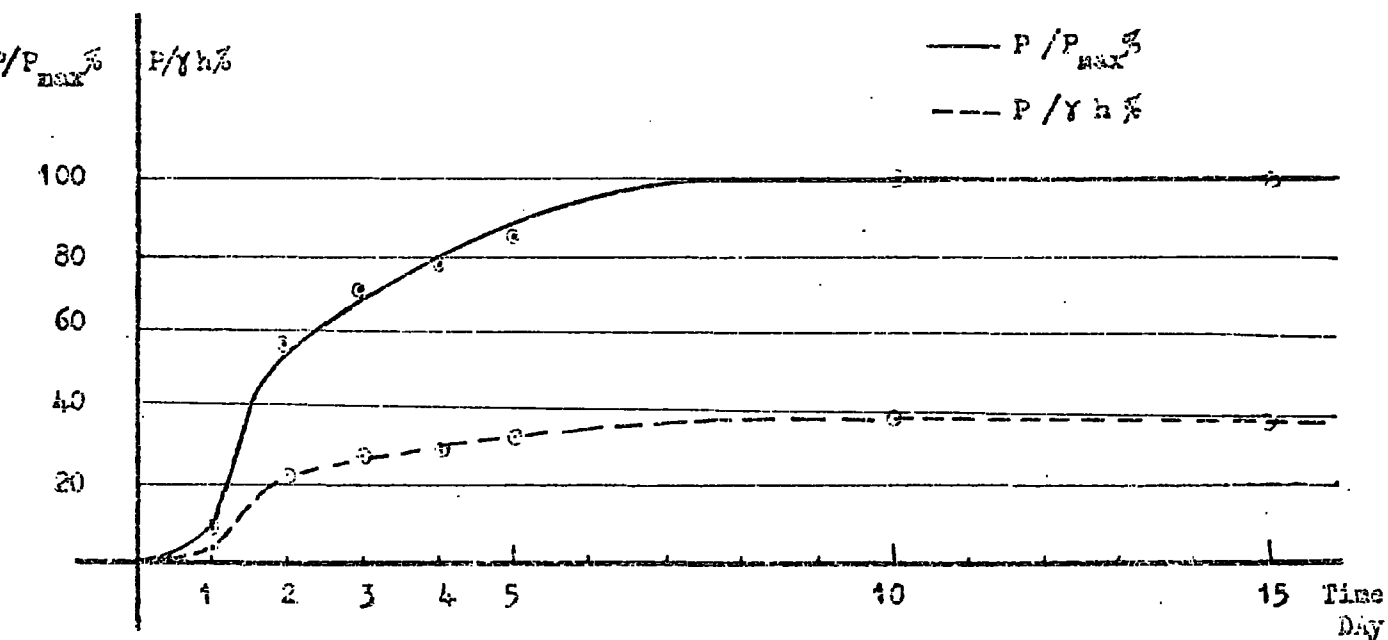


Figure 65.  $P/P_{max}$  % and  $P/\gamma h$  % - time curve of Pressure cell No. 4



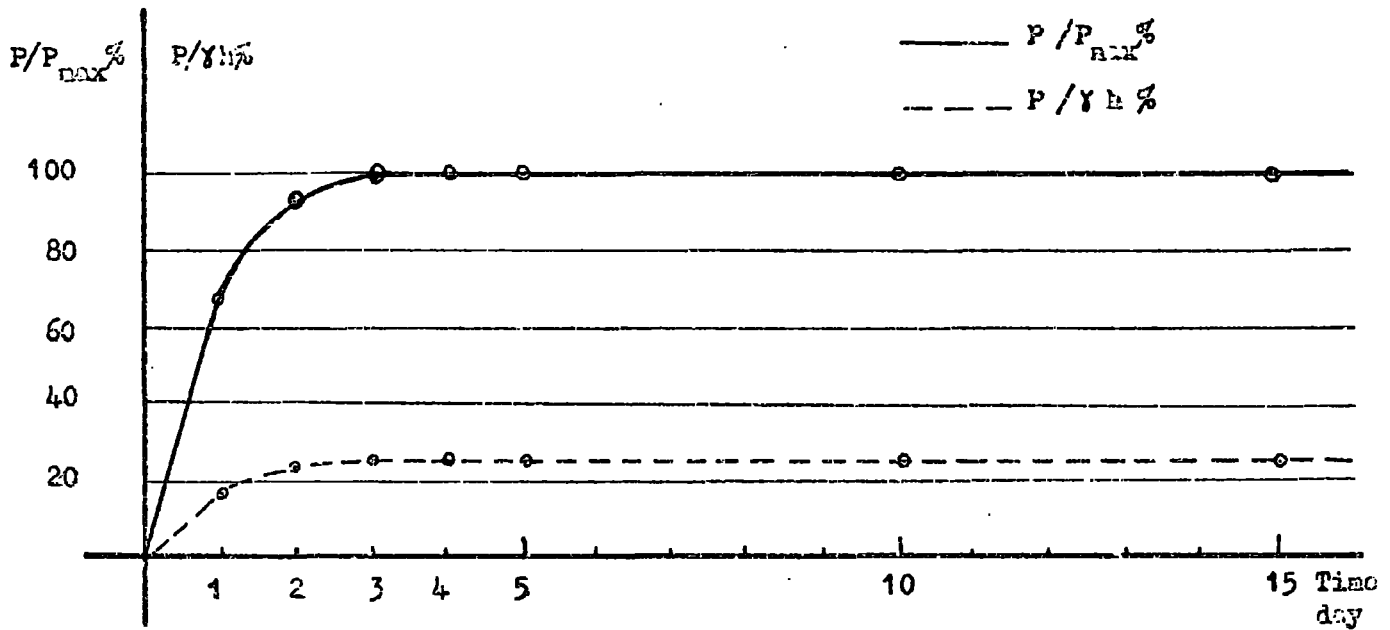


Figure 66  $P/P_{max} \%$  and  $P/\gamma h \%$  - time curve of pressure cell No. 5

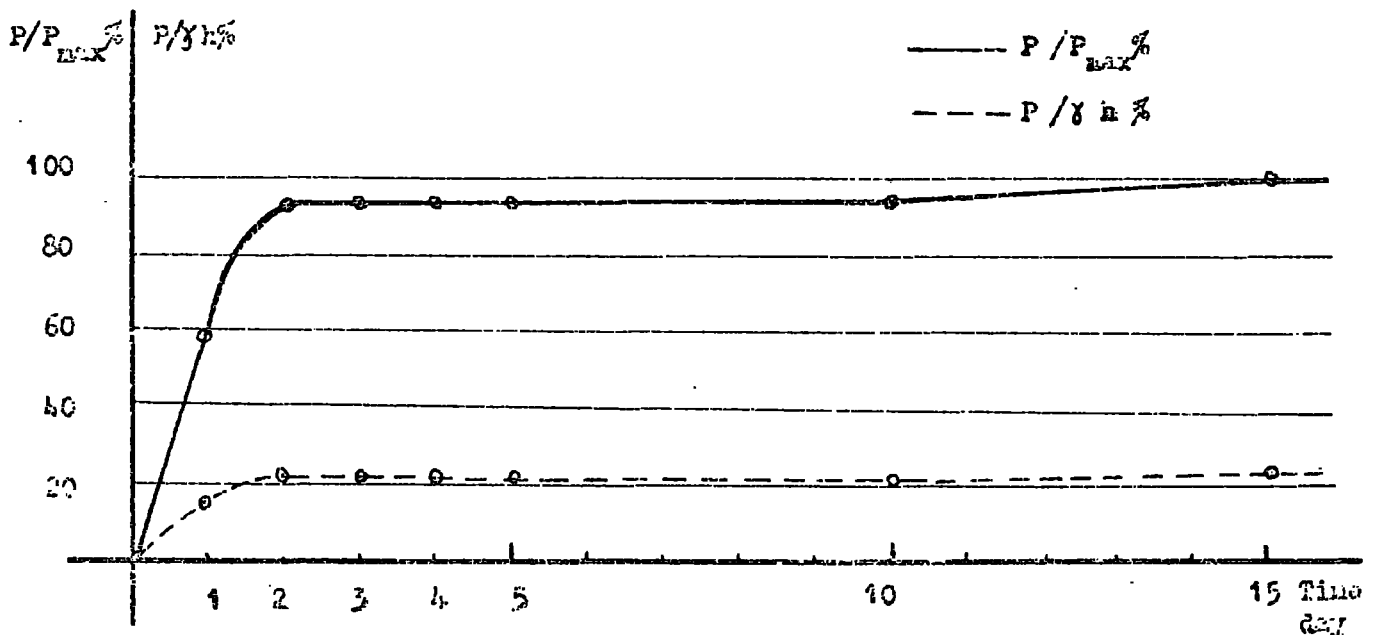


Figure 67  $P/P_{max} \%$  and  $P/\gamma h \%$  - time curve of pressure cell No. 6

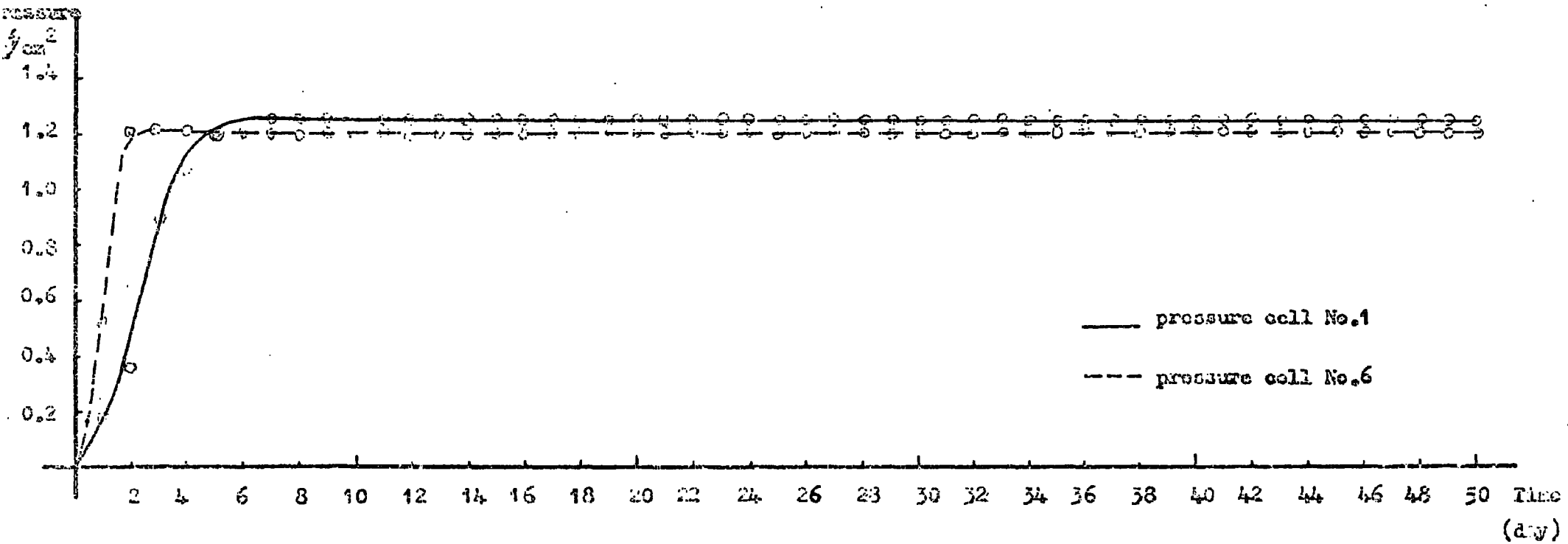


Figure 68 Pressure - time curve of the pressure cells No. 1 and 6. (second experiment)

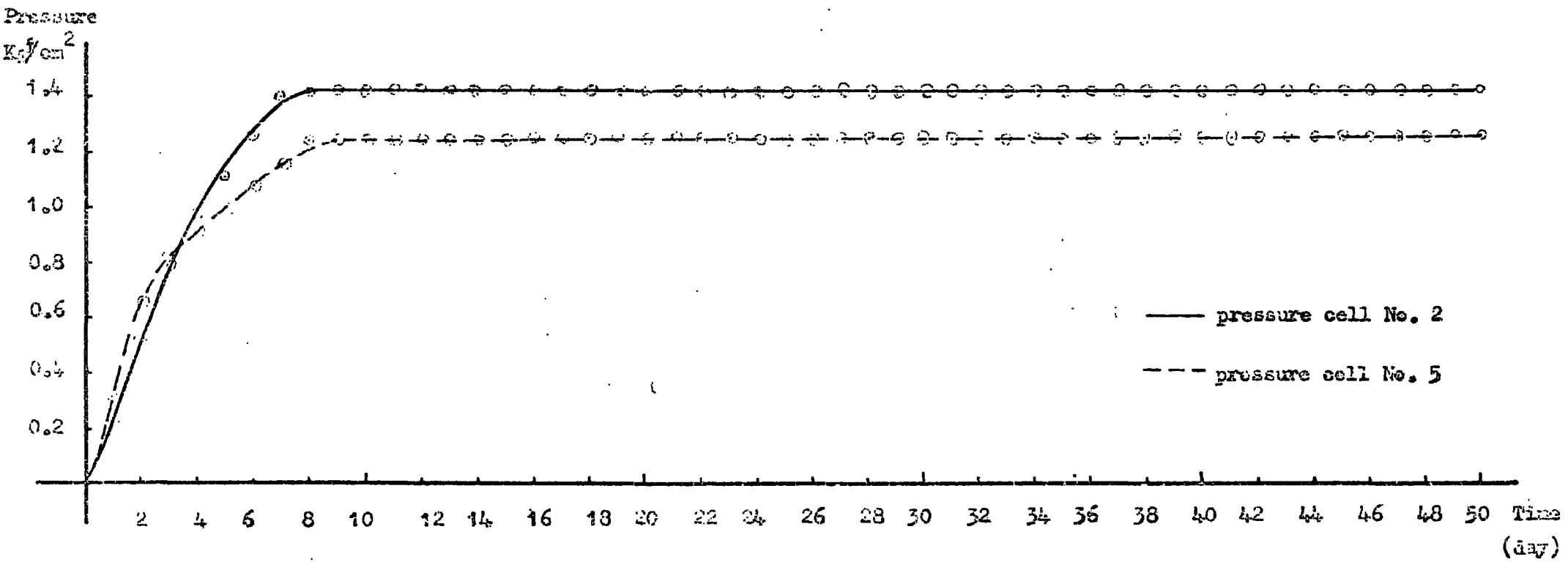


Figure 69 Pressure - time curve of the pressure cells No.2 and 5 (second experiment)

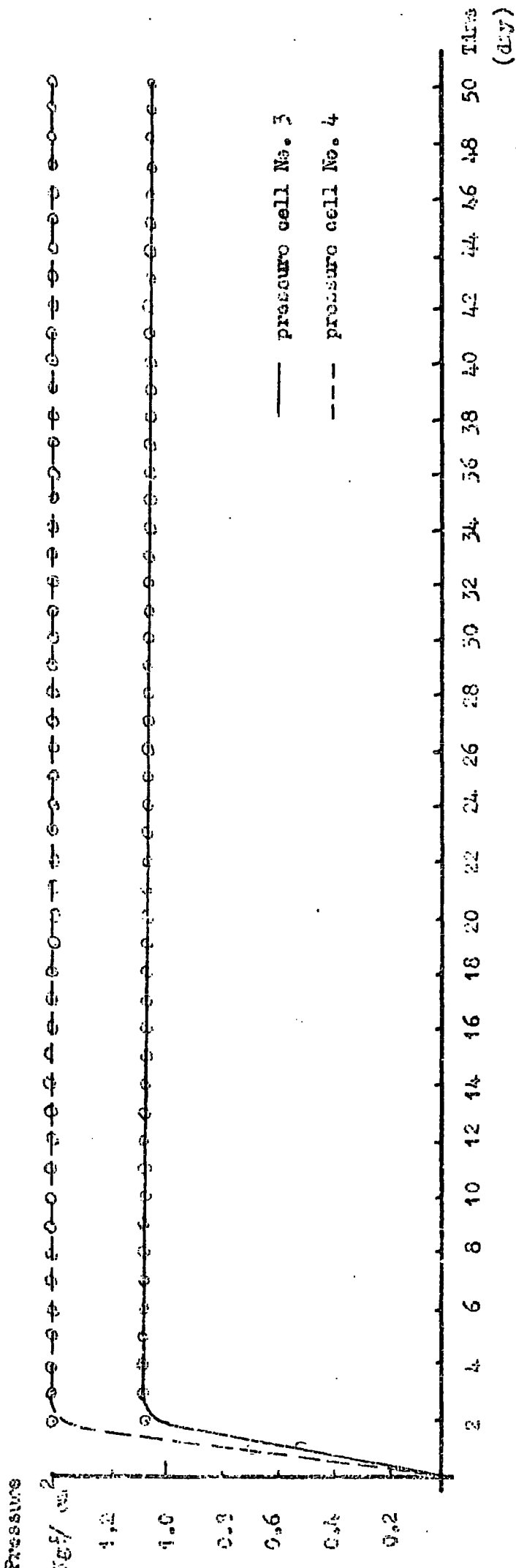


Figure 70 Pressure - time curve for the pressure cells No. 3 and 4  
 (second experiment)

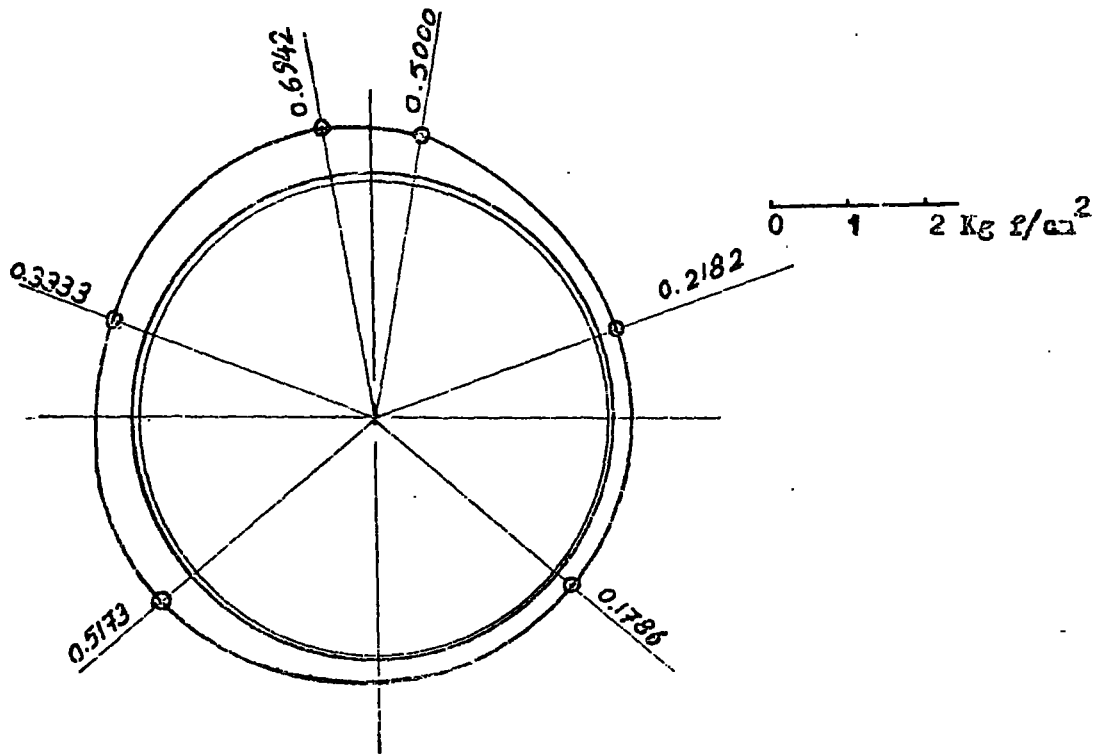


Figure 71 Pressure distribution around the tunnel lining one day after its construction (second experiment).

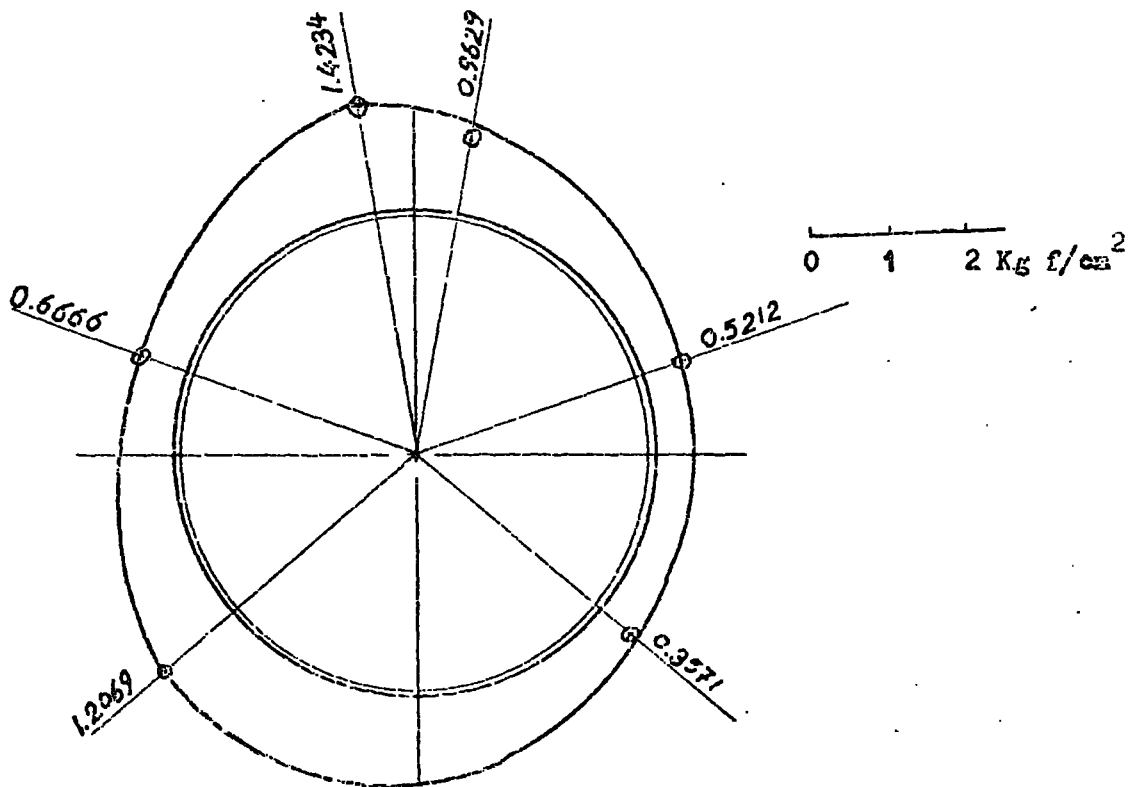


Figure 72 Pressure distribution around the tunnel lining two days after its construction (second experiment).

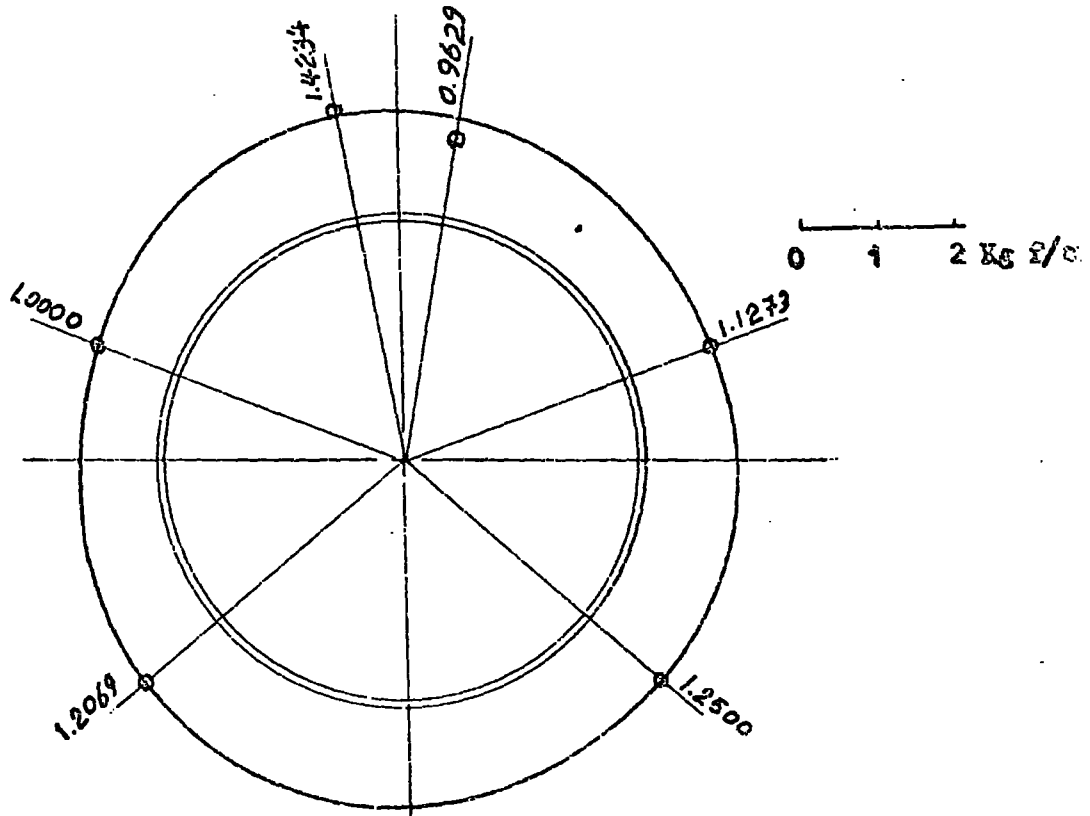


Figure 73 Pressure distribution around the tunnel lining five days after its construction (second experiment).

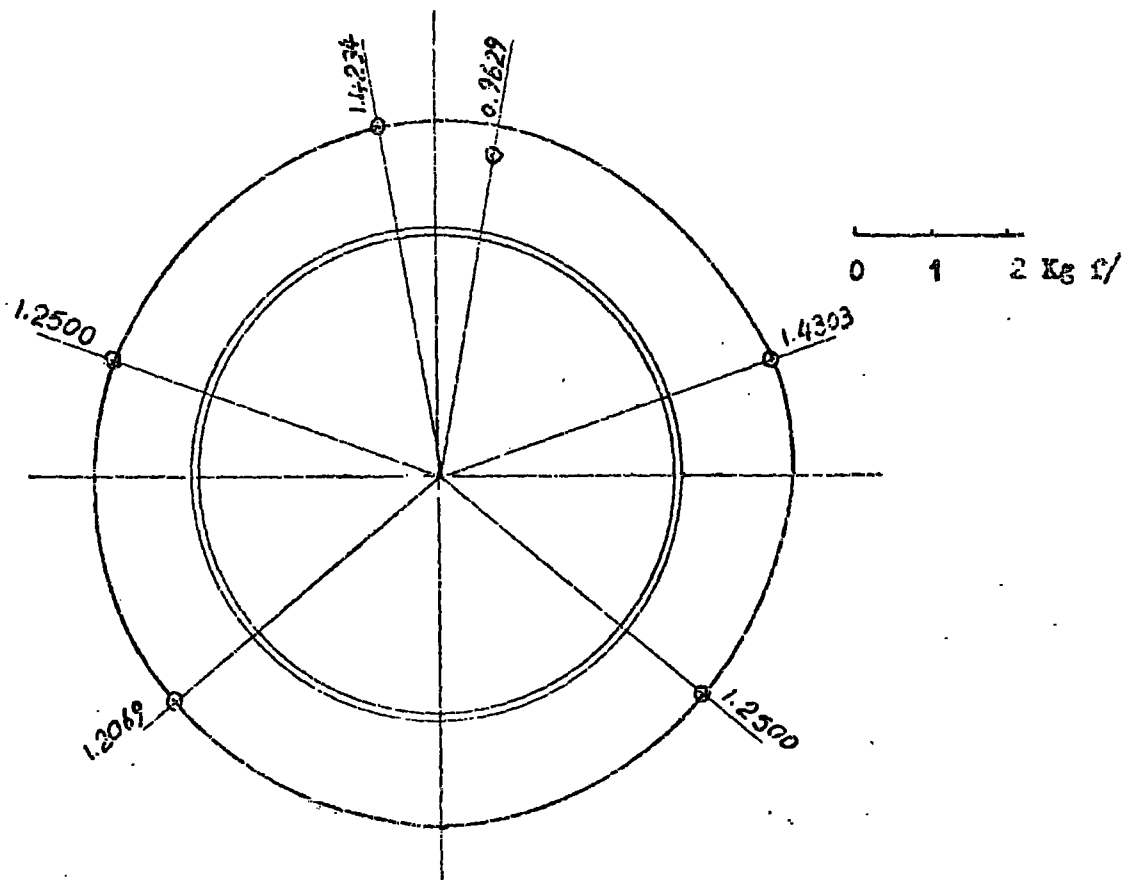


Figure 74 Final pressure distribution around the tunnelling (second experiment).

that the tunnel lining is ultimately subjected to a uniform hoop pressure.

$P/P_{\max}$  and  $P/\gamma h$  - time curves for the pressure cells used in the second experiment, are illustrated in the Figures 75 to 80. These Figures prove that the pressures around the tunnel lining reach their terminal values after a period of eight days of the lining erection in a closely similar manner to the pressure development in the first experiment.

#### 4.3 Analysis of the tunnel diameter measurements

The results of the field measurement of the changes in tunnel diameter are tabulated in Table 11. Figure 81 represents the primary and the final tunnel lining form, the final form being reached after 8 days following lining erection.

The development of lining deformation for the four measuring directions  $D_1$ ,  $D_2$ ,  $D_3$  and  $D_4$  is indicated in Figure 82. It will be noted that the maximum diametral change for the vertical diameter  $D_1$  was 1.30 mm, which is equivalent to 0.041%. and for the horizontal diameter  $D_2$  was 0.88 mm, which is equivalent to 0.027%. Diametral changes for the diameters  $D_3$  and  $D_4$  are practically negligible, as might be expected.

These very low values of deformation imply that the lining behaved essentially in an ideally rigid manner and for that the grout at the spring line was extremely effective in filling the overcut created by the pneumatic spades and in facilitating early mobilization of passive pressure. The deformation measurements therefore substantiate the arguments propounded earlier on the basis of the pressure cell readings.

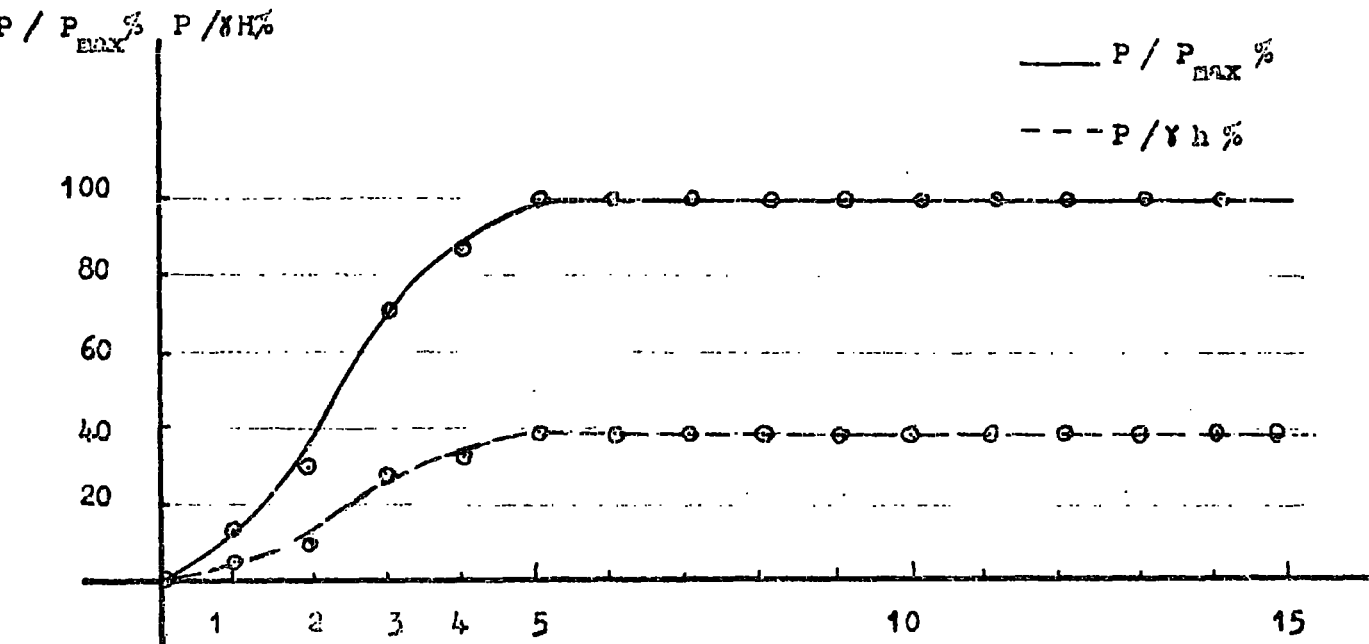


Figure 75  $P/P_{max}$  and  $P/Yh$  % - time curve of the pressure cell No.1  
(second experiment)

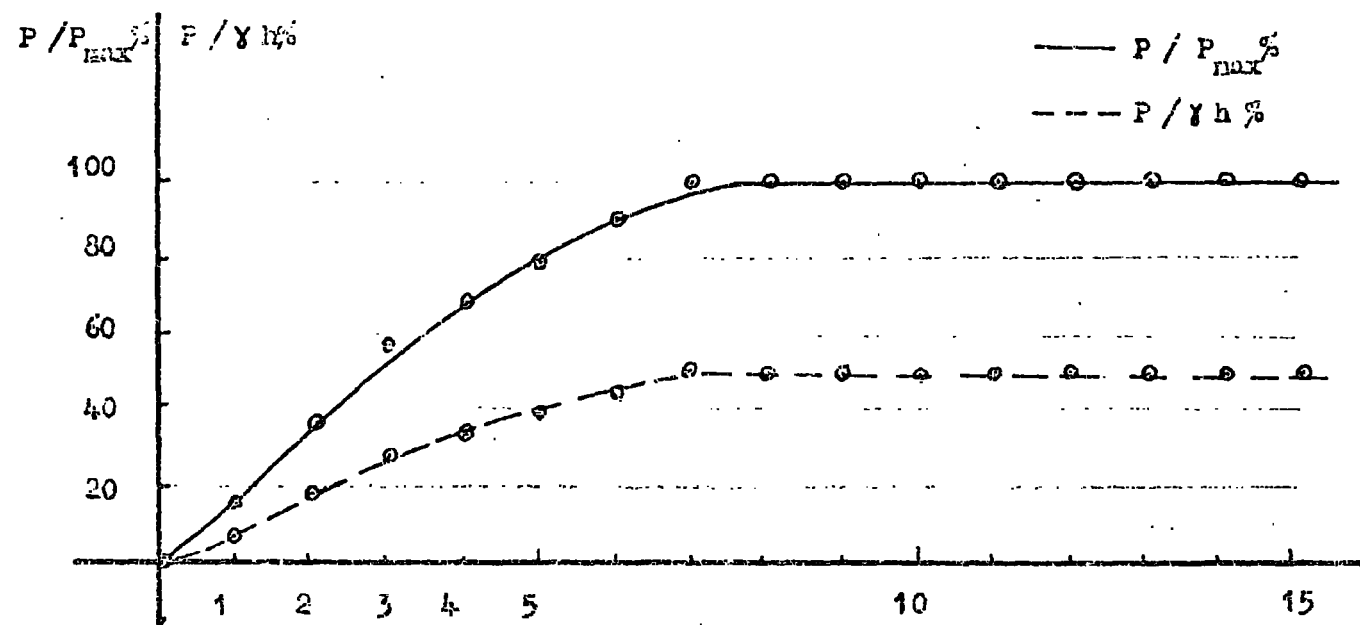


Figure 76  $P/P_{max}$  and  $P/Yh$  % - time curve of pressure cell No. 2

(second experiment)



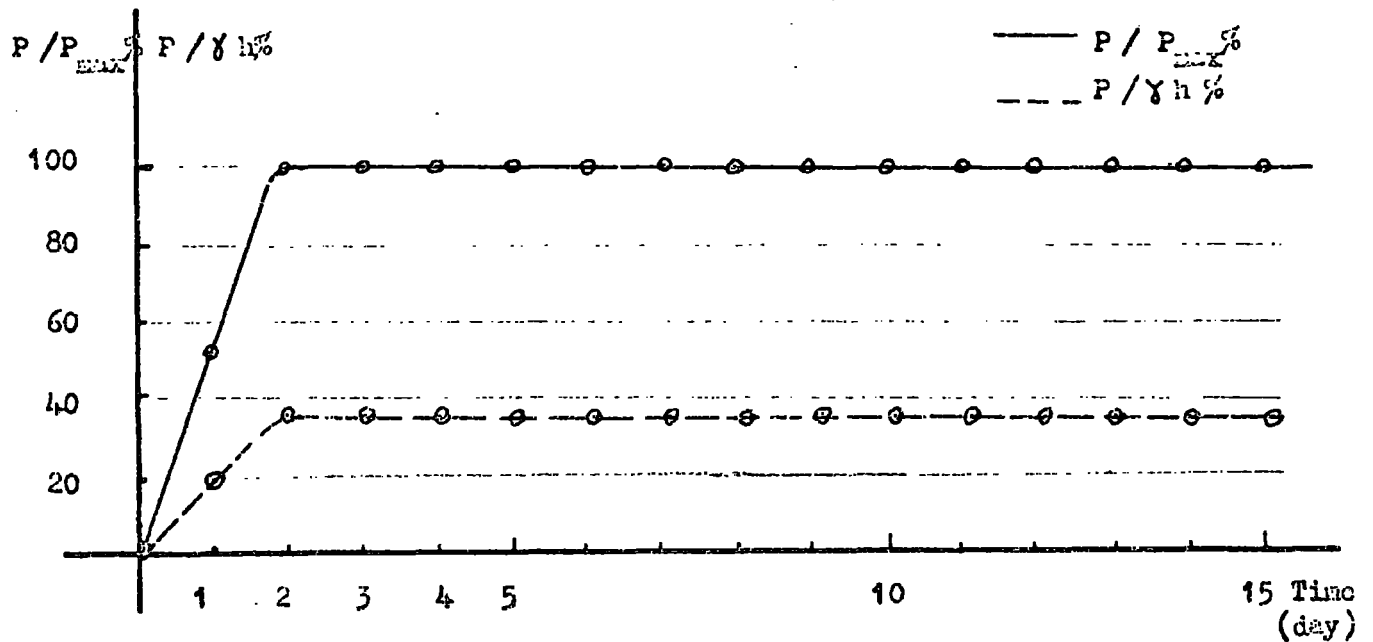


Figure 77  $P/P_{max}$  % and  $P/Y h$  % -time curve of pressure cell No. 3  
(second experiment)

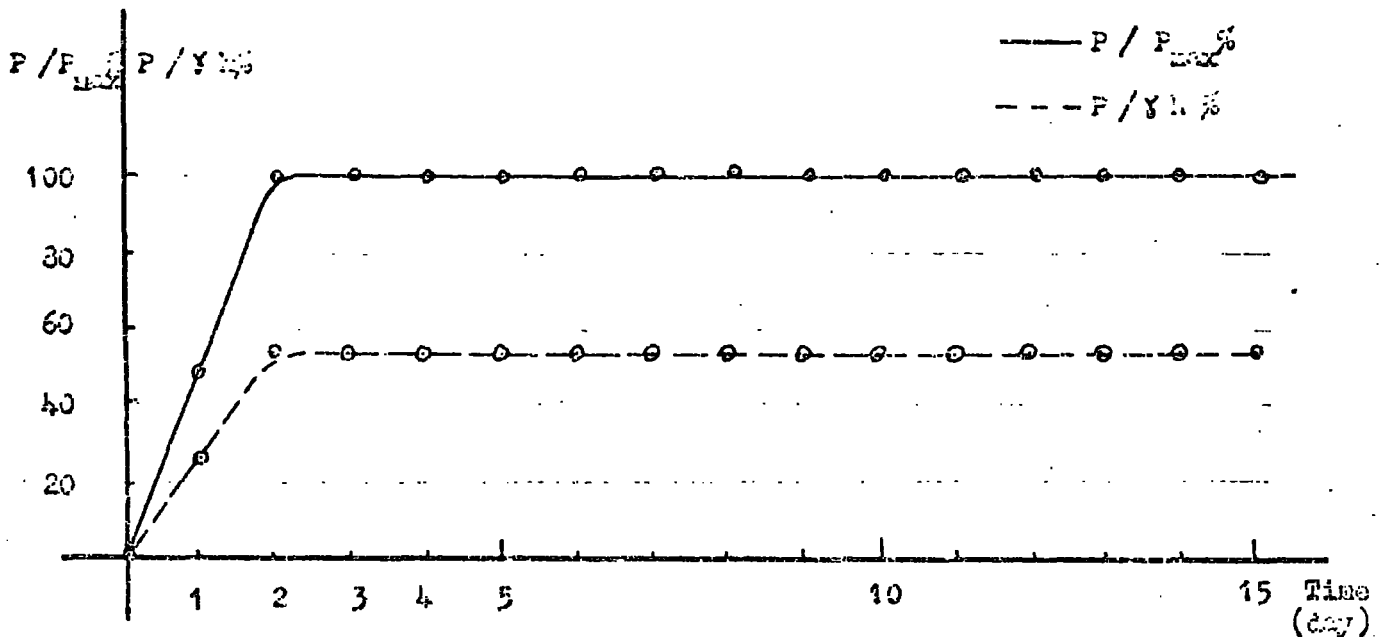


Figure 78  $P/P_{max}$  % and  $P/Y h$  % -time curve of pressure cell No. 4  
(second experiment)

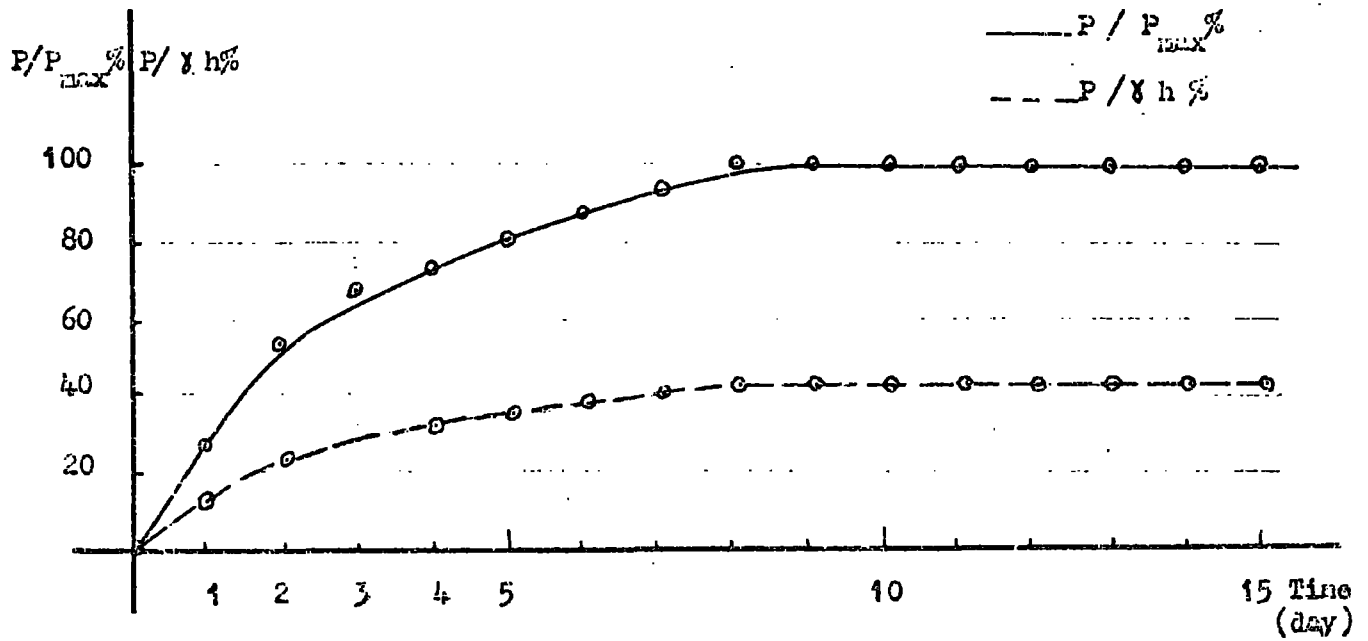


Figure 79  $P/P_{max} \%$  and  $P/\gamma h \%$  -time curve of pressure cell No. 5  
(second experiment)

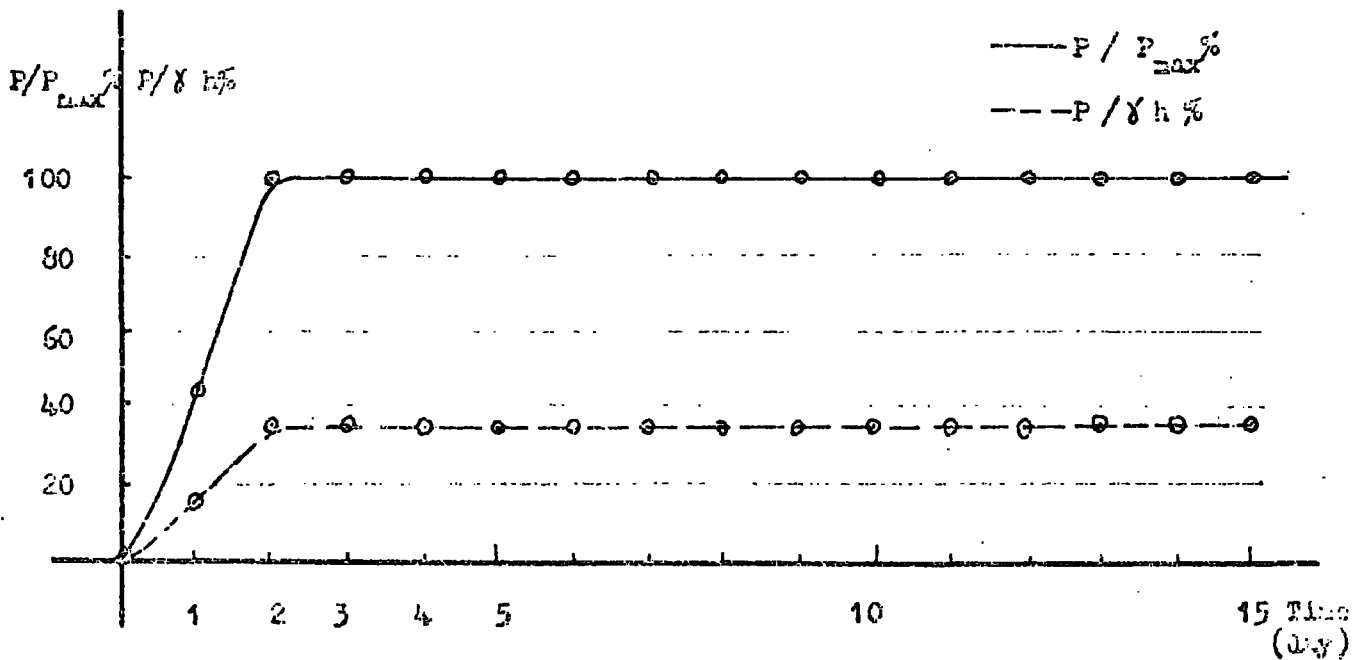


Figure 80  $P/P_{max} \%$  and  $P/\gamma h \%$  - time curve of pressure cell No. 6  
(second experiment)

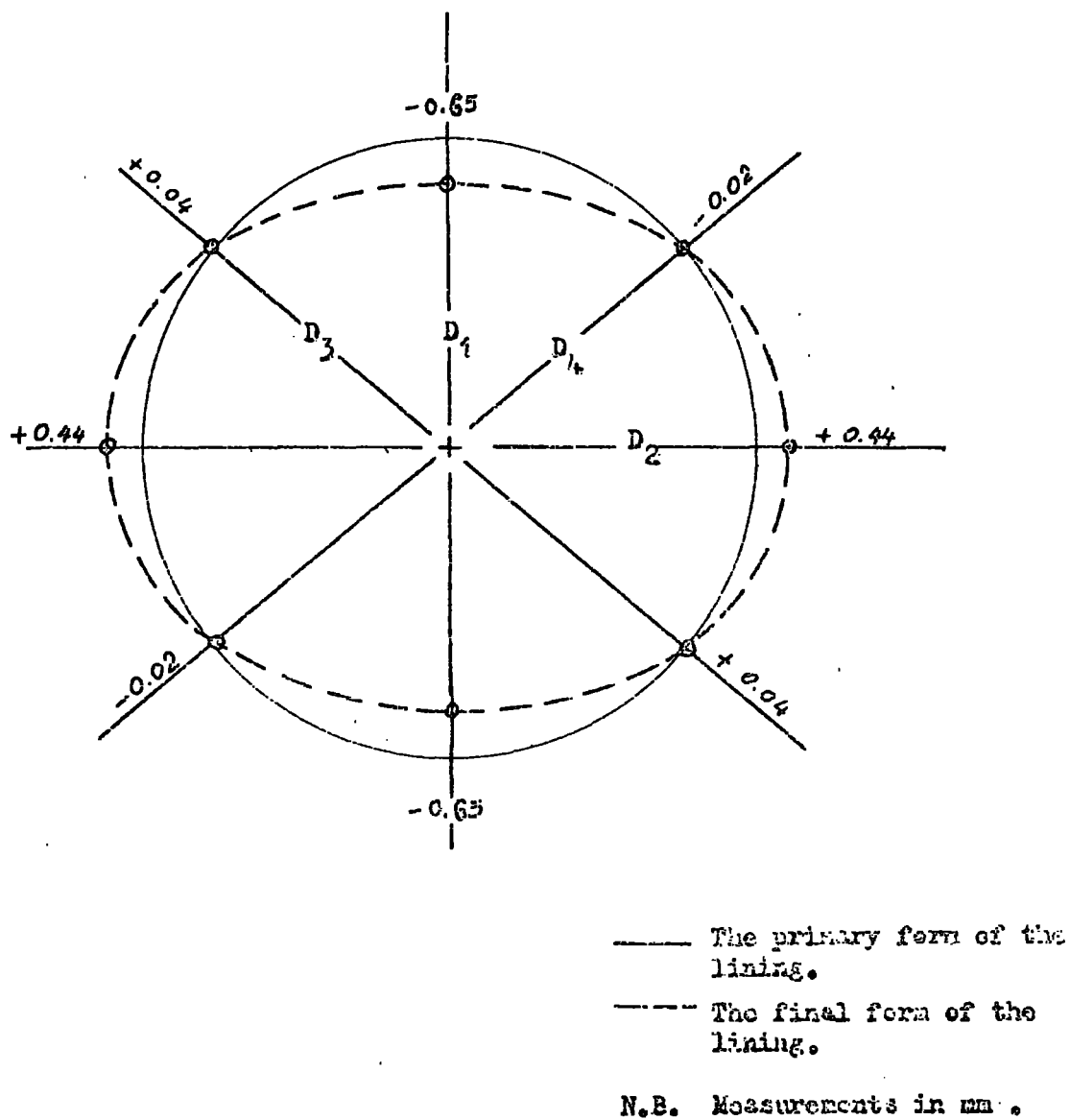


Figure 81 Final deformation of the tunnel lining .

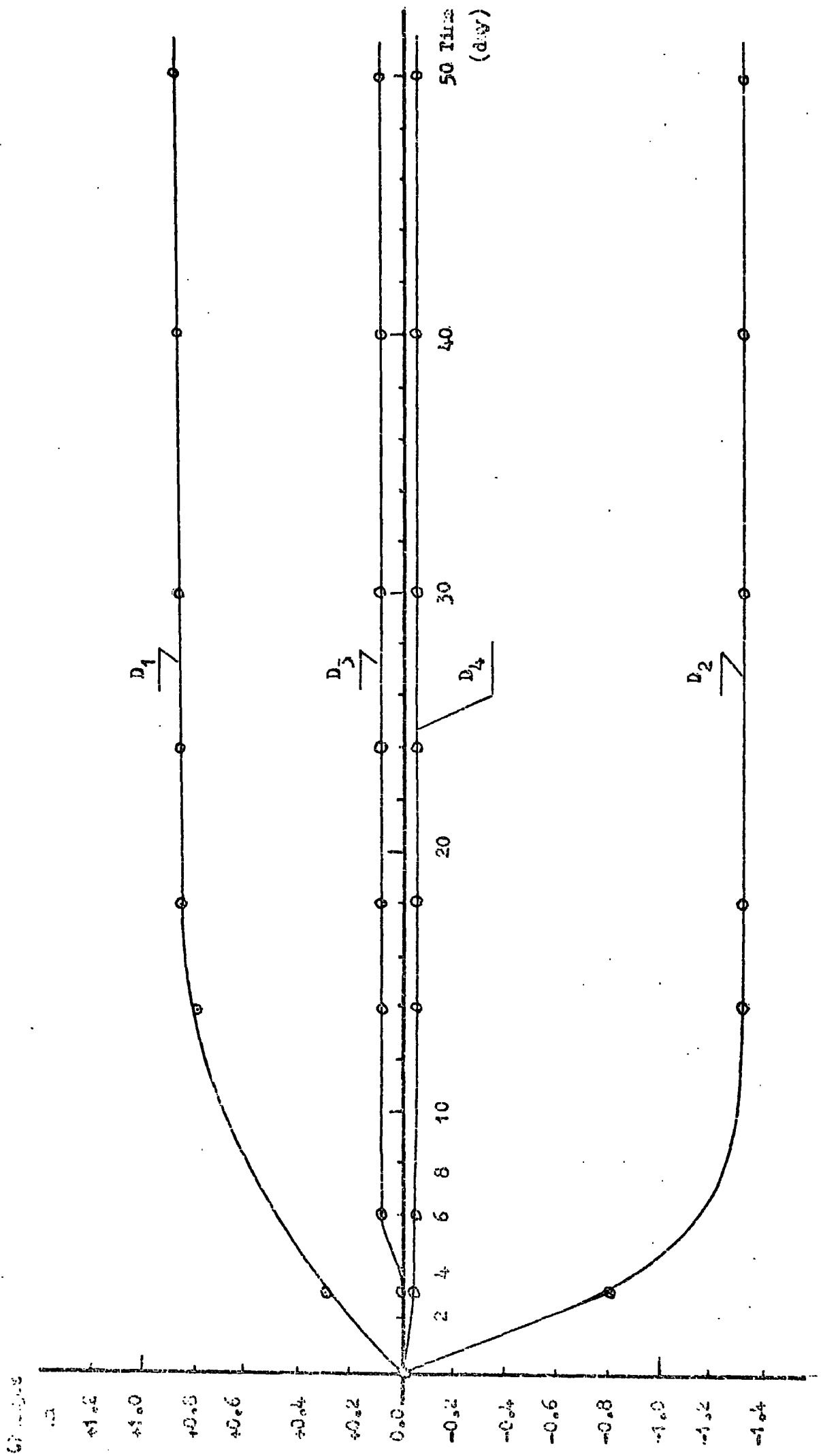


Figure 82 The changes of the tunnel diameter - time curves .

Diameter Time 'day'	D <sub>1</sub>	D <sub>2</sub>	D <sub>3</sub>	D <sub>4</sub>
0	± 0.00	± 0.00	± 0.00	± 0.00
3	+0.30	- 0.81	+ 0.00	- 0.04
6	+ 0.68	- 1.12	+0.10	- 0.08
14	+ 0.80	- 1.30	+ 0.09	- 0.05
18	+ 0.87	- 1.29	+ 0.09	- 0.03
24	+ 0.88	- 1.29	+ 0.09	- 0.03
30	+ 0.87	- 1.30	+ 0.08	- 0.04
40	+ 0.87	- 1.30	+ 0.08	- 0.04
50	+ 0.88	- 1.29	+ 0.08	- 0.04

Table 11 The changes in the tunnel diameter (mm).

#### 4.4 Application of tunnel-soil contact pressure theories to the tunnel situation currently considered

By applying Terzaghi's theory and Protodyakonov's theory (see Appendices A and B) to the present situation we have:

##### A) Terzaghi's theory

According to this theory, the vertical pressure of the tunnel crown ' $P_v$ ' is given by:

$$P_v = \frac{B(\gamma/2 - C/B)}{K \tan \phi} \left\{ 1 - \exp \left( -K \tan \phi \cdot \frac{2H}{B} \right) \right\} + q \exp \left( -K \tan \phi \cdot \frac{2H}{B} \right)$$

where

- $b$  = tunnel width
- $h_t$  = tunnel height
- $B = 2 \left[ b/2 + h_t \tan(45 - \phi/2) \right]$
- $\gamma$  = unit weight of the soil
- $\phi, C$  = soil shear strength parameters
- $q$  = superimposed load
- $H$  = tunnel cover depth
- $K$  = coefficient of earth pressure

For purely cohesive soils, the above equation is modified to the following form.

$$P_v = H (\gamma - \tau/B)$$

where  $\tau$  = the shear strength of soil.

Thus, in the cases in question,

##### a) First Experiment

$$H = 11.77 \text{ m}$$

$$\tau = 18 \text{ tf/m}^2$$

$$B = 9.60 \text{ m}$$

$$\gamma = 2.2550 \text{ t/m}^3$$

$$P_v = 11.77 \left( 2.255 - \frac{18.0}{9.60} \right)$$

$$\begin{aligned}
 &= 4.4726 \text{ tf/m}^2 \\
 &= 0.4473 \text{ kgf/cm}^2 \\
 &= 43.8667 \text{ kN/m}^2.
 \end{aligned}$$

b) Second Experiment

$$\begin{aligned}
 H &= 12.39 \text{ m} \\
 \tau &= 18 \text{ tf/m}^2 \\
 B &= 9.60 \text{ m} \\
 \gamma &= 2.2550 \text{ t/m}^3 \\
 P_v &= 12.39 \left( 2.255 - \frac{18.0}{9.60} \right) \\
 &= 4.7082 \text{ tf/m}^2 \\
 &= 0.4708 \text{ kgf/cm}^2 \\
 &= 46.1714 \text{ kN/m}^2.
 \end{aligned}$$

B) Protodyakonov's theory.

According to this theory, the vertical pressure at the tunnel crown ' $P_v$ ' is given by:

$$P_v = 2 \gamma b/3f$$

where

- $\gamma$  = the unit weight of the soil
- $b$  = half the tunnel width
- $f$  = strength factor suggested by Protodyakonov

Thus, in the case in question (the two field experiments)

$$\begin{aligned}
 P_v &= 2 \times 2.2550 \times 1.6/3 \times 1.5 \\
 &= 1.6036 \text{ tf/m}^2 \\
 &= 0.1604 \text{ kgf/cm}^2 \\
 &= 15.7304 \text{ kN/m}^2
 \end{aligned}$$

For comparison, the results of the applied theories and the field measurements are tabulated below.

Method Experiment	Field Measurement	Terzaghi's Theory	Protodyakonov's Theory
1st Experiment	1.298 kgf/cm <sup>2</sup>	0.4473 kgf/cm <sup>2</sup>	0.1604 kgf/cm <sup>2</sup>
2nd Experiment	1.4234 kgf/cm <sup>2</sup>	0.4708 kgf/cm <sup>2</sup>	0.1604 kgf/cm <sup>2</sup>



#### 4.5 Notable case histories of tunnel-soil contact pressure measurements:

There are a number of case histories relating to in-tunnel experimentation. From some of the most notable of these the following are chosen to illustrate the type of results that are obtained.

##### i) Shield tunnels of the Chicago Subway (Terzaghi, 1942)

A long term experiment over a period of ten years was carried out in order to measure the earth movement resulting from the driving of two adjacent tunnels in Chicago Clay and to gather information on both the pressure distribution developed around the welded steel tunnel liner and the tunnel lining deformation.

Each of the two tunnels was 25 ft outer diameter and the invert of each was located at a depth of about 50 ft below the street level. The space between the tunnels at the spring line level was about 2ft 9in. Two different methods were used for the construction of the tunnels; the liner plate and the shield method. North of Chicago River, where the clay is stiff enough to withstand the loads imposed upon it by the footings, the liner plate method was used.

The more costly shield method was used south of the river, where the clay is too soft to withstand the expected load. These experiments resulted in the following conclusions:

1. Different sizes of opening in the shield face and a variable rate of shoving were used during the tunnel construction, and because of the presence of a stiff crust of clay located about midway between the tunnel crown and the surface of the street overhead, neither the size of the

opening nor the rate of shoving had a significant effect on the surface heave which took place due to the passage of the shield.

2. The heave that occurred due to the passage of the first and second shield was generally followed by a progressive settlement at a decreasing rate, and this lasted for about one year after the passage of the shield due to the consolidation of the remoulded clay around the tunnel.

3. Measurement of the lining-soil interaction pressure showed that the final equilibrium in the soil did not occur until about five years after the lining construction. Figure 83 represents the pressure-time curve at the crown, invert and the spring line of the lining.

4. Measurement of the tunnel lining deformation indicated a slight change in the shape of the lining up to about one year after erection. Figure 84 represents the deformation-time curve and Figure 85 illustrates the shape of the ring after 47 days and after 342 days.

ii) The development of earth loading and deformation in tunnel linings in London Clay (after Ward, 1965):

A long term experiment over a period of six years was performed in order to measure the lining-soil interaction pressures and the deformation of tunnel linings in London Clay.

The experiment was carried out at two sites for three different types of tunnel lining: the particulars of the linings are tabulated in Table 12 and sections through the segments are illustrated in Figures 87 and 90.

The changes in the horizontal and vertical tunnel diameter for the three types are illustrated in Figures 86 and 89, and the Pressure-Time curves are illustrated in Figures 88 and 91.

Pressure  
psi

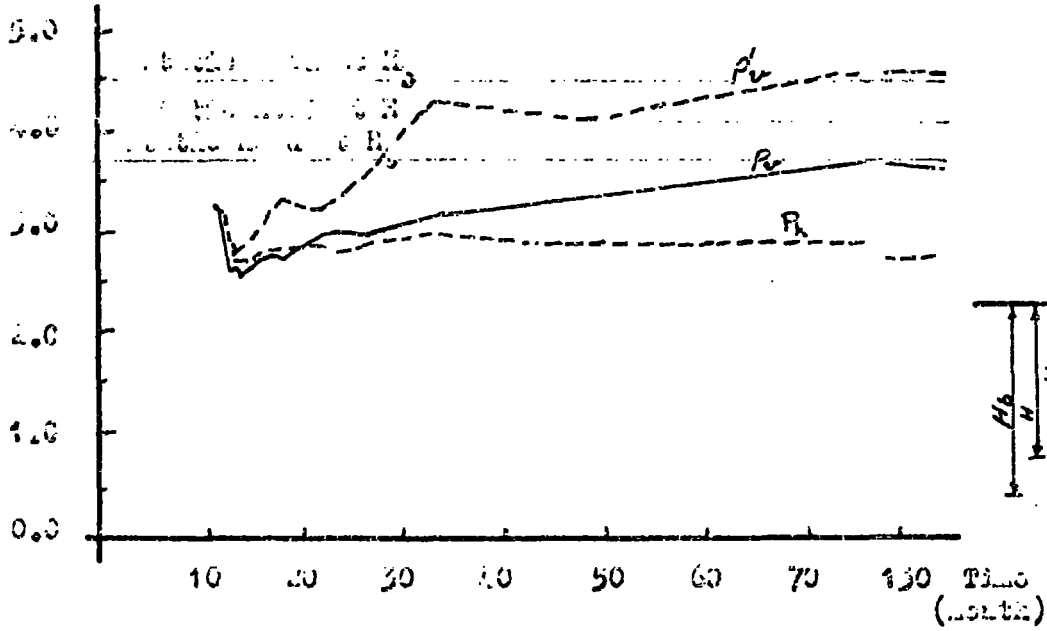
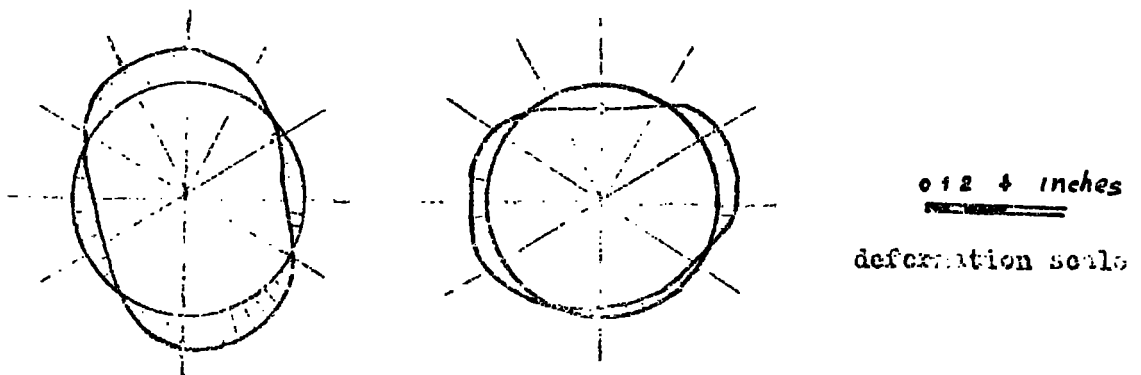


Figure 83 Pressure-time curve of a tunnel in Chicago plastic clay



Figure 84 Deformation-time curve of the tunnel lining (Chicago - clay)



of Chicago plastic clay

of Chicago plastic clay

Figure 85 Deformation of the tunnel lining (Chicago - clay)

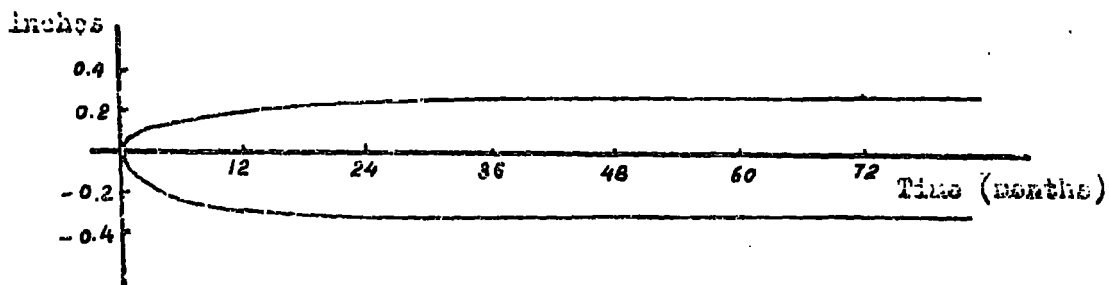


Figure 86 The changes in the horizontal and vertical tunnel diameter at site 'B' .

Figure 87

section through the tunnel linings at site 'B'

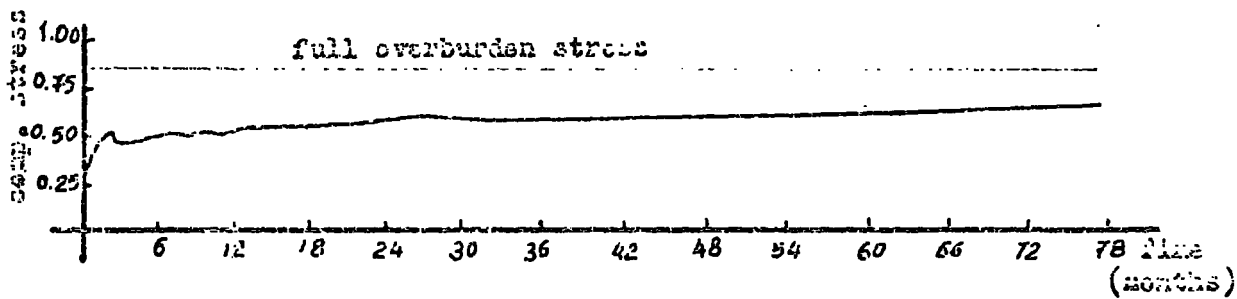
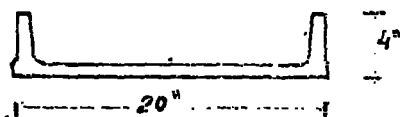


Figure 88 Stress - time curve at site 'B' .

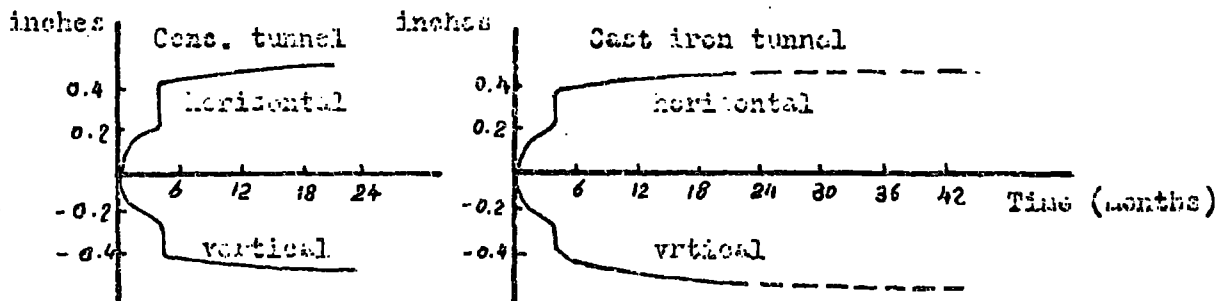


Figure 89 The changes in the horizontal and vertical tunnel diameter at site 'A' .

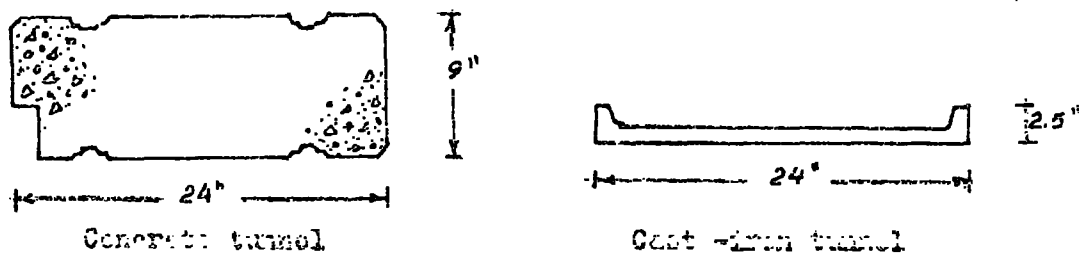


Figure 90 Sections through the tunnel linings at site 'A' .

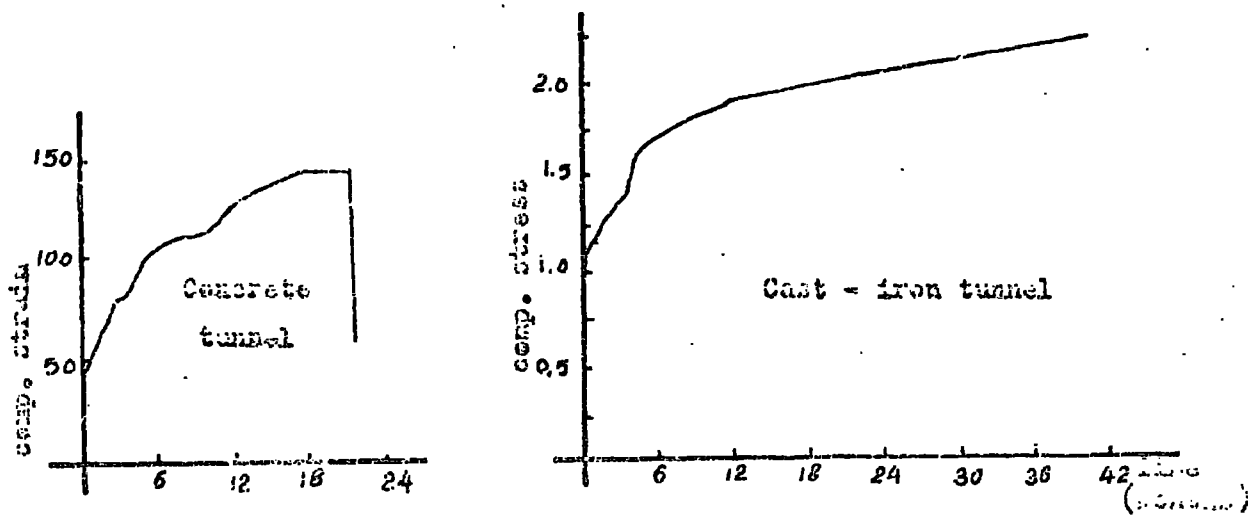


Figure 91 Stress - time curve at site 'A' .

Site	Depth	Internal diameter ft-in.	Material	Segments in one ring	Sectional area of Segment	Longitudinal joints.	Fitting to Clay
A	79	12-8	cast iron	6	27	Knuckle	jacked
	85	12-6	concrete	14	209	Curved butt	wedges
B	55	7-0	cast iron	6	21	Butt & bolted	grouted

Table 12 Particulars of tunnel-linings

The measurements of the deformations of each type of lining show a decrease in the vertical diameter and an increase in the horizontal diameter. The deformations developed rapidly in the first few months after construction, but continued at a slow rate for at least six years.

The maximum diametral changes took place along the vertical and horizontal diameters, and at  $45^{\circ}$  to these directions the changes were negligible. For the concrete lining the vertical and horizontal changes are fairly equal, but for the cast-iron lining the increase in the horizontal diameter is less than the decrease in the vertical diameter.

Measurements of the circumferential pressure around the linings show that the distributions of the pressures were fairly uniform. At site A, for cast-iron linings, the pressure approached the value of the full overburden pressure  $\frac{3}{2}$  years following construction, and for concrete linings it reached 65% of the overburden pressure after 21 months. At site B, the pressure reached 75% of the overburden pressure after 6 years.

iii) Observations on a tunnel driven in blue London Clay.  
(Skempton, 1943)

This experiment was performed in a tunnel driven in blue London Clay. The tunnel lining was a cast-iron type, and of the cross section as shown in Figure 93. The tunnel was 12 ft internal diameter, and its axis level was 109 ft below the street level. The experiment was concerned only with the measurement of the stresses developed in the lining by the earth pressure around the tunnel. Two sets of instruments, each consisting of three Whittemore strain-gauges, were established in the positions shown in Figure 93. The locations of the observation points were 2 feet to the right and the left of the crown. The measurements began ten days after an adjacent tunnel - 5 feet between the external diameters - had been driven past the ring in question.

The experiment results in the conclusion that the clay was sufficiently plastic to exert its full weight on the tunnel, and a two weeks time period being required for the full pressure to be developed. Figure 92 illustrates the pressure-time curve.

iv) Summary

The results of the experiments mentioned before are listed together with the results of the field experiment in question in Table 13.

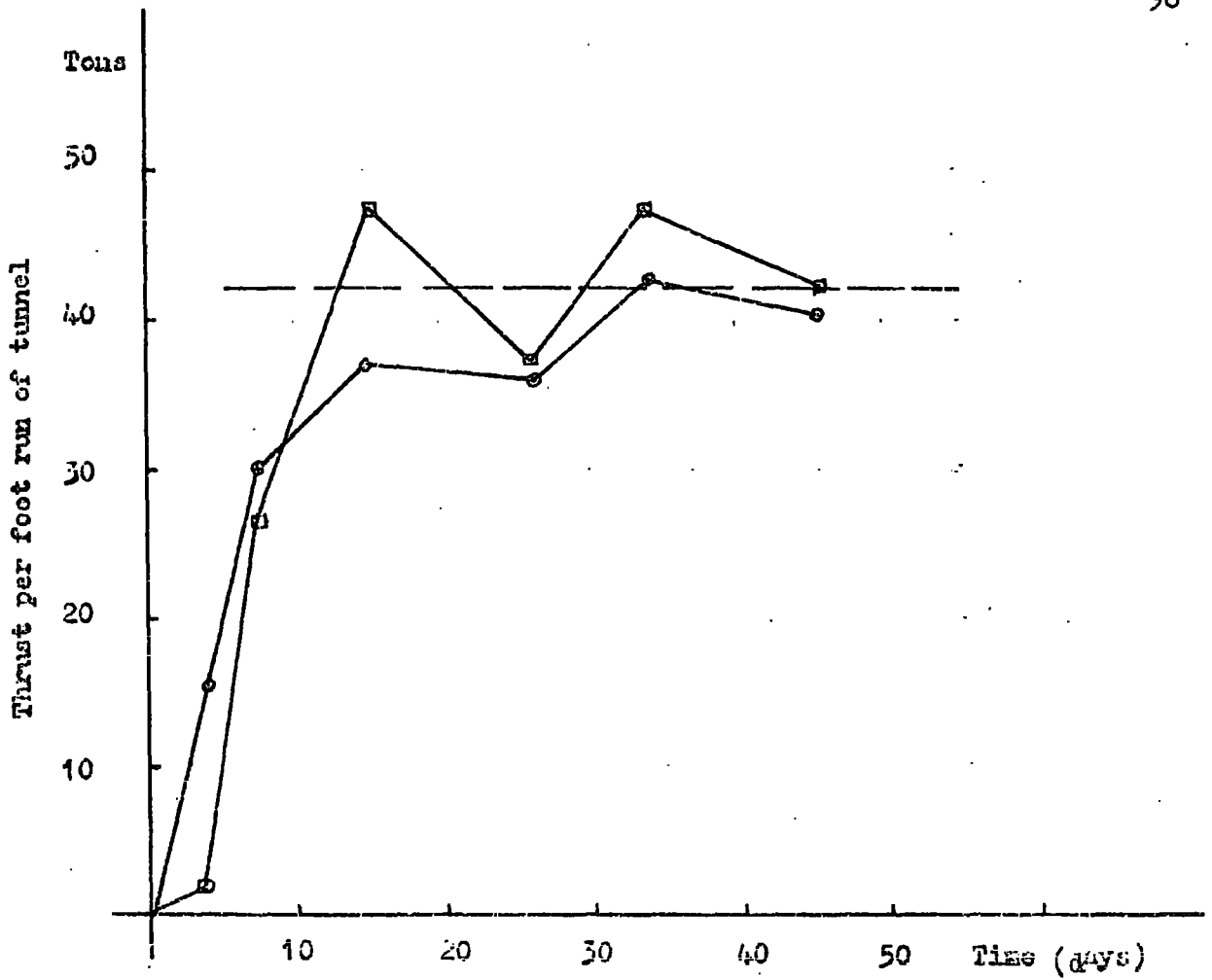


Figure 92 Thrust - time curve for the two observation points.

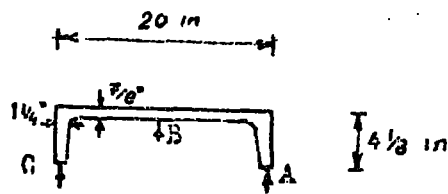


Figure 93 Section through the tunnel lining .



Table 13      Comparison between the Experiment-results.

Experiments	Soil	Tunnel depth (crown) m	Internal diameter m	No. of segments in the ring.	Material	Time required for pressure development	Measured Pressure Overburden Pressure %	Notes
Terzaghi (1942)	Chicago Clay	7.50	7.50	6	welded steel	5 years	100%	
Ward (1965)	London Clay	1- 24.095	3.889	6	cast-iron	3½ years	100%	at spring level
		2- 25.925	3.812	14	concrete	21 months	65%	"
		3- 16.775	2.135	6	cast-iron	6 years	75%	"
Skempton (1943)	Blue London Clay	31.00	3.66	6	cast-iron	14 days	100%	
The experiment in question	Laminated clay and stiff stony clay	11.77	2.90	6	concrete	8 days	51%	at the crown
		12.39	2.90	6	concrete	8 days	52%	at the crown

## CHAPTER 5

### Theoretical study of the effect of lining-soil stiffness on the distribution of thrust and bending moment in the lining.

#### 5.1 Introduction.

One of the most interesting problems that faces structural engineers during the design of tunnels is the estimation of the magnitude and distribution of the total pressure - that is, the effective earth pressure and water pressure - to which these tunnels will be subjected after construction.

The magnitude of the earth pressure is in general independent of the stiffness and time of installation of the tunnel lining; only the distribution of the earth pressure is directly influenced by the lining stiffness. Accordingly, the magnitude and the distribution of thrust and bending moment throughout the lining are directly affected by the stiffness of the lining relative to that of the surrounding soil.

The tunnel linings can be classified according to their relative stiffness into three types. These are: essentially rigid, essentially flexible, and semi-flexible or semi-rigid linings. Each type will be separately discussed subsequently.

#### 5.2 Rigid lining.

The lining is said to be rigid if it deflects insignificantly under the effect of the outer soil pressure, that is, there is negligible soil-lining interaction. In this case the lining is considered to be subjected

to the earth pressures distribution as shown in Figure 94.

According to this pressure diagram, the maximum bending moment 'M' and the thrust 'T' in the tunnel-lining are given by (Peck, 1972):

$$M = \frac{1}{4} \gamma H (K_0 - 1) R^2,$$

$$T(\text{spring line}) = \gamma H R,$$

$$\text{and } T(\text{invert \& crown}) = K_0 \gamma H R.$$

### 5.3 Flexible Lining.

The lining is considered to be flexible if it fully interacts with the surrounding soil in such a way that the final pressure distribution acting upon the lining is nearly uniform.

In this case the lining must be designed to withstand the thrust resulting from the outer pressure together with the bending moments resulting from the lining deformation, which latter can be estimated from experience (usually in the range of  $\frac{1}{2}\%$ ). The structural section of the lining must be checked against buckling, and this can be attained, in the case of soft clays, by ensuring that the overburden pressure  $\gamma H$  is less than  $3 EI/R^3$ , where,

E = Young's modulus of the lining material,

I = moment of the lining-structural section,

and R = mean radius of the lining.

### 5.4 Semi-flexible or semi-rigid lining.

The lining is known as a semi-flexible or semi-rigid lining if it has an intermediate flexibility compared with the two earlier-discussed extremes (the flexible and the rigid lining).



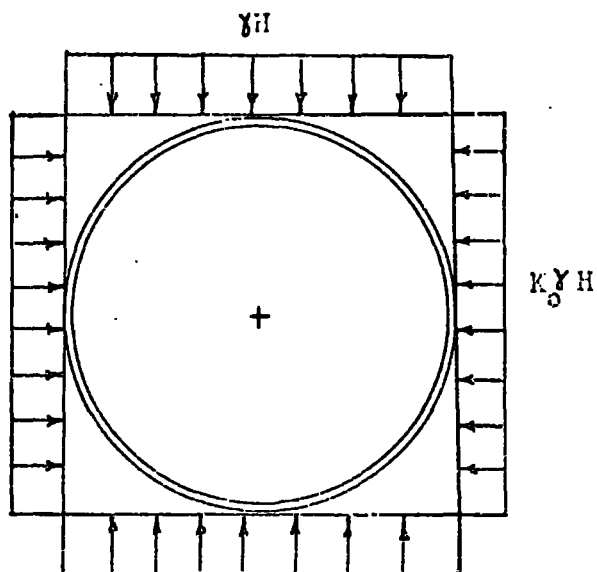


Figure 94. Pressure distribution on a rigid lining.

In this study, two quantitative methods to determine the relative flexibility of the tunnel lining of intermediate rigidity, as suggested by Burns and Richard (1964) and Peck (1972), are presented.

#### 5.4.1 The method suggested by Burns and Richard (1964).

In this method the tunnel-soil combination is considered as an elastic cylindrical shell embedded in an elastic medium. A structural analysis was made for the suggested system. Figure 95 illustrates the straining actions imposed upon the shell and upon the medium. In this analysis, the effect of a surface over-imposed load P only is considered. The analysis is applicable only to deeply buried conduits since the over-imposed load is considered to be acting at infinity in the derivation.

According to this method, any shell medium combination could be identified by the following parameters:

##### i) for the medium:

a) the constrain modulus  $M = \frac{E'(1 - \nu')}{(1 + \nu')(1 - 2\nu')}$  ;

b) the lateral stress ratio  $K = \frac{\nu'}{1 - \nu'}$  ;

##### ii) for the shell:

a) the radius R;

b) the circumferential extensional stiffness/unit length EA;

c) the circumferential bending stiffness/unit length EI.

In these expressions,  $E'$  is the modulus of elasticity and  $\nu'$  is the Poisson's ratio of the medium,  $E$  is the modulus of elasticity for the shell and  $A, I$  are the area and the moment of inertia of the shell section per unit length respectively.

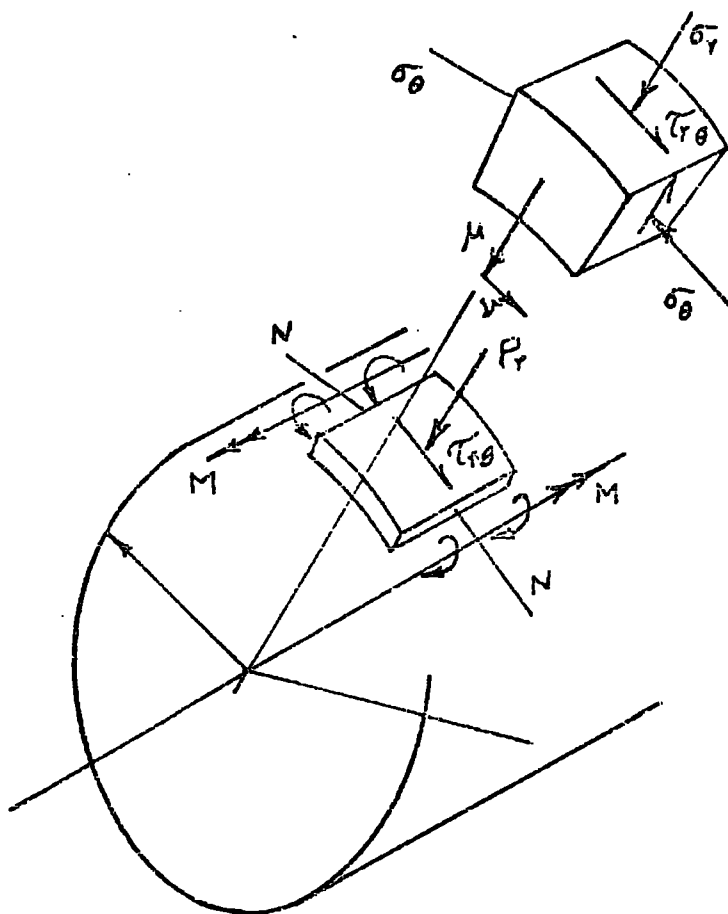


Figure 95 Straining actions diagram .

From these parameters, the following non-dimensionalized parameters and non-dimensionalized constants may be found:

i) The non-dimensionalized parameters:

$$a) \quad B_1 = \frac{1}{2}(1 + K) = \frac{1}{2} \left( \frac{1}{1 - \nu'} \right)$$

$$b) \quad B_2 = \frac{1}{2}(1 - K) = \frac{1}{2} \left( \frac{1 - 2\nu'}{1 - \nu'} \right)$$

$$c) \quad \text{The compressibility ratio } C = (1 + K) \frac{M R}{E A}$$

$$d) \quad \text{The flexibility ratio } F = (1 - K) \frac{M R^3}{6 E I}$$

ii) The non-dimensionalized constants:

$$a) \quad a = (C - 1)/(C + B_1/B_2)$$

$$b) \quad a' = (2F - 1 + 1/B_1)/(2F - 1 + 3B_1)$$

$$c) \quad a'' = (2F - 1)/(2F - 1 + 3/B_1)$$

The structural analysis showed that the stress distribution and displacements throughout the system are influenced by the following governing parameters:

i) The circumferential extensional flexibility of the medium relative to that of the shell (compressibility ratio, C).

ii) The circumferential bending flexibility of the medium relative to that of the shell (flexibility ratio, F).

iii) The tangential slippage of the shell relative to the medium at the shell-medium interface.

Two conditions were considered in the analysis: the full slippage and non-slippage condition. Since the shear stresses at the shell-medium interface (for most of the cases) are relatively high, the case of full slippage only will be considered.

According to the analysis, the stresses and displacements in the medium are given by the following equations:

$$(a) \text{ the radial stress } \sigma_r = P \left\{ B_1 [1 - a(R/r)^2] - B_2 [1 + 3a' (R/r)^4 - 4a'' (R/r)^2] \cos 2\theta \right\},$$

$$(b) \text{ the tangential stress } \sigma_\theta = P \left\{ B_1 [1 - a(R/r)^2] + B_2 [1 + 3a' (R/r)^4] \cos 2\theta \right\},$$

$$(c) \text{ the shear stress } \tau_{r\theta} = P \left\{ B_2 [1 - 3a' (R/r)^4 + 2a'' (R/r)^2] \sin 2\theta \right\},$$

$$(d) \text{ the radial displacement } U \\ = \frac{Pr}{2M} \left\{ [1 + a(B_1/B_2)(R/r)^2] - [1 - a'(R/r)^4 + a''(2/B_1)(R/r)^2] \cos 2\theta \right\},$$

$$(e) \text{ and the tangential displacement } V \\ = \frac{Pr}{2M} \left\{ [1 + a'(R/r)^4 + a''(2B_1/B_2)(R/r)^2] \sin 2\theta \right\}.$$

The stresses and displacements in the shell may be obtained by setting  $r = R$  in the equations as follows:

$$(a) \text{ the radial stress } Pr = P \left\{ B_1 [1 - a] - B_2 [1 + 3a' - 4a''] \cos 2\theta \right\},$$

$$(b) \text{ the radial displacement } W = \frac{PR}{2M} \left\{ [1 + a(B_1/B_2)] - [1 - a' + 2a''/B_1] \cos 2\theta \right\},$$

$$(c) \text{ the tangential displacement } V = \frac{PR}{6M} \left\{ [F + C(B_2/2B_1)] [1 + 3a' - 4a''] \sin 2\theta \right\}.$$

Figure 96 represents graphically the afore mentioned equations.



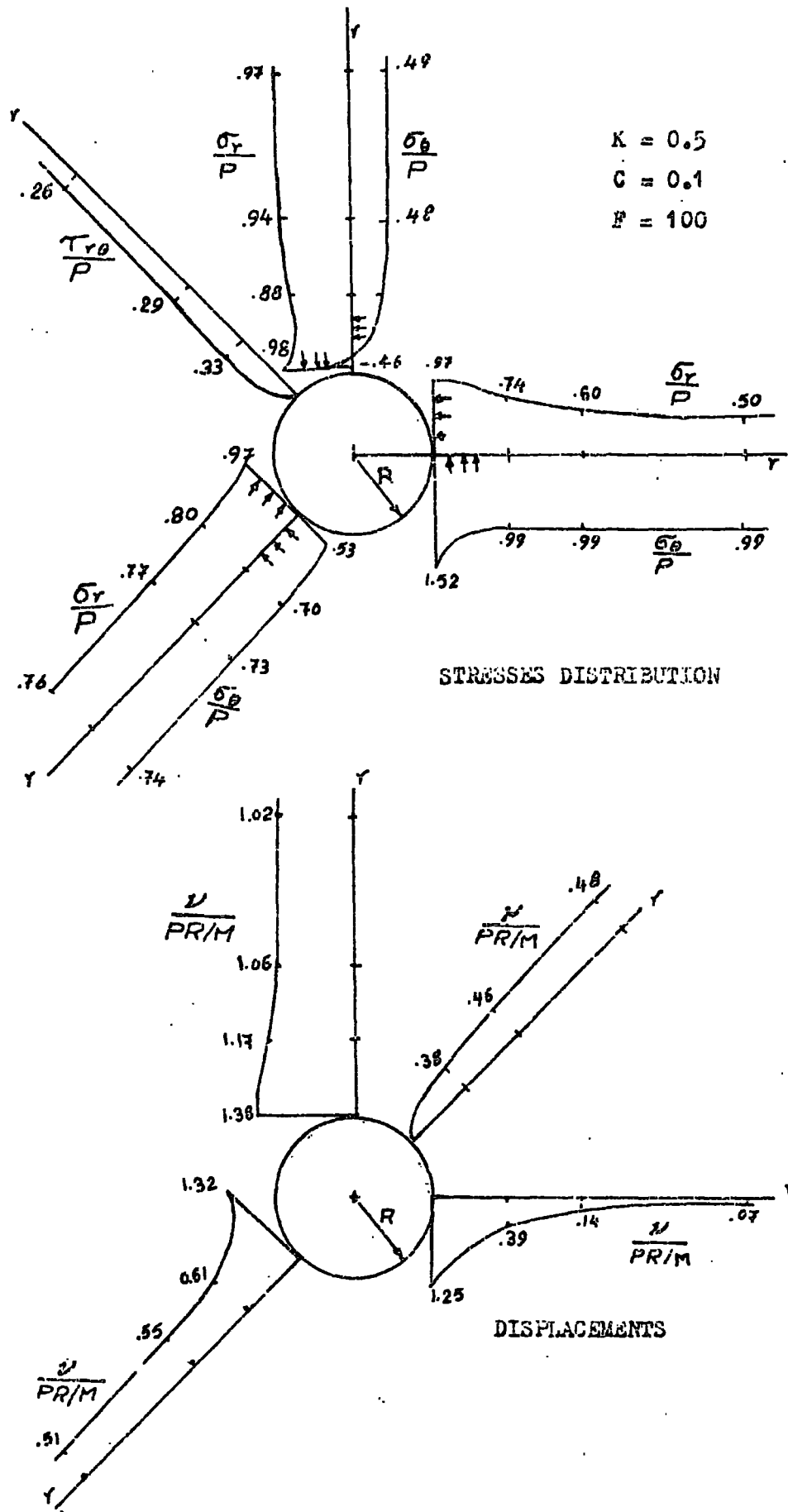


Figure 96 Stresses distribution and displacements in the medium and in the shell .

#### 5.4.2 The method suggested by Peck (1972):

According to this method, the stiffness of the lining relative to that of the soil medium may be quantitatively evaluated by two parameters: the compressibility ratio and the flexibility ratio. The compressibility ratio is a measure of the extensional stiffness of the medium relative to that of the lining, where the extensional stiffness is the measure of the equal uniform pressure necessary to cause unit diametral strain of the lining without any change in shape (see Figure 97). On the other hand, the flexibility ratio is a measure of the flexural stiffness of the medium relative to that of the lining, where the flexural stiffness is a measure of the magnitude of the non-uniform pressure (see Figure 98) necessary to cause unit diametral strain which results in a change in shape, or an ovaling of the lining. The compressibility ratio  $C$  and the flexibility ratio  $F$  are given by the following expressions:

$$C = \frac{E'/(1 + \nu')(1 - 2\nu')}{Et/(R(1 - \nu'^2))}$$

and

$$F = \frac{E'/(1 + \nu')}{6EI/(R^3(1 - \nu'^2))}$$

where  $E'$  and  $\nu'$  are the Young's modulus and Poisson's ratio of the soil medium respectively, and  $E, \nu, R, t$  and  $I$  are the Young's modulus, Poisson's ratio, radius, thickness and moment of inertia of the tunnel lining respectively. The equations derived by Burns and Richard (1964) - mentioned earlier in Section 5.2 - can be easily modified to give the thrust, bending moment, and displacement at any section in the lining for any values of coefficient of earth pressure  $K_0$ . The following equations

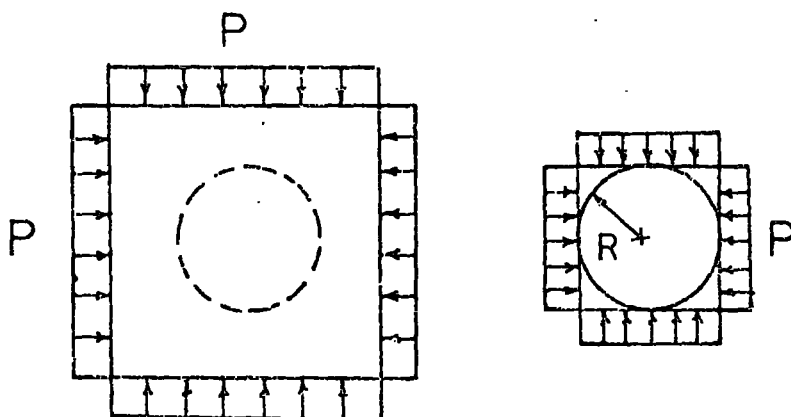


Figure 97 Medium and lining under a state of uniform compression .

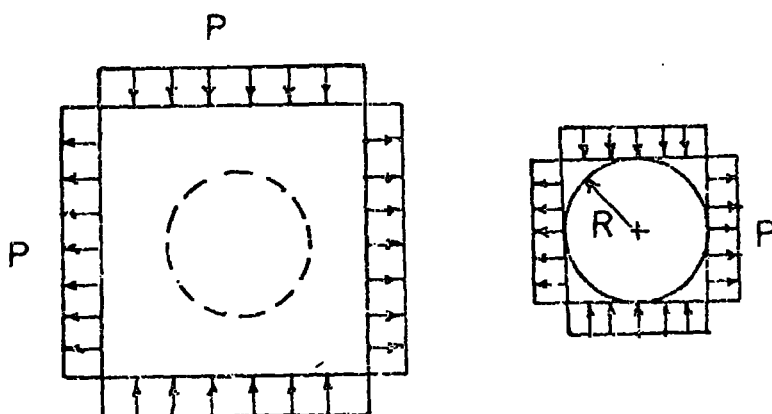


Figure 98 Medium and lining under a state of pure shear .

give the values of the thrust, bending moment, and displacement at the crown and at the springline of a deeply-buried tunnel lining:

a) For the crown or invert:

$$T_c = \frac{1}{2} \left\{ (1 + K_o) b_1 - \frac{1}{3} (1 - K_o) b_2 \right\} \gamma H R ,$$

$$M_c = \frac{1}{6} (1 - K_o) b_2 \gamma H R^2 ,$$

$$W_c = \frac{1}{2} \frac{\gamma H R}{M} \left\{ (1 - \nu') (1 + K_o) b_1 C + \frac{2}{3} \frac{1 - \nu'}{1 - 2\nu'} (1 - K_o) b_2 F \right\} .$$

b) For the springline:

$$T_s = \frac{1}{2} \left\{ (1 + K_o) b_1 + \frac{1}{3} (1 - K_o) b_2 \right\} \gamma H R ,$$

$$M_s = -\frac{1}{6} (1 - K_o) b_2 \gamma H R^2 ,$$

$$W_s = \frac{1}{2} \frac{\gamma H R}{M} \left\{ (1 - \nu') (1 + K_o) b_1 C - \frac{2}{3} \frac{1 - \nu'}{1 - 2\nu'} (1 - K_o) b_2 F \right\} .$$

where

$$b_1 = 1 - a_1 ,$$

$$b_2 = 1 + 3a_2 - 4a_3 ,$$

and

$$a_1 = \frac{(1 - 2\nu')(C - 1)}{(1 - 2\nu')C + 1} ,$$

$$a_2 = \frac{2F + 1 - 2\nu'}{2F + 5 - 6\nu'} ,$$

$$a_3 = \frac{2F - 1}{2F + 5 - 6\nu'} .$$

In these equations,

$\gamma$  = unit weight of soil,

$H$  = height to centre of tunnel,

and  $R$  = the mean radius of the tunnel.

These equations are graphically expressed in Figures 99, 100 and 101 for two values of  $K_0$  (0.5 and 2.0). According to the above equations, the thrust is influenced by both the compressibility ratio and the flexibility ratio. Figure 99 represents the influence of both the compressibility ratio  $C$  and the flexibility ratio  $F$  on the thrust coefficient ( $T/\gamma H R$ ). This Figure shows that for a given value of  $F$ , the thrust coefficient decreases as  $C$  increases, and for a given value of  $C$ , the thrusts at the crown and the springline become nearly identical as  $F$  increases. On the other hand, the moment is influenced only by the flexibility ratio and not by the compressibility ratio. The relation between the moment coefficient ( $M/\gamma H R^2$ ) and the flexibility ratio is shown in Figure 100. Figure 101 shows the variation of the diametral changes with the flexibility ratio. This Figure indicates that for flexibility ratios greater than 10, the diametral changes reach a constant value, and thus the deformation in the lining is independent of the lining structural properties but is governed by the mechanical characteristics of the soil.

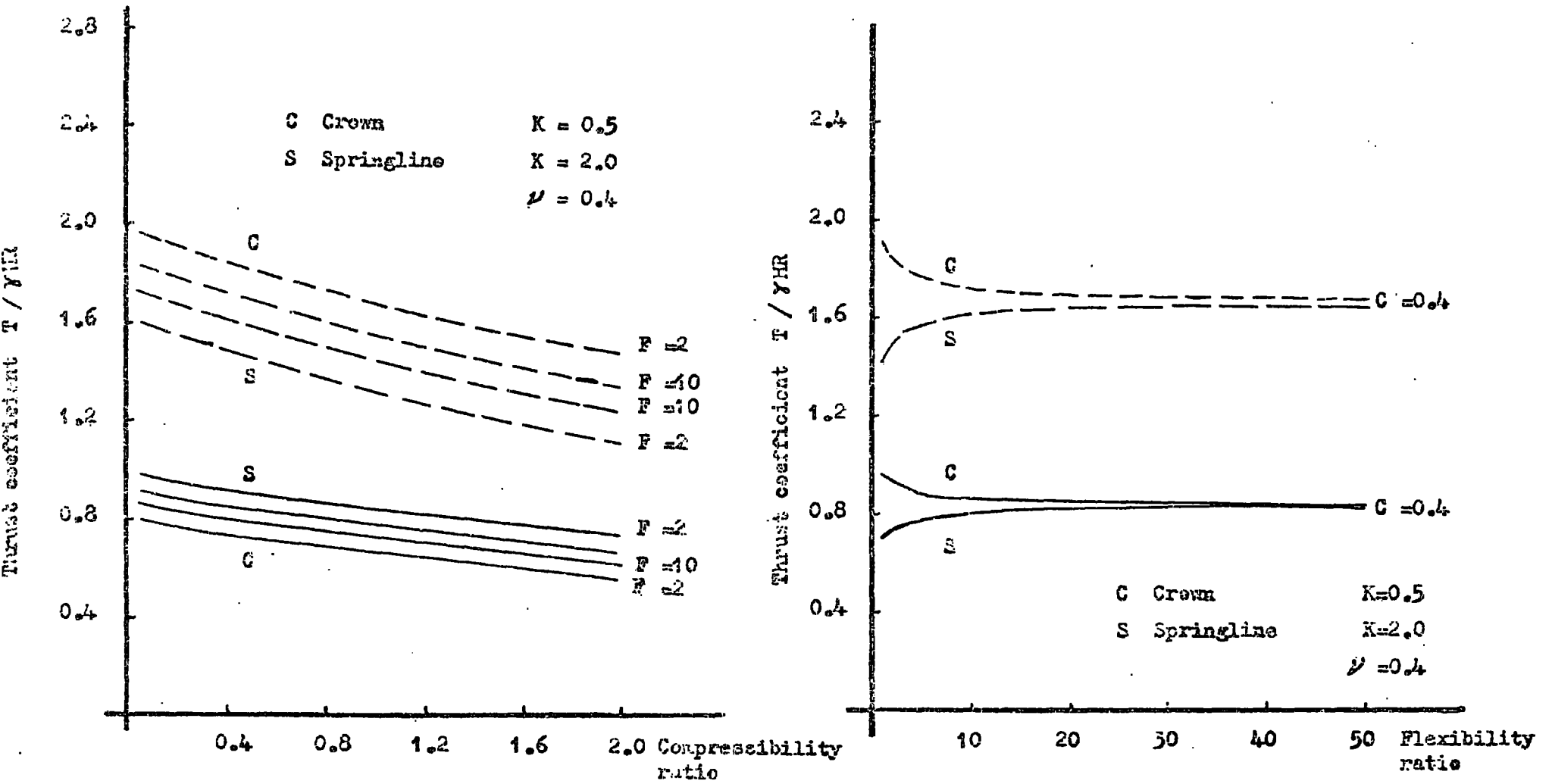


Figure 99 Variation of thrust coefficient with compressibility ratio and flexibility ratio.

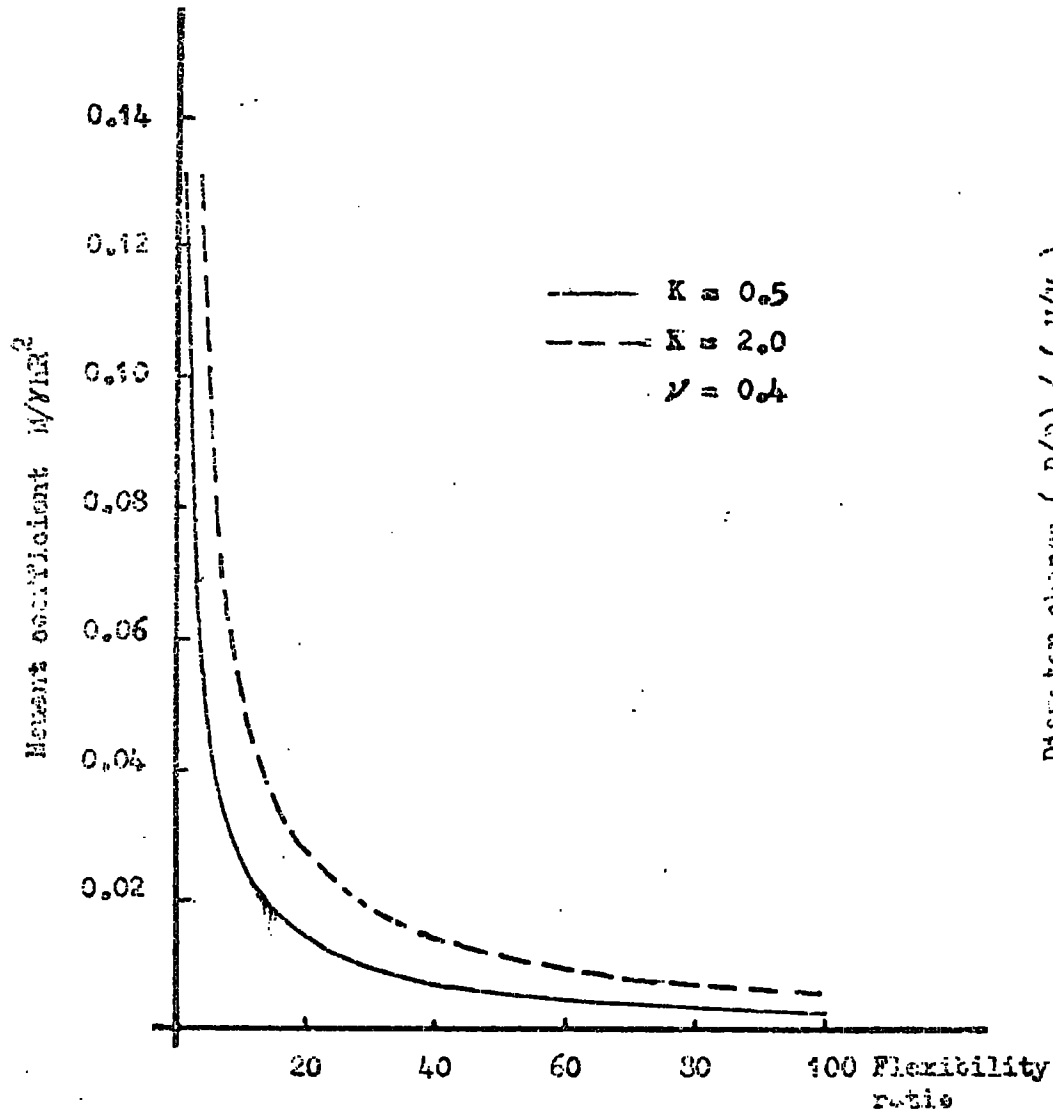


Figure 100 Variation of moment coefficient with flexibility ratio .

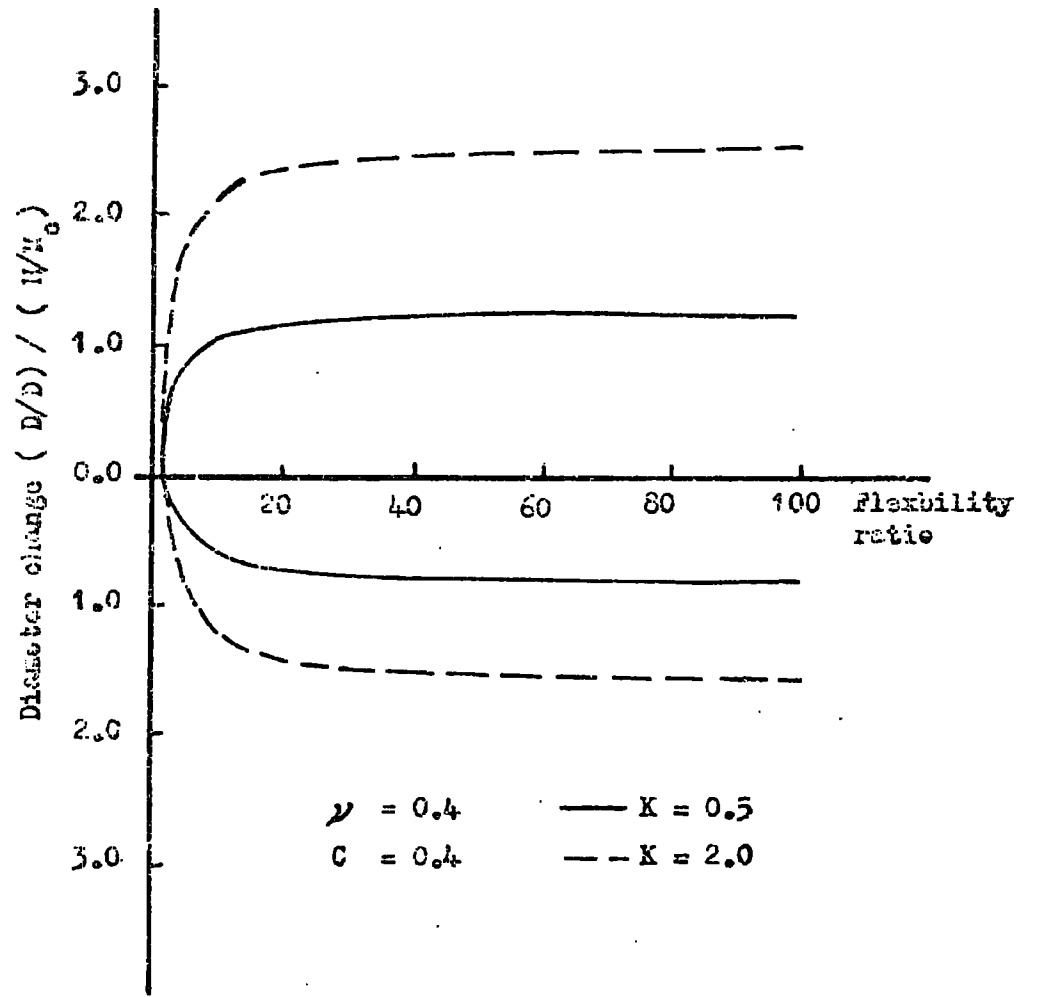


Figure 101 Variation of diameter change with flexibility ratio .

## CHAPTER 6

### SUMMARY AND CONCLUSIONS

#### 6.1 Summary

A programme of work has been instituted with the object of designing, constructing and calibrating a type of earth pressure cell and using it in two field experiments for the measurement of tunnel lining-soil interaction pressure. Six pressure cells were developed for each experiment, the details of the design, construction and calibration of these cells being discussed in detail in Chapter 2 of the thesis.

Two field experiments were carried out for measuring the radial contact pressures around the lining of a tunnel in mixed 'soft' ground (stony clay, laminated clay) on the north bank of the river Tyne in north east England, as shown in Figures 1 and 2. The deformations of the tunnel lining were measured using a dial gauge measuring beam of 0.01 mm sensitivity. Details of the field measurements, installation and data recording are given in Chapter 3.

In Chapter 4, technical analysis of and discussion on the derived data are presented. Resulting from this study, several conclusions may be drawn.

#### 6.2 Conclusions

1. The lining-soil interaction pressure has a nearly uniform final distribution about the tunnel cross-section.
2. The value of the developed pressure at the tunnel crown is nearly one-half the value of the overburden pressure as calculated on the



basis of soil density multiplied by depth from ground surface to the point of measurement interest.

3. The radial contact pressure around the tunnel lining reached a constant level after a period of 7-8 days following lining erection and grouting.
4. The measurement of the deformation of the tunnel lining showed that, under the conditions pertaining, the maximum change in the vertical diameter was 1.30 mm (0.041%), the maximum change in the horizontal diameter was 0.88 mm (0.027%), and the deformation reached a constant value 7 days after lining installation.
5. We may conclude from this evidence that it is possible, under the conditions as specified, to begin the building of the secondary brick lining 6 weeks following the erection of the segmental concrete primary lining since there appears to be no facility for further significant deformation after this period of time. This conclusion is of special interest when, at the present time, the contractor is required to hold-off construction of the secondary lining for a substantial period of time. This may require off-site removal of plant following primary construction, the plant then having to return later for secondary lining construction at greater cost ultimately to the client. The practical advantages of continuous operations are obvious.

APPENDIX A

Theories taking the effect of tunnel depth into consideration

This group will be represented by two theories; Bierbumer's theory and Terzaghi's theory.

1. Bierbumer's theory

According to this theory, the tunnel lining will be acted upon by a pressure "P", equivalent to the weight of the soil mass bounded by a parabola of height  $h = \alpha H$ , as shown in Figure A1. The reduction factor ' $\alpha$ ' could be determined by the following method.

It is assumed that the soil mass, after the excavation of the tunnel, tends to move along sliding planes  $aa_2$  and  $bb_2$  inclined at  $45 + \phi/2^\circ$  with the horizontal. The plane  $ab$  at the crown of the tunnel is acted upon by the weight of the sliding mass  $aa, bb$ , which is counteracted by two forces of friction along the vertical planes  $aa, and bb$ , equal to  $2\mu E$ . Thus the net load at the plane  $ab$  could be given by the following expression:

$$P = \gamma H \left\{ b + 2h_t \tan(45 - \phi/2) \right\} - \gamma H^2 \tan^2(45 - \phi/2) \tan \phi$$

and the pressure  $P$  is given by:

$$P = P/B = \gamma H \left\{ 1 - \frac{\tan \phi \tan^2(45 - \phi/2) H}{b + 2h_t \tan(45 - \phi/2)} \right\}$$

$$= \alpha \gamma H$$

$$\text{where } \alpha = 1 - \frac{\tan \phi \tan^2(45 - \phi/2) H}{b + 2h_t \tan(45 - \phi/2)}$$

The reduction factor  $\alpha$  has two limiting values; for small depths  $\alpha = 1$  and for great depths ( $H > 5B$ ) the effect of depth on the value of  $\alpha$  becomes insignificant and its value is given by  $\alpha = \tan^4(45 - \phi/2)$

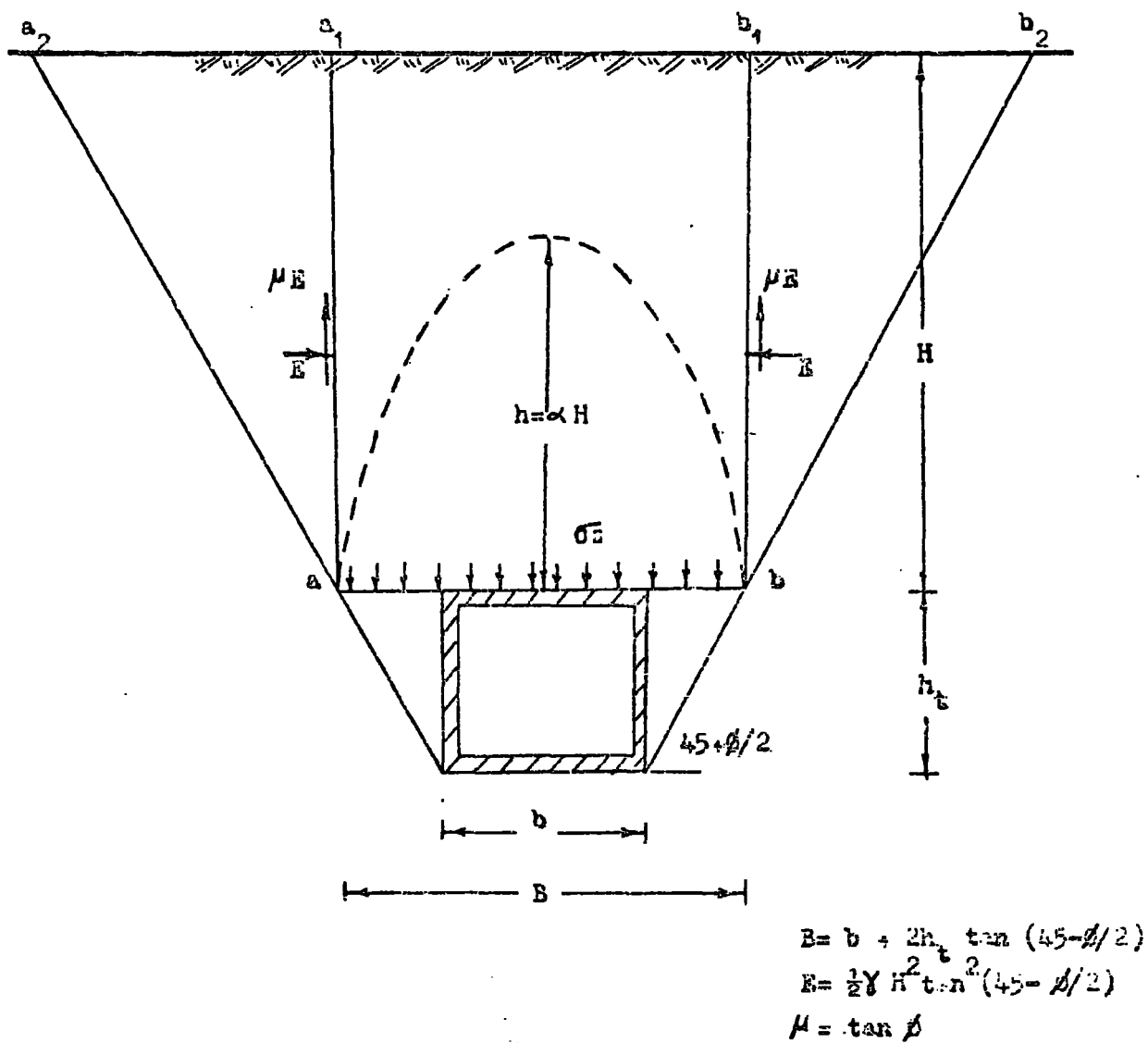


Figure A1

pressure diagram suggested by Bierbaumer

( Szechy, 1956)

## 2. Terzaghi's pressure theory

According to this theory, the pressure " $\sigma_v$ " acting upon the tunnel crown is evaluated according to the following procedure:

Figure A2 represents the pressure diagram suggested by this theory (after Terzaghi 1946). The movement of the soil mass is assumed to take place along two planes of rupture inclined at  $45 + \phi/2$  with the horizontal, starting from the level of the tunnel invert to the level of the tunnel crown, then it continues along the two vertical planes  $aa_1$  and  $bb_1$ .

The stability of a soil prism of width  $B$  and height  $dz$  at a depth  $z$  from the soil surface is considered. The equilibrium of the forces acting on this prism may be expressed as follows:

$$B dz \gamma = B(\sigma_v + d\sigma_v) - B \sigma_v + 2 \tau dz \quad \dots\dots 1$$

$$\text{where } B = b + 2 h_t \tan (45 - \phi/2)$$

$$\gamma = \text{the soil unit weight}$$

$$\tau = \text{shearing force along the planes of failure}$$

$$= c + \sigma_h \tan \phi$$

$$= c + K \sigma_v \tan \phi$$

Substituting in equation 1 we get:-

$$B \gamma dz = B(\sigma_v + d\sigma_v) - B \sigma_v + 2c dz + 2K \sigma_v dz \tan \phi$$

$$\therefore \frac{d \sigma_v}{dz} = \gamma - \frac{2c}{B} - 2K \sigma_v \frac{\tan \phi}{B} \quad \dots\dots 2$$

By solving this differential equation and by considering the boundary condition  $\sigma_v = q$  at  $z = 0$  we get:

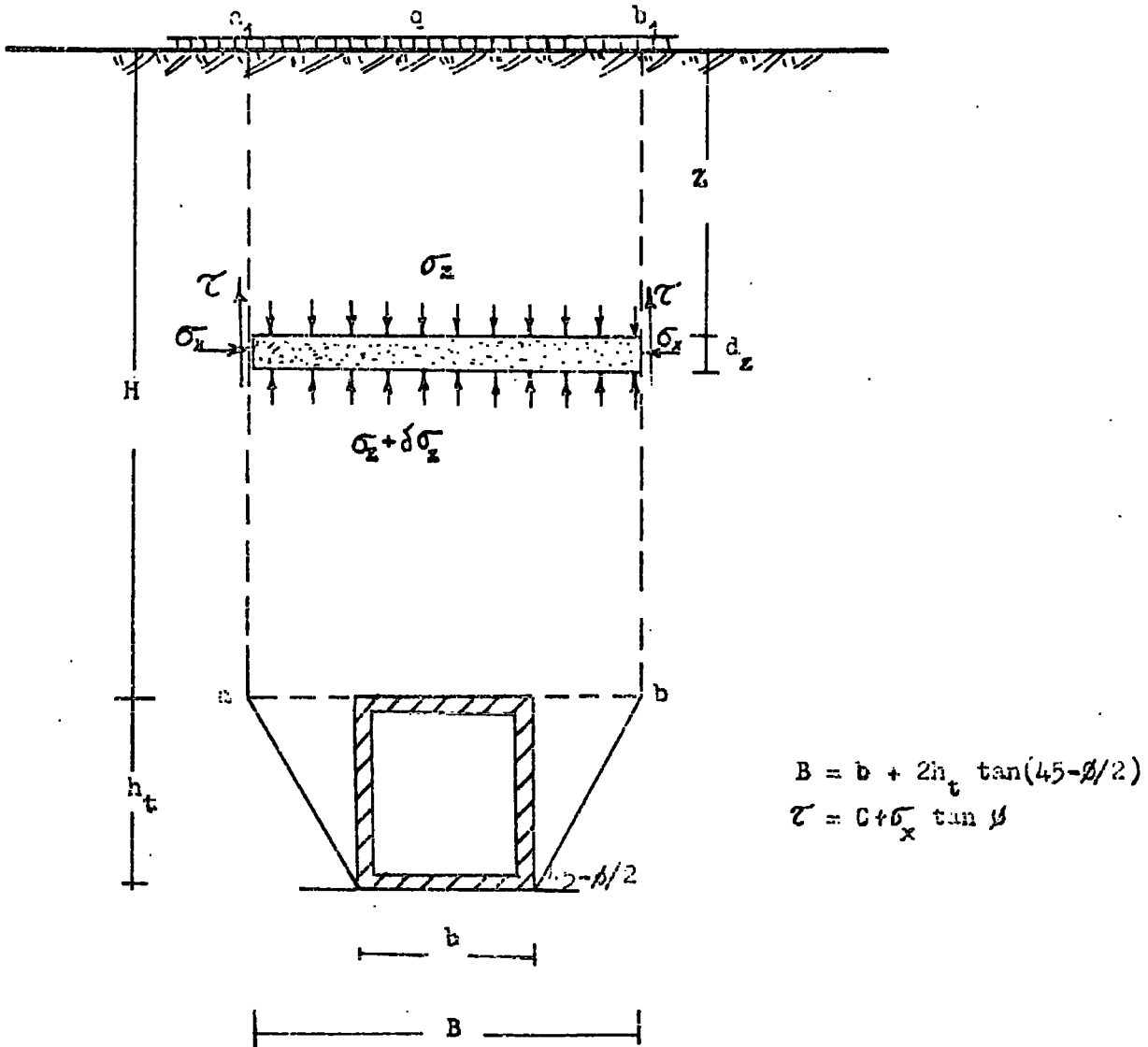


Figure A2 Pressure diagram (after Terzaghi, 1946)

$$\sigma_v = \frac{B \left( \frac{\gamma}{2} - \frac{c}{B} \right)}{K \tan \phi} \left\{ 1 - \exp \left( -K \tan \phi \frac{2z}{B} \right) \right\} + q \exp \left( -K \tan \phi \frac{2z}{B} \right)$$

i.e. for a tunnel at a depth 'H' the soil pressure " $P_v$ " is given by

$$P_v = \frac{B \left( \frac{\gamma}{2} - \frac{c}{B} \right)}{K \tan \phi} \left\{ 1 - \exp \left( -K \tan \phi \frac{2H}{B} \right) \right\} + q \exp \left( -K \tan \phi \frac{2H}{B} \right)$$

APPENDIX B

Theories neglecting the effect of the tunnel depth.

This group is represented by two theories; the Kommerell theory and the Protodyakonov theory.

1. Kommerell theory.

This theory is considered to be one of the approximate methods which gives a quick idea about the soil-structure interaction pressures. According to this theory, the height "h" of the soil mass loaded on the structure is determined from the deformation "e" of the supporting structure, and is given by the following relation:

$$h = 100 e/\delta \quad \dots\dots 1$$

where  $\delta$  is the loosening coefficient of the surrounding soil.

Values of  $\delta$  are given in the Table below:

<u>Description</u>	<u><math>\delta</math> %</u>
Loose granular soil	1-3
Moderately cohesive soil	3-5
Cohesive soil	5-8
Soft rocks	8-12
Solid rock	10-15

The pressure diagram suggested by Kommerell is illustrated in Figure B1. According to this diagram, the structure is loaded by a total load "P" equal to the weight of a soil mass, bounded by a half ellipse of height "h".

The equation of the ellipse is given by:

$$\frac{x^2}{b^2} + \frac{y^2}{h^2} = 1 \quad \dots\dots 2$$





From equations 1 and 2 we get

$$\frac{x^2}{b^2} + \frac{y^2 \delta^2}{(100e)^2} = 1$$

and the total load "P" is given by

$$P = \frac{1}{2} \gamma \pi b h = 50 \gamma \pi b e / \delta \quad \dots\dots 3$$

and the pressure is given by

$$p = 25 \gamma \pi e / \delta \quad \dots\dots 4$$

## 2. Protodyakonov's theory.

This is the most popular theory adopted for the construction of the underground structures in the U.S.S.R. Figure B2 represents the pressure diagram proposed by Protodyakonov. According to this theory the development of a parabolic arch ACB on the structure is assumed. Thus, the stresses along this arch are purely compressive (no bending). Considering the equilibrium of the part CD which is subjected to the forces "T" the horizontal force at C, "PX" the vertical pressure, and "R" the tangential force at D, and by taking moments about D, we get:

$$\frac{1}{2} p x^2 - T y = 0$$

$$\therefore \frac{1}{2} p x^2 = T y \quad \dots\dots 1$$

The resultant force "R" acting at the arch support A can be resolved into two components V and H, as shown in Figure B2. The relationship between the vertical component V and the horizontal component H, taking the effect of the shear stress  $\tau$  into consideration, is given by

$$H = fV - \tau h$$

where f, the coefficient of internal friction =  $\tan \phi$ , and V, the vertical component at A-B level = p b.

$$\therefore H = f p b - \tau h \quad \dots\dots 2$$

From equations 1 and 2 we get

$$\frac{1}{2} p b^2 = \{ f p b - \tau h \} h$$

$$\tau = p b \left\{ \frac{2fh - b}{2h^2} \right\} \dots\dots 3$$

The height 'h' of the developed arch is obtained by differentiating equation 3. This will cover the condition that h is developed with the maximum value of "τ", whence

$$d\tau/dh = pb \left\{ \frac{b - fh}{h^3} \right\} = 0$$

$$\text{Therefore } h = b/f \dots\dots 4$$

From equations 3 and 4 we get

$$\tau = \frac{1}{2} pf^2 \dots\dots 5$$

and by substituting in equation 2 we have

$$T = fpb - \frac{1}{2} pbf = \frac{1}{2} pbf \dots\dots 6$$

Substituting in the equation 1 we derive the equation of the parabola as

$$y = x^2/bf$$

The total load/unit length of the structure "P" equals the weight of the soil mass bounded by the parabola:

$$\begin{aligned} P &= \frac{4}{3} b h \gamma \\ &= 4 \gamma b^2 / 3f \end{aligned}$$

whence the pressure at A-B level is given by

$$P_v = 2 \gamma b/3f$$

where  $\gamma$  = unit weight of the soil

$$f = \tan \phi$$

N.B.

This theory has been developed for granular non-cohesive soil (sand), but it could be applied to cohesive soils and rocks by using the values

of the empirical coefficient "f" proposed by Protodyakonov as a result of experiments and practical experience. The values of the coefficient "f" (known as the strength coefficient) are tabulated in Table 14.

Strength grade	Denotation of rock (soil)	Unit-weight (kg/m <sup>3</sup> )	Crushing strength $\sigma_c$ (kg/cm <sup>2</sup> )	Strength coeff. 'f'
Highest	Solid, dense quartzite, basalt and other solid rocks of exceptionally high strength	2800 3000	2000	20
Very high	Solid, granite, quartzporphyr, silica shale. Highly resistive sandstones and limestones	2600-2700	1500	15
High	Granite and alike. Very resistive sand- and limestones. Quartz. Solid conglomerates.	2500-2600	1000	10
High	Limestone, weathered granite. Solid sandstone, marble. Pyrites.	2500	800	8
Moderately strong	Normal sandstone	2400	600	6
Moderately strong	Sandstone shales	2300	500	5
Medium	Clay-shales. Sand- and limestones of smaller resistance. Loose conglomerates	2400-2800	400	4
Medium	Various shales and slates. Dense marls.	2400-2600	300	3
Moderately loose	Loose shale and very loose limestone, gypsum, frozen ground. Common marl. Blocky sandstone, cemented gravel and boulders, stoney ground	2200-2600	200-150	2
Moderately loose	Gravelly ground. Blocky and fissured shale, compressed boulders and gravel, hard clay.	2200-2400	—	1.5
Loose	Dense clay. Cohesive ballast. Clayey ground.	2000-2200	—	1.0
Loose	Loose loam, loess, gravel.	1800-2000	—	0.8
Soils	Soil with vegetation, peat, soft loam, wet sand.	1600-1800	—	0.6
Granular soils	Sand, fine gravel, upfill	1400-1600	—	0.5
Plastic soils	Silty ground, modified loess and other soils in liquid condition	—	—	0.3

Table 14. Strength coefficient 'f' (after Protodyakonov).

REFERENCES

- BJERRUM, L., KENNY, T.C. and KJAERNSLI, B. (1965) "Measuring instruments for strutted excavation", Proc. ASCE, Vol. 91, pp. 94-111.
- BROWN, S.F. and PELL, P.S. (1967) "Subgrade stress and deformation under dynamic load", Proc. ASCE, Vol. 93, pp. 17-45.
- BURNS, J.Q. and RICHARD, R.M. (1964) "Attenuation of stresses for buried cylinders", Proc. Symp. on Soil-Structure interaction, Tucson, 1964 pp. 78-392.
- HANNA, T.H. (1973) "Foundation instrumentation", First edition, Trans. Tech. Publications, Switzerland.
- KALLSTENIUS, T. and BERGAU, W., (1956) "Investigations of soil pressure measuring by means of cells", Proc. Royal Swedish Geotechnical Institute, Vol. 12.
- PEATIE, K.R. and SPARROW, R.W. (1954) "The fundamental action of earth pressure cells", Journal of the Mechanics and Physics of Solids, Vol. 2, pp. 144-155.
- PECK, R.B. (1969) "Deep excavations and tunnelling in soft ground", Proc. 7th Int. Conf. on Soil Mech. and Found. Engrg., State of the Art Volume, Mexico City, pp. 225-290.
- PECK, R.B., HENDRON, A.J., Jr., and MOHRAZ, B. (1972). "State of the art of soft ground tunnelling", North American Rapid Excavation and Tunnelling Conference, pp. 259-286.
- SHEPHERD, R. (1967) "Some measurements of foundation bearing pressure", Journal of Strain, Vol. 3, pp. 32-35.
- SKEMPTON, A.W. (1943) Discussion on "Tunnel Linings with special reference to a new form of reinforced concrete lining," by G.L. Groves, Journal ICE, March, pp. 29-64.

- SPARROW, R.W. and TORY, A.C. (1966) "Behaviour of soil mass under dynamic loading", Proc. ASCE, Vol. 92, pp. 59-86.
- TAYLOR, D.W. (1947) "Pressure distribution in soils", Soil Mechanics Fact Finding Survey, Waterways Experimental Station, U.S.A.
- TERZAGHI, K. (1942) "Shield tunnels of the Chicago Subway", Journal of Boston Soc. of Civil Eng., Vol. 3, pp. 163-209.
- THOMAS, H.S.H. and WARD, W.H. (1969) "The design construction and performance of a vibrating wire earth pressure cell", Geotechnique, vol. 19, No. 1, March, 1969, pp. 39-51.
- TIMOSHENKO, S. and WOINOWSKY, K.S. (1959) Theory of Plates and Shells. Mc Graw-Hill, New York.
- WARD, W.H. and THOMAS, H.S.H., (1965) "The development of earth loading and deformation in tunnel linings in London Clay". Proc. 6th Int. Conf. on Soil Mech. and Found. Engrg, Montreal, pp. 432-436.
- WATERWAYS EXPERIMENTAL STATION, (1944) "Pressure cell investigation", U.S. Army Engineer Waterways Experimental Station, Vicksburg, Memorandum no. 210-1.
- WONG, H.Y. (1974) "Some design and performance considerations of diaphragm type pressure cells using strain gauges", Proc. Inst. of Civ. Eng., Vol. 2, pp. 93-99.

